An Environmentally Sensitive Equilibrium Morphology Phase Map of Zinc Sulphide Nanoparticles

Christopher A. Feigl, B.Sc(Hons)

School of Applied Science

College of Science, Engineering and Health

RMIT University

August, 2012

A THESIS SUBMITTED TO RMIT UNIVERSITY FOR THE DEGREE OF DOCTOR OF PHILOSOPHY IN THE FACULTY OF APPLIED PHYSICS

Declaration

The work reported in this thesis is the candidate's alone, except where acknowledged. No part of this thesis has been submitted previously, in whole or in part, to qualify for any other academic award. The content of the thesis is the result of work which has been carried out since 12th January 2009. All ethics procedures and guidelines have been followed.

Christopher A. Feigl

Dedication

This work is dedicated to the memory of Professor Ian K. Snook – esteemed patriarch of physics at RMIT University, inspiring leader and tireless mentor.

Acknowledgements

It is with immense gratitude that I acknowledge the academic and professional guidance of my PhD supervisors Professor Salvy P. Russo and Dr. Amanda S. Barnard. For their countless hours of instruction on theoretical and technical topics, their wisdom and the post-doctoral opportunities they have helped to create, I am forever grateful. I also wish to formally acknowledge the support of the Australian Research Council by way of the Australian Postgraduate Award, as well as the CSIRO PhD Scholarship Program.

For their support and kinship I would like to thank my parents and their partners, my aunt, my brother, my sister-in-law, my nephew. Furthermore, I would like to acknowledge the support given to me by my close friends, my partner and my fellow post-graduate students at RMIT University. Thank you for the excellent homes I have been a part of, as well as the couches and spare rooms provided when flood waters rose, rental leases expired and scholarships ended, and for sharing the little victories and the anguishes along the way.

This project was made possible by extensive amounts of computation time and resources supplied entirely by the National Computational Infrastructure.

CONTENTS

List of Figures

List of Tables

Publications

Feigl, C.A., A.S. Barnard, and S.P. Russo *Modelling polar wurtzite ZnS nanoparticles: the effect of sulphur supersaturation on size- and shape-dependent phase transformations*. Journal of Materials Chemistry, 2012. **22**(36): p. 18992-18998.

Feigl, C.A., A.S. Barnard, and S.P. Russo, *Modelling nanoscale cubic ZnS morphology and thermodynamic stability under sulphur-rich conditions*. CrystEngComm, 2012. DOI:10.1039/C2CE25814E. *In Press.*

Feigl, C.A., A.S. Barnard, and S.P. Russo, *Size- and shape-dependent phase transformations in wurtzite ZnS nanostructures.* Physical Chemistry Chemical Physics, 2012. **14**(28): p. 9871-9879.

Feigl, C.A., S.P. Russo, and A.S. Barnard, *A comparative density functional theory investigation of the mechanical and energetic properties of ZnS.* Molecular Simulation, 2011. **37**(4): p. 321-333.

Barnard, A.S., C.A. Feigl, and S.P. Russo, *Morphological and phase stability of zinc blende, amorphous and mixed core-shell ZnS nanoparticles.* Nanoscale, 2010. **2**(10): p. 2294-2301.

Feigl, C.A., S.P. Russo, and A.S. Barnard, *Safe, stable and effective nanotechnology: phase mapping of ZnS nanoparticles.* Journal of Materials Chemistry, 2010. **20**(24): p. 4971-4980.

Abstract

Zinc sulphide (ZnS) nanoparticles have promising applications in a diverse range of fields, including bio-technology; optoelectronics; catalysis; photovoltaics; gas, chemical and bio-sensors; field effect transistors; and field emitters. Like most modern nanomaterials, ZnS nanoparticles derive their utility from physical properties which can be 'customised' or 'tuned' for specific needs; however, there are considerable risks associated with the use of nanoscale ZnS, which exist as a direct consequence of the structure/property relationships from which their utility is derived. These risks include instability, adverse physical properties and elevated toxicity. In order to minimize exposure to these risks, *ab inito* calculations and a shape-dependent thermodynamic model were used to predict the equilibrium morphologies and phase transformations between the cubic, hexagonal and amorphous phases of ZnS as a function of size, temperature and pressure. The likelihood of a phase transformation occurring was fond to vary significantly, depending heavily on both size *and* shape. Further to this, thermodynamic conditions were identified which are expected to favour the formation of specific morphologies and encourage long-term stability in a broader environmental sense. These results show how tailoring the shape of a nanoparticle may ultimately determine its phase by encouraging or suppressing phase transformations, and provide insight into how experimental synthesis conditions can be modified to obtain synthesis objectives and maintain post-synthesis phase and morphological stability; outcomes which are critical for safe, stable and effective applications of this material.

Chapter 1. Introduction

1.1 Nanotechnology Emerging

Following its conceptual origins in the mid-twentieth century[1], 'nanotechnology' has grown to become a vital component of modern day science and technology. This emerging field is rapidly adopting some of the most highly anticipated and promising scientific advances of recent times. As a result, the market share of nanotechnology-enhanced consumer products (such as clothing, cosmetics, sporting goods and building materials) is steadily increasing[2,3], while government organisations also are placing more funding into nanotechnology research for public interests such as renewable energy[4,5], water purification[6] and defence[7,8].

The potential impacts relating to progress in this field display considerable depth and breadth. For example, on the molecular scale, nanoparticles are used to selectively target bio-molecules, such as DNA sequences and protein receptors[9-11]. On the other end of the applied size scale, nanomaterial-based catalysts acting on environmentally sensitive compounds such as CO_2 could potentially be applied to such problems as global warming and climate change[12,13]. These examples illustrate how even though the length scale of nanoscale components is very small, the length scales spanned by potential applications is surprisingly broad. As a result of this breadth and depth is has been speculated that the socio-economic impacts of advanced nanotechnology could be greater than the industrial and information technology revolutions[14]. However, such promises come attached to significant causes for concern, as progress in the field is persistently shadowed by fundamental and significant risks[15], with many formidable challenges requiring urgent attention.

Currently, despite enormous amounts of experimental development and rapidly evolving technology markets, nanotechnology remains one of the least understood and most difficult fields of progress to regulate[15]. It is widely recognised that there are gaps between

our technical capabilities and theoretical knowledge, and between applications and regulatory frameworks. Regarded by many as a ticking time bomb with the potential to bring about a broad consumer backlash (like that seen against genetically modified crops), considerable effort is made to stay abreast of public attitudes towards nanotechnology and to ensure that exposure to risk is minimised[16]. This naturally requires a suitable level of assurance that nanomaterials are safe, stable and effective before they are applied to ourselves or our environment. Without the adequate regulatory framework however, such assurances are easily ignored. Furthermore, such assurance requires modern, advanced methods in material science, as the structural and physicochemical complexity of nanomaterials are significantly increased over their bulk counterparts.

Part of this increase in complexity is the result of structure-property relationships, which manifest themselves on the nanoscale. These relationships allow a wide array of chemical and physical properties to be 'customised' or 'tuned' for specific needs, by carefully controlling the size or structure of the material. The hazards associated with nanomaterials exist as a direct consequence of the structure-property relationships from which their utility is derived. These hazards include elevated toxicity and reduced efficiency. For example, nanomaterial devices based on a specific set of properties may cease to function, or function with significantly reduced efficiency, should the material alter its structure. Secondly, the biological and environmental significance of a material is significantly increased once the size is reduced to the nanoscale (as a result of the massive increase in surface area), and may also be drastically altered as a result of structural changes. A poignant example is a potentially toxic substance emerging at the nanoscale, even when the same material is perfectly harmless and benign in bulk form, or in a different nanoscale phase. For example, the surfaces of ZnO are photochemically active, and produce reactive oxygen species (also known as free radicals) upon exposure to certain frequencies of UV light. This is of little consequence when the

effective surface area is very low (as it is in bulk materials), but when the surface-to-volume ratio becomes very large the production efficiency of free radicals increases by orders of magnitude[17]. This is significant since free radicals have been shown to damage DNA[18]. In a broader sense, the consequences of these risks could pose a threat to our environment, to ourselves and to other living organisms[19-24]. Subsequently, one of the most highly coveted yet complex aims of modern nanotechnology is establishing qualitative and quantitative measures of nanomaterial structure-property relationships and establishing robust methods of morphology and phase prediction and control.

1.2 Nanomorphology and Phase Selection on the Nanoscale

The first step in accomplishing these aims involves constructing a detailed understanding of how nanomaterials interact with their surroundings, and with each other. Even inorganic nanomaterials can respond to changes in their surroundings, in order to find some equilibrium. This can be difficult to anticipate, since the thermodynamic behaviour of nanomaterials (the response of the material to temperature and pressure) differs from bulk-scale materials. This is primarily due to contributions from the free energy associated with geometric features containing under-coordinated atoms[25]. In many cases the most significant feature is the effective surface energy, which is the product of the total surface free energy and the total surface area. This contribution is insignificant at the macro scale, as the surface atoms comprise a very small fraction of the whole entity. However as the size is reduced the surface-to-volume ratio becomes large and the surface free energy term becomes more significant. At the nanoscale the surface free energy term can dominate, leading to equilibrium arrangements of atoms that differ greatly from the bulk. Understanding the complex free energy profiles of nanomaterials, with respect to structure and environment, and identification of low energy configurations are key elements to successful nanomorphology prediction and control.

In order to adopt a lower energy configuration, all materials must surpass a free energy transformation barrier. Kinetic processes (the physical motion of atoms) determine how this transpires, and the height of the barrier determines whether or not this barrier can be overcome. Hence, the final atomic arrangement of a given material is determined through a combination of thermodynamic and kinetic processes, whereby thermodynamics determine the energetically preferred structure of a material and kinetics determine how (and if) that structure is reached. Once the final structure has been determined (irrespective of whether it is the thermodynamically equilibrium structure, or merely a meta-stable kinetic structure), maintaining the structural integrity of nanomaterials in their local environment is also vitally important, since the properties of a given nanomaterial, including its physical and chemical behaviour, are utterly dependent upon its size and structure and response to local environmental changes[26].

As we enter a period when new nanomaterial products are continuously entering the marketplace and nano-medicines are entering clinical trial stages, assessing the safety and stability of nanomaterials has risen to the top of our priority list, irrespective of how benign their macroscopic form may be. The consequences of releasing a poorly tested nanomaterial are far reaching[19-24], but the task of assessing the stability and toxicity of nanomaterials represents an enormous challenge owing to the complex thermodynamic and kinetic influences as mentioned above. New approaches to material safety assessments are required, and it is becoming increasingly apparent that theory, computational science and predictive modelling (primarily for rapid, simultaneous assessment a large number of physical parameters) are a critical means to this end[27,28].

1.3 The Case for Zinc Sulphide

Among the nanomaterials produced today, zinc sulphide (ZnS) nanoparticles (NPs) are an excellent candidate for a array of novel applications in a diverse range of fields, such as: bio-technology[9,29-31]; optoelectronics[29,32-34]; catalysis[29,35,36]; photovoltaics[37]; gas[29,38], chemical[29,31,39] and bio-sensors[29,31]; field effect transistors[29,31] and field emitters[40,41]. ZnS is a type II-VI semiconductor with two stable crystalline phases in bulk (macroscopic) form at standard temperature and pressure (STP): the low energy cubic (zinc blende, or ZB) phase and the metastable hexagonal (wurtzite, or WZ) phase[29]. Both are common crystalline phases of ZnS nanoparticles and exhibit well-documented structure-property relationships on the nanoscale[29]. Devices typically incorporate NPs of one phase or the other and long term functionality relies on the stability of the nanoparticle morphology or the predictable switching between different structures on demand, irrespective of their surrounding chemical conditions. However it has been conclusively shown that ZnS NPs readily undergo reversible and irreversible phase transformations between the ZB and WZ phases under ambient conditions[42-44]. This throws into question the long term reliability of devices based on the phase dependent properties of this material, and may expose hazards relating to eco-/cyto-toxicity. For these reasons phase transformations and the structures of ZnS nanoparticles have received considerable attention[45-69]. However, accurate phase prediction of ZnS nanoparticles still has not been achieved and the relationship between the phase determining factors remains poorly understood.

Using advanced theoretical and computational methods it is possible to rapidly explore the complicated phase space that makes up the thermodynamic domain of ZnS nanoparticle phase and nanomorphology, and map the equilibrium morphologies as a function of the dominant thermodynamic influences[70]. These methods are proving to be powerful, even irreplaceable tools in the quest for nanomorphology prediction and control[27,28] and are

applied to the study of ZnS in the work contained herein. This study will serve to increase the reliability and safety of current and prospective devices and products utilising this novel and highly functional nanomaterial.

1.4 Outline of Thesis

This thesis is structured in the following manner. Chapter 2 discusses existing experimental and theoretical knowledge on the subject on ZnS, with a focus on nanoscale properties and phenomena, solid phases and nanoscale phase transformations, as well as highlighting the need for and providing an overview of the current body of work. Chapter 3 offers a description of the theoretical framework and computational methods employed in the current study. Chapter 4 sets out various computational (density functional theory - DFT) methods and applies them to the calculation known bulk properties of ZnS, for the purpose of comparison with experiment and to ascertain the most effective DFT method for the study of ZnS. Chapters 5-9 apply these computational and theoretical techniques to model ZnS nanoparticles and determine the equilibrium phase and shape. In Chapters 5 and 6 this is performed for the zinc blende and wurtzite phases, respectively, as a function of size. Chapter 5 includes a comparison with the amorphous phase, while Chapter 6 compares low energy zinc blende and wurtzite morphologies in order to determine the sizes at which phase transformations are likely to occur between the two. Chapters 7 and 8 apply *ab initio* thermodynamics techniques to the zinc blende and wurtzite phases, respectively, so that temperature and pressure dependence on phase selection can be modelled. Chapter 9 includes a study of some non-equilibrium, mixed phase morphologies that are of particular interest experimentally. Finally Chapter 10 summarises the findings of this work as a whole. The Appendices include derivations of the geometric expressions required for the shape-dependent thermodynamic methods employed in this study, as described in Chapter 3.

Chapter 2. Background

2.1 Introduction to ZnS Nanoparticles

A review of work pertaining to the formation and stability of zinc sulphide (ZnS) nanoparticles is presented in this chapter, and the role of mapping the equilibrium morphologies as a means of predicting the most probable phase of this material (and hence its stability and biological and environmental significance) is highlighted. As will be described, ZnS is a highly suitable example, as the material is technologically relevant, but exhibits acute structural sensitivity to changes in the thermal and chemical environment; even under ambient conditions.

From a technological perspective, ZnS is a II-VI class semiconductor, and when the physical dimensions of this material are comparable to the Bohr excitonic radius luminescent nanoparticles or 'quantum dots' may be produced[71]. This class of semiconductor nanomaterials is also occupied by the well-known cadmium sulphide (CdS) and cadmium selenide (CdSe) quantum dots. All are the focus of extensive experimentation in nanoparticle form, and are being considered for applications in a range of fields including medical diagnostics and therapeutics, optoelectronics, catalysis and photovoltaics[9-11,29-41,72-102]. Nanoparticles of ZnS are often doped with impurities such as manganese or copper to improve their luminescent properties, and used to 'cap' or form a shell surrounding a core nanoparticle consisting of a similar II-VI semiconductor, such as CdS or CdSe[103,104].

In both cases, the material exposed to the surrounding environment or biological system is ZnS, which is significant since ZnS nanoparticles have been shown to be inherently unstable and (like a large number of other industrially relevant nanoparticles) have the potential to undergo uncontrolled, post-synthesis, solid-solid phase transformations under ambient conditions[42-44]. A thorough review of existing experimental knowledge and

theoretical work, ascertaining the common structural morphologies and the dominant influences driving phase selection of ZnS nanoparticles, will provide valuable insights into the current state of knowledge and serve to highlight what remains to be addressed to achieve accurate and reliable morphology prediction under operationally and environmentally relevant conditions.

2.2 The Solid Crystalline Phases of ZnS

The base of current knowledge rests on previous work examining the macroscopic forms of ZnS. In bulk form ZnS is used extensively in optoelectronic devices[105]. At standard temperature and pressure (STP) ZnS is stable in the zinc-blende (ZB or B3) phase, otherwise known as sphalerite. The ZB phase possesses a dual basis, face-centred cubic structure with an internal parameter of (¼, ¼, ¼). Both zinc and sulphur atoms are tetrahedrally coordinated and the ZnS dimers are stacked in an ABCABC arrangement. A meta-stable wurtzite (WZ or B4) structure also exists at STP, but is more stable than the ZB phase above 1020˚C (a ZB to WZ solid-solid phase transformation occurs at this temperature). The WZ structure has ABAB stacking in the ZnS dimers which produces a hexagonal close-packed system with tetrahedral bonding. These crystal structures are illustrated in Figure 2.1. At high pressures (above ~15 GPa) the rocksalt (RS or B1) phase exists, and the Cinnabar (CmCm or B2) phase emerges above ~65 GPa[54]. These pressures are too high for the typical operational environments of nanoparticles, and are well beyond the pressures induced by surface stresses even at small sizes.

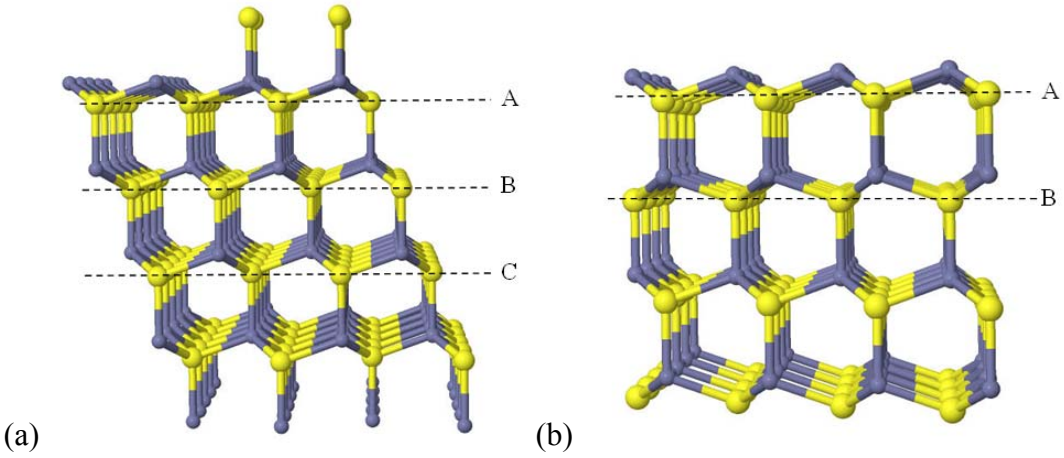

(a) (b)

Figure 2.1 – Common phases of ZnS at STP, showing stacking of the ZnS dimmers in (a) an ABCABC arrangement in the ZB phase, and (b) an ABAB arrangement in the WZ phase.

However, in nanoscale systems reversible and irreversible phase transformations between ZB and WZ phases occur under ambient conditions. Motivated by the need to control nanocrystalline morphology a large amount of experimental and theoretical studies have investigated the nature of these transformations, shedding light on the dominant phase determining factors of size, chemical environment and aggregations state, as well as temperature and pressure[45-69].

Qadri *et al.*[47] observed XRD diffraction peaks from the WZ phase in samples of initially pure ZB phase following annealing at temperatures as low as 400˚C, significantly lower than the bulk transformation temperature of 1020˚C. Qadri *et al.*[48] also carried out pressure induced transformations on 2.8 nm and 25.3 nm nanoparticles, finding that the 25.3 nm sized particles underwent a WZ to ZB phase transformation at 0.5 GPa and a subsequent transformation to the RS phase at 15.0 GPa. The ZB phase was restored when the pressure was released. In contrast, the 2.8 nm particles, initially in the ZB phase, required a pressure of 18.0 GPa for transformation to RS (3.0 GPa higher than the larger 25.3 nm sample), indicating a size-dependent pressure transformation point. The ZB phase was again restored upon the release of pressure.

Pan *et al.*[49] carried out similar tests on 10 nm and 5 nm nanoparticles, finding an increase in the ZB to RS transition pressure from 16.2 GPa to 16.9 GPa with a reduction in nanoparticle size from 10 nm to 5 nm, respectively, and an increase in compressibility.

In a related study, Yang *et al.*[52] investigated the pressure dependence of the temperature transformation points. Their samples consisted of ~3-4 nm ZB nanoparticles (see Figure 2.2). A ZB to WZ phase transformation was detected at 400˚C under ambient pressure, with a clear indication of the WZ structure at 500˚C (again substantially lower than the bulk transition temperature of 1020˚C). Under a pressure of 1 GPa the ZB to WZ transformation occurred at 250˚C, however above 300˚C the average size increased to 10 nm. This pressure-temperature-size inter-dependency is primarily responsible for the significant difficulty in obtaining an experimental phase map.

2.3 ZnS Nanoparticle Synthesis

A large variety of synthesis techniques are available for producing nanoparticles in both ZB[43,106-114] and WZ[43,114-119] phases. These have been summarised in Table 2.1. Techniques commonly employ specific solvents or surfactants to gain morphology control. For example, in the synthesis of WZ structures, Zhao *et al.*[119] noted the importance of using polyols as passivating agents while Sun *et al.*[118] also found it necessary to add ethylene glycol.

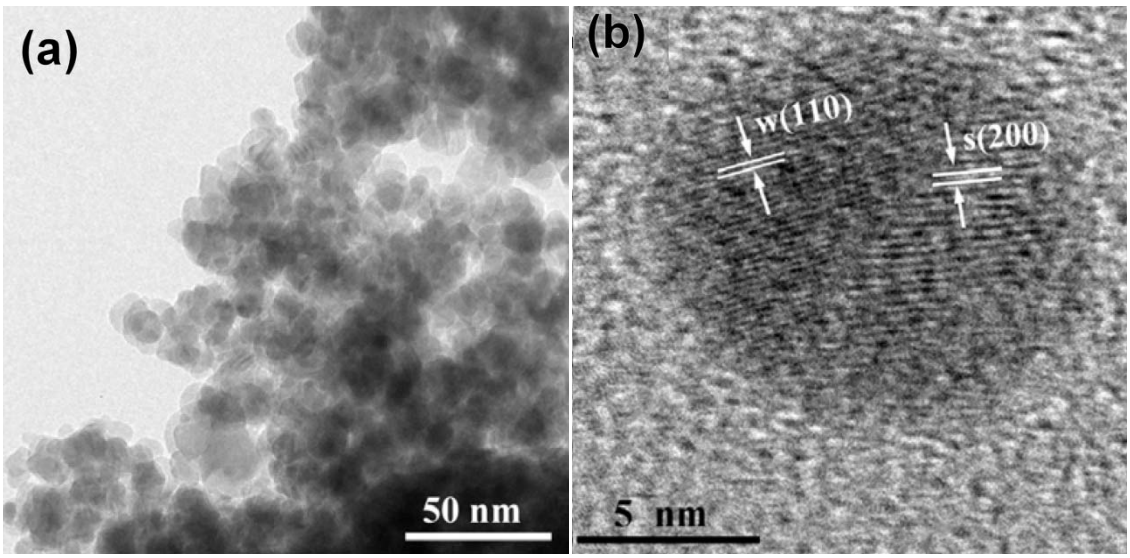

Figure 2.2 - ZnS nanoparticles showing mixed ZB and WZ structures. (a) TEM image after 300˚C (for 1 h) under a pressure of 1 GPa, and (b) HRTEM image of a representative ZnS nanoparticle following the same procedure. The w(110) and s(200) indices refer to the (110) and (200) planes of the WZ and ZB phases, respectively. Reproduced with permission from reference 56, Institute of Physics and IOP Publishing Limited © 2009

Tong *et al.*[114] produced ZB structures in the presence of water, WZ in the presence of ethanolamine and both in the presence of ethanediamine (where temperature became the determining factor). Furthermore, the p*Ka* values of the organic molecules was found to be a critical factor for inducing phase transformations in a study of post-synthesis morphology control methods by Murakoshi *et al.*[42]. Similarly, surface chemistry induced phase transformations have been studied and reported on in great detail[42,44,53,57,59-63]. Motivated by the need for synthesis and post-synthesis morphology control, these studies have provided significant insight into the interactions that occur between the surface of a ZnS nanoparticle and its environment and have provided conclusive evidence of surface induced phase transformations.

Table 2.1 – A summary of some synthesis methods and surfactants or solvents employed in the production of ZnS nanoparticles and the resulting sizes and phases.

Ref	Synthesis Technique	Surfactant	Size(s)	Phase	Characterization Technique(s)	Comments
[107]	Zinc acetate dihydrate and 1-thioglycerol dissolved in dimethyl formamide (DMF) combined with sodium sulphide nonahydrate dissolved in water. pH regulated with NaOH. Precipitation by addition of acetone or alcohol, washed with methanol and ether. Found to dissolve readily in water.	1-thioglycerol	1.8nm 2.5 nm 3.5 nm	ZB	XRD (powder) TEM (vacuum) EDAX UV-vis (water)	
[112]	Zinc chloride, sulphur powder, NaOH and deionised water refluxed. Sample centrifuged and washed with water. Stable ZnS nanoparticle powder obtained after drying.	None	18.2 nm (15nm to 20nm)	ZB	XRD SEMTEM PL (toluene)	

[110]	Hydrothermal decomposition from thiocynoto complexes. $ZnCl_2$ solution mixed with NH_4SCN, combined with distilled water and heated. White precipitate collected by filtration and washed repeatedly with absolute alcohol and distilled water.	None.	30 nm to 38 nm	ZB	XRD TEM	Higher synthesis temperature increased particle size.
[116]	$Zn(DDTC)_2$ prepared by precipitation from $Zn(CH_3COO)_2$ and sodium diethyldithiocarbamate ($(C_2H_5)_2NCS_2Na{\cdot}3H_2O$) in distilled water. ZnS nanocrystals obtained by subjecting precursor to heat treatment.	None.	2.8 nm to 6.6 nm	WZ	XRD XPS SEM TEM/SAED UV-vis (ethanol)	Aggregation observed in TEM
[118]	$Zn(DDTC)_2$ precipitate prepared from $ZnCl_2$ and $(C_2H_5)_2NCS_2Na{\cdot}3H_2O$ in distilled water. $Zn(DDTC)_2$ added to ethylene glycol	None.	4.5 nm	WZ	XRD FESEM TEM (ethanol) PL	FESEM reveals aggregation. Failed to form nanoparticles when using water or ethylenediamine instead of

	and heated by MW. Products separated by centrifuge, washed with ethanol and dried.					ethylene glycol. MW single-source precursor described as being fundamental to the formation of WZ structure.
[119]	Anhydrous $ZnCl_2$ and tertamethylammonium hydroxide dissolved in ethylene glycol (EG) mixed with thiourea dissolved in EG. ZnS nanoparticles separated by centrifuge and washed with acetone and alcohol.	None.	4.2 nm	WZ	UV-vis (ethanol) XRD TEM	WZ structure also obtained without TMAH and also with other polyols such as diethylene glycol and glycerol. Comments made regarding key role played by polyols.
[114]	$Zn(NO)_3{\cdot}6H_2o$ and L-cysteine ($HSCH_2CH(NH_2)COOH$) dissolved in deionised water and varying amounts of ethanolamine (EOA) or ethanediamine (EDA). Various temperatures and times were	None.		ZB (in water only). ZB (95˚C in H_2O/EDA.) WZ (200˚C in	TEM SEM XRD UV-vis PL	Discussion on the effect of surface-modifying reagents and growth kinetics vs. thermodynamics. ZnS nanostructured spheres assembled from various ZnS

	used. White precipitate separated by centrifuge and washed with ethanol.			H_2O/EDA) WZ (95˚C and 200 in H_2O/EOA.)		building blocks, such as QDs, nanosheets, nanorods, and "multimorphology" nanocrystals.
[43]	H_2S gas introduced into *N,N*-dimethylformamide solution of $Zn(CH_3COO)_2{\cdot}2H_2O$. N_2 gas used to purge solution of unreacted H_2S. DMF solution of organic compound such as thiol, carboxylic acid or phenol added to ZnS-DMF.	None.	3 nm	WZ converted to ZB when C_6F_5SH used.	HR-TEM FT-IR UV-vis EXAFS	Discussion on the effect of surface-modifying reagents. All thiols (pentafluorothiophenol, thiophenol, 1-decanethiol, 1-hexanethiol) induced WZ to ZB phase change.

2.4 Post-Synthesis Phase Transformations

Fujiwara, Hosokawa, Kanemoto, Murakoshi, Wada, Yanagida and others investigated the photocatalytic activity of ZnS nanoparticles[37,84-86], the influence of nanoparticle phase in this capacity[87,120], the nature of surface induced nanoparticle phase transitions[42,43] and the interaction of surfaces with organic solvents[45,46]. In so far as the stability of the nanoparticles and the causes of phase transitions are concerned, Hosokawa *et al.*[45] found that zinc atoms on the nanoparticle surfaces were solvated by the oxygen atoms in dimethylformamide (DMF, a common organic solvent used in ZnS nanoparticle production) and that the choice of zinc salt (the source of zinc) affected the coordination of the surface atoms thus affecting the efficiency of the DMF as a solvent, leading to varying degrees of surface stoichiometry. Further study by Fujiwara *et al.*[46] showed that the surface interaction of DMF molecules was dependent on the coexistent counteranions in solution. Murakoshi *et al.*[42] provided details of controlled phase transitions (WZ to ZB) induced by surface modifications at ambient temperature and pressure. This was achieved through the introduction of solvents. The results of Murakoshi concluded that the ability of a solvent to induce a phase change was related to its acid dissociation constant, or pK_a value. This was attributed to interaction of the dissociated anions of the respective organic molecule with the surface of the ZnS nanoparticle to form covalent or ionic bonds.

In contrast to the assumption that elevated temperatures were necessary to induce structural phase transformation, Zhang, Gilbert, Huang, Banfield and others observed reversible structural transformations in ZnS nanoparticles at room temperature[44]. These studies introduced methods for post-synthesis control of nanoparticle structure and even went so far as to suggest the use of the switching of the nanoparticle structure in the development of an environmental sensor. Reversible structural transformations at room temperature were induced by aggregation-disaggregation[56] and absorption-desorption of methanol and

water[44]. Since it is not possible to make step-wise observations in real experiments, these studies were supported by classical MD simulations of the interaction between methanol and water and the surface S and Zn ions. This part of the study showed that the surfaces of nanoparticles in methanol undergo reconstruction that penetrates several atomic layers, leading to a crystalline core surrounded by disordered arrangements. In contrast, water was found to decrease the interfacial free energy, thus increasing crystallinity throughout the nanoparticle (as shown in Figure 2.3). These effects were attributed to the orienting of the polar water molecules to permit hydrogen and oxygen bonding to the terminating S and Zn ions, providing strong interaction and a stabilising effect; whereas interactions with methanol where presumed to be lower owing to its lower molecular polarity.

2.5 Theory and Simulation

Hamad, Cristol, Catlow, Spano, Matxain and Ugalde[64-69] conducted first principles computational studies of ZnS clusters, surfaces and nucleation. A lattice statics and density functional theory (DFT) approach was taken to calculate surface energies in both ZB and WZ phases[64]. These calculations were used to find the low energy crystal morphologies following the Gibb's criteria[121] (via minimisation of the surface free energy), and predicted a dodecahedron shape for the ZB phase and a prismatic shape for the WZ phase. The dependency of these results on factors such as size, temperature and pressure and the effect of surface passivating species and aggregation states were not considered, but they demonstrate that "spherical" shapes are likely to be insufficient for describing the morphology of ZnS nanoparticle as they fail to account for the surface energy anisotropy.

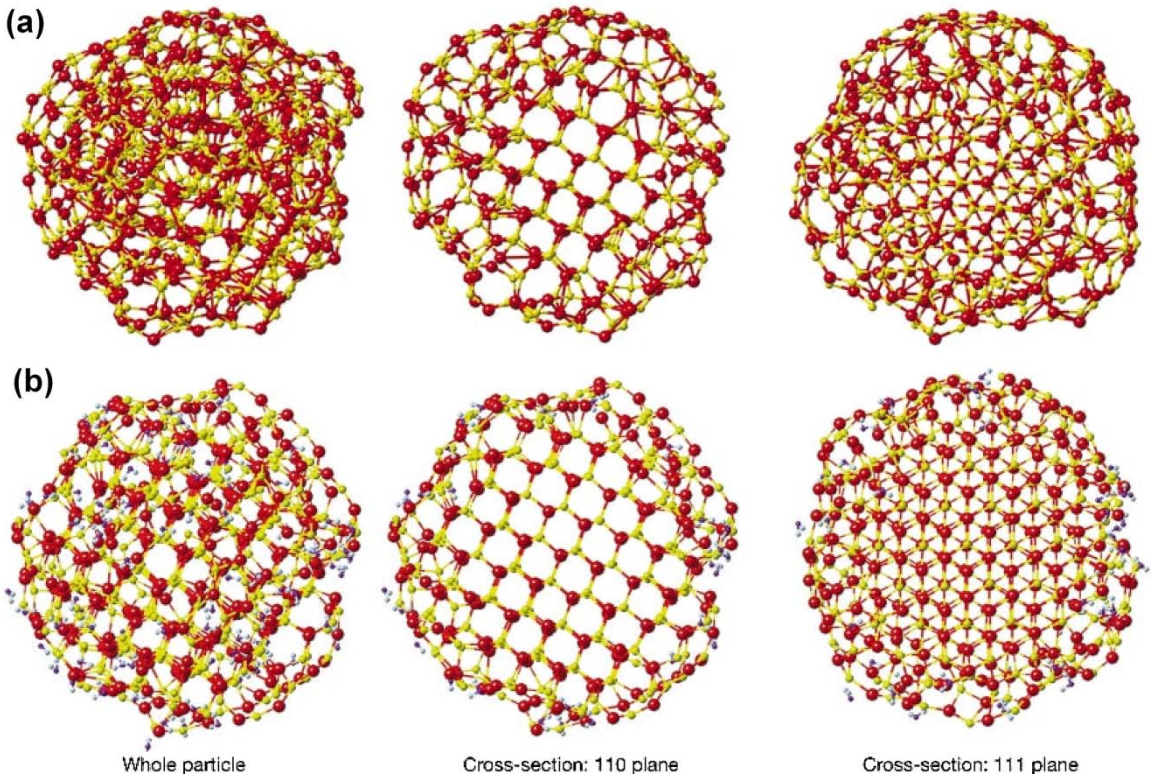

Figure 2.3 – Molecular dynamics prediction of the structure of a "spherical" 3 nm ZnS nanoparticle. (a) Without surface-bound water, and (b) with surface-bound water. Sulphur atoms are shown in yellow, zinc atoms are shown in red, oxygen atoms are shown in blue, and hydrogen atoms in light blue. The 3-D structures are shown in the left column, and cross-sections through central (110) and (111) planes are shown in the central and right columns, respectively. Reproduced with permission from reference 44, Nature Publishing Group © 2003.

The same authors also employed a simulated annealing method using classical inter-atomic potentials (supported by DFT), to find the best possible estimate of the global energy minimum of ZnS clusters with sizes ranging from 10 to 47 atoms[68]. This method produced 'bubble' clusters (appearing as hollow structures consisting of 4, 6 and 8 atom rings), where all the atoms in the structure are three-fold coordinated, as opposed to the tetrahedral four-fold coordination encountered in larger structures. Similar studies of n = 50 - 80 produced onion-like structures, where one bubble cluster was enclosed inside another with tetrahedral bonding between the two[65,69]. Further computational studies by this group on structures above this size (up to n = 512) predicted a BCT (zeolite) crystalline structure to be stable, although it is not encountered in the bulk[67] (see Figure 2.4). Examples of resultant structures are shown in Figure 2.5. The WZ phase was found to be only slightly energetically higher than the BCT

structure, and was expected to be lower in energy with solvation, while the ZB phase was predicted to be least stable (even though it is most stable in nature). It is possible that these discrepancies arise due to the limitations imposed by the structure set used in the simulations, and alternative shapes may yield different results. This is a common flaw of studies that are entirely computational, since decisions and choices must be made in regard to the virtual "sample set", and the consequences of these choices may be unknown. One way of overcoming this inherent weakness is to combine computational results with suitable theoretical modelling, to extend the range of applicability and sample a greater region of the relevant morphology-space.

Taking a theoretical approach, Li, Lian and Jiang recently investigated the transition temperatures between ZB and WZ nanoparticles by considering the energetic contributions of average surface energy, average surface stress and external pressure on the Gibb's free energy of a "spherical" ZnS nanoparticle[51]. In this study it was found that the temperature required to drive the transformation decreases with decreasing diameter, but increases with pressure. The relationship between the transformation temperature and nanoparticle diameter was in good agreement with experimental results[54] (as shown in Figure 2.6), but the study neglected to include a description of realistic polyhedral shapes such as those predicted in other works[64,65].

Despite a reasonable body of experimental, computational and theoretical studies concerning ZnS nanoparticle phase control, the exact relationship between the physical and chemical environment and the preferred morphology of ZnS nanoparticles remains poorly understood, as adequate connections between the various studies are still lacking. Although some of the important experimental phase-determining factors have been identified above, these factors are omitted from the computational and theoretical studies. While

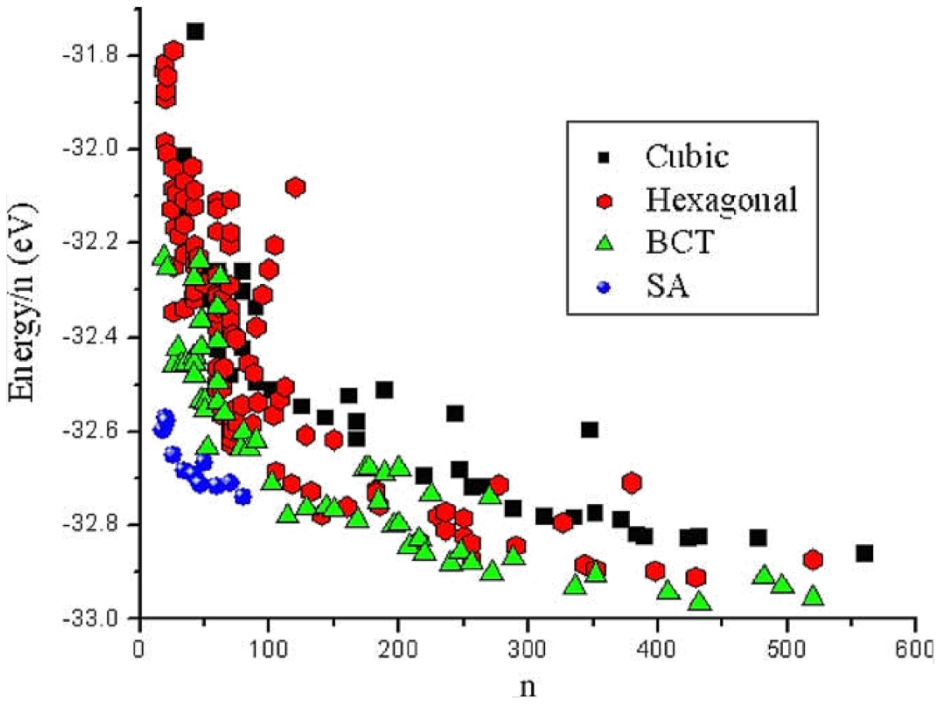

Figure 2.4 – Energies of geometry optimized clusters determined using IPEM techniques. The structure of the clusters is indicated in the legend. Reproduced with permission from reference 67, Elsevier © 2004.

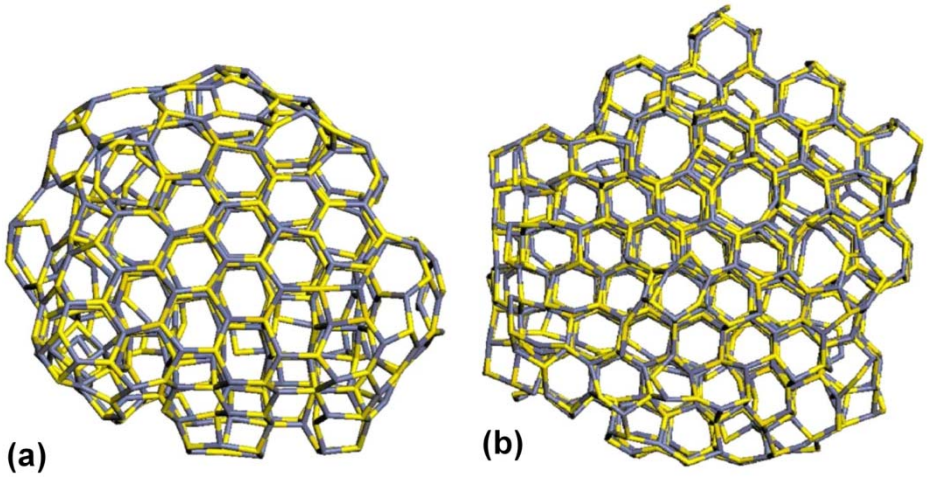

Figure 2.5 – Structures of two clusters, obtained with simulated annealing. (a) $(ZnS)_{256}$, (b) $(ZnS)_{512}$. Light gray sticks refer to sulphur and dark gray to zinc. Reproduced with permission from reference 67, Elsevier © 2004.

surface passivation was included in references 44 and 56, a very limited set of nanoparticles were simulated and polyhedral or WZ structures were omitted. A larger set of sizes, shapes and solid-phases were treated in references 64 to 69, but the surfaces were unpassivated and the sizes were still inconsistent with experiment. And finally, although the theoretically

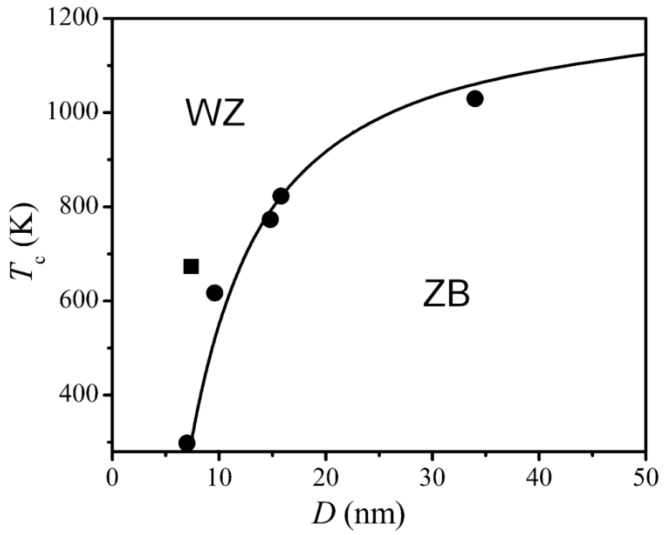

Figure 2.6 – Size-dependent critical temperature for the transformation between ZB and WZ ZnS phases, in a vacuum. The solid squares and solid circles indicate corresponding experimental results. Reproduced with permission from reference 51, Elsevier © 2008.

modelling in reference 51 considered a range of realistic temperatures and pressures, surface passivation and surface energy anisotropy was ignored. Each study was carefully undertaken, and delivers much useful information, but the goal of performing 'virtual experiments' that are consistent with experiment is still not possible.

2.6 Overview of Current Work

Nanomorphology prediction remains one of the most coveted but complex aims of nanotechnology today; one that ultimately lies in the motions and interactions of every particle in a nano-structure and its immediate environment. One approach that can help to shed some light on the problem is to map the stability of each solid phase in $<T,P,D>$ space (where T is the temperature, P is the external pressure and D is a measure of the characteristic size in the critical dimension), while accounting for changes in particle shape and variation in surface chemistry[70,122]. The development of a nano-scale phase diagram for ZnS may provide a way of rapidly assessing the multi-parameter phase-space that this problem occupies, and serve to highlight the size, temperature, pressure and chemical regimes that require further experimental or computational attention.

For bulk materials, a phase map is produced by altering one variable, such as pressure, while holding all others constant and measuring an independent property such as resistivity. On the nanoscale however, the phase space is multi-dimensional, making experimental exploration a momentous task. In addition, the experimental difficulties involved in holding all but one factor constant make such a task appear practically impossible to achieve.

From a theoretical standpoint, these phase transformations are highly efficient, indicating a low kinetic transformation barrier and dominant thermodynamic influences. Ignoring the effects of kinetics, it is suggested that rapid phase prediction could be achieved through *ab inito* calculation of the thermodynamic properties and equilibrium morphologies, and subsequent mapping of these morphologies in the domain of the dominant thermodynamic variables (size, temperature and pressure). The following body of work attempts to accomplish this aim, in order to facilitate phase prediction in a way that is not currently available, and in turn assist in the intelligent design of stable and efficient nano-devices and the formation of appropriate material safety guidelines.

Chapter 3. Theory and Methods

3.1 Overview

The equilibrium morphologies of ZnS nanoparticles can be determined with a high degree of accuracy using a modern theoretical method which models nanoparticles based on a sum of their mesoscale thermodynamic properties. This model contains material-, phase- and shape-dependent terms. Some of these terms (density and molar mass for example) can be found in literature. Others, such as surface energies and stresses must be calculated, using the same *ab inito* or empirical methods to ensure that their relative accuracy is consistent. Shape dependent terms such as surface-to-volume ratio and facet weighting factors are determined geometrically.

In the present study, density functional theory (DFT) was used to calculate parameters such as surface energies and stresses. This is currently the most common method for calculations of electronic structures and total energies as it is considered highly accurate with reasonable demand on computational resources. However, as discussed below, a range of DFT methods exist and their relative accuracy for any given system cannot be known without comparative testing. Therefore, prior to performing the calculations necessary for the thermodynamic modelling, a comparison of DFT methods was performed by calculating known bulk ZnS properties and comparing the results to experiment (Chapter 4). The most appropriate method was then applied to the remainder of the study.

It is important to point out that the DFT effectively calculates properties at zero temperature. This means that the Gibbs free energy, used as a measure of thermodynamic stability, is effectively a free energy of formation, equivalent to the enthalpy for formation. This has implications for the applicability of some modelling results to real experiments. As such, the results reported in Chapters 5 and 6 are more closely related to low-temperature

quasi-equilibrium conditions, and may have limited applicability to cases where ZnS nanostructures are grown at high temperature. In Chapters 7 and 8 *ab initio* thermodynamic techniques are used to treat surrounding gas phase temperatures and partial pressures for polar faceted nanoparticles, however intrinsic entropic lattice vibrations associated with the nanoparticles themselves are not included.

3.2 Shape-Dependent Thermodynamic Modelling

The thermodynamic model used is based on a geometric summation of the Gibbs free energy[123,124], which by definition is minimum at equilibrium. This model considers contributions from the bulk phase, anisotropic surface energies, anisotropic surface stresses (causing volume dilations), external pressure, and the reduction of the surface-to-volume ratio caused by high energy facets. A complete discussion of this method is found elsewhere[123,124] and has been successful applied to the study of transition metal oxides and sulphides[125-130].

The Gibbs free energy is defined as:

$$G = U + pV - TS \qquad \text{Eq 3.1}$$

where U is the internal energy (the sum of the kinetic and potential energy components of the system), p is pressure, V is volume, T is temperature and S is entropy. For macro-scale materials, the free energy is dominated by atomic arrangements in the bulk, which make up the vast majority of the material. However, when dimensions are reduced to the nanoscale, the surface-to-volume ratio increases and the energies of atomic arrangements surrounding the bulk become significant. For nanoparticles in the solid-amorphous or liquid phase, this constitutes random surface arrangements; while in crystalline nanoparticles, facets are formed and the final shape can be classified in terms of the resultant surfaces, edges or corners. Therefore, the free energy for a nanoparticle in phase x may be defined as:

$$G_x^0 = G_x^{bulk} + G_x^{surface} + G_x^{edges} + G_x^{corners} \quad \text{Eq 3.2}$$

Complexity and computational expense associated with calculating input parameters is significantly reduced by restricting the results of modelling to nanoparticle sizes above $\langle D \rangle$ = 3 nm. Above this size, the edge and corner energies (the final two terms in Eq 3.2) can be ignored as the atoms residing in these arrangements make up an insignificant fraction of the whole, as demonstrated in reference 124, and the contribution from these terms scale as $1/R^2$ and $1/R^3$, respectively. There are pre-existing studies which explicitly model small ZnS nanoparticles, many of which are entirely first principles techniques[64-69], and these are more applicable at sizes less than 3 nm. In addition to this, a comparison of modelling results incorporating each term in Equation 3.2 and separate, explicit DFT calculations has already been performed[123] and the uncertainty associated with the omission of these terms has been quantified. Based on these previous studies, the need for thermodynamic modelling below $\langle D \rangle$ = 3 nm is negated, and this project is restricted to particles greater than this size. Eq 3.2 is therefore reduced to:

$$G_x^o = G_x^{bulk} + G_x^{surface} \quad \text{Eq 3.3}$$

The first term G_x^{bulk} is defined as the standard Gibbs free energy of formation, $\Delta_f G_x^o\ (T)$ (the temperature-dependent change in free energy associated with the formation of one mole of a substance from the constituent elements in their standard states). At zero temperature, this is equivalent to the standard enthalpy of formation, ΔH_f°. This quantity can be calculated, using DFT for example, or may be found in literature relating to experiments at finite temperature[131,132].

The remaining free energy term in Eq 3.3, the total temperature-dependent surface free energy, can be simply expressed as follows:

$$G_x^{surface} = A\gamma_x(T) \quad \text{Eq 3.4}$$

where A is the surface area and γ_x is the temperature-dependent surface energy per unit area of a material in phase x. The effects of surface energy anisotropy are included by modifying Eq 3.4 as follows:

$$G_x^{surface} = \sum_i A_i \gamma_{x,i}(T) \qquad \text{Eq 3.5}$$

where the total surface free energy is now a sum over the product of the individual surface-specific surface-areas and surface-specific free energies (per unit area) for each surface i (in phase x). This is consistent with the Wulff construction[[133]], which is an exact and efficient method for finding minimum surface energy configurations when applied to bulk objects, and has long been used to determine the shape of water droplets as well as bulk and nanoscale crystals without any size dependence. The current method considers additional contributions to the free energy, which can be significant in determining morphologies below ~ 50 nm but are ignored under the Wulff construction.

Firstly, at sizes below 50 nm the surface-to-volume ratio increases dramatically, to the extent that the formation of higher energy surfaces, which would contribute positively to the free energy in Eq 3.5, may lower the total free energy if they sufficiently moderate this shape-dependent quality (at larger sizes the surface-to-volume ratio decreases towards the bulk limit and the shape converges to the Wulff construction). By including a surface-to-volume ratio term any thermodynamic advantage gained by introducing higher energy facets can be assessed. The shape-dependent surface-to-volume ratio term, q, in conjunction with the material-dependent molar mass M and the phase-dependent density ρ_x (equivalent to the surface area per mole), and are substituted into the model in place of the surface area term in Eq 3.5, to give an expression for the free energy in joules per mole, as follows:

$$G_x^{surface} = \frac{M}{\rho_x} q \sum_i f_i \gamma_{x,i}(T) \qquad \text{Eq 3.6}$$

where f_i is a weighting factor defined such that:

$$\sum_i f_i = 1 \qquad \text{Eq 3.7}$$

On the nanoscale, the surface-to-volume ratio of objects can be significantly affected by volume dilations caused by surface stress, σ_x. This will be an anisotropic effect if more than one type of surface is present, as stress in the plane of the surface varies with type. To include the influence of surface tension in the model, the surface-stress-related volume dilation, e, is defined in terms of an effective pressure P_{eff}. In general, the volume dilation caused by an applied pressure is modulated by the bulk modulus B_0, according to the following relationship:

$$\frac{\Delta V}{V} = e = \frac{P_{eff}}{B_0} \qquad \text{Eq 3.8}$$

Negative volume dilation increases the surface-to-volume ratio, so this affect is included in the Eq 3.6 model as follows:

$$G_x^{surface} = \frac{M}{\rho_x}(1-e)q\sum_i f_i \gamma_{x,i}(T) \qquad \text{Eq 3.9}$$

The effective pressure term in Eq 3.8 can be approximated by the Laplace-Young equation which defines the relationship between surface tension and mean particle radius $\langle R \rangle$, as follows:

$$P_{eff} = \frac{2\sigma_x}{\langle R \rangle} \qquad \text{Eq 3.10}$$

Surface tension anisotropy is included by modifying Eq 3.10 as follows:

$$P_{eff} = \frac{2\sum_i f_i \sigma_{x,i}}{\langle R \rangle} \qquad \text{Eq 3.11}$$

where the total surface tension is now a sum over the surface-specific surface tensions (per unit area) for each surface i (in phase x) and f_i is defined in Eq 3.7.

Combining Eqs 3.11, 3.8, 3.9 and 3.2, and including the effect of external, atmospheric pressure (noting the convention of a positive external pressure causing negative volume dilation) the shape-dependent expression for the Gibbs free energy per mole, is as follows:

$$G_x^o = \Delta_f G_x^o + \frac{M}{\rho_x}\left[1 - \frac{2\sum_i f_i\,\sigma_{x,i}}{\langle R\rangle} + \frac{P_{ext}}{B_0}\right] q \sum_i f_i\,\gamma_{x,i}(T) \qquad \text{Eq 3.12}$$

Eq 3.12 was used to model ZnS nanoparticles in the zinc blende (ZB), wurtzite (WZ) and amorphous (AM) phases in the size range <*D*> = 3.0 – 100 nm, with the results reported in Chapters 5 – 8.

3.3 *Ab Inito* Thermodynamics

The gap between low-temperature, zero-pressure calculations in DFT and experiments conducted at finite temperature and pressure was bridged through the use of *ab initio* thermodynamics[134,135]. These methods employ DFT total energy calculations to form a potential energy surface and form an expression for the Gibbs free energy $G(T,P,N_{Zn},N_S)$, which can then be used to determine equilibrium structures based on local and global energy minima.

The surface formation energy γ_i can be defined in terms of the partial pressure (or supersaturation) of sulphur $P(S)$[129], beginning with:

$$\gamma_i = \frac{1}{2A_i}\left[E_i(N_{ZnS}) - N_{ZnS}\mu_{ZnS,bulk} + P\Delta V - T\Delta S\right] \qquad \text{Eq 3.13}$$

where $E_i(N_{ZnS})$ is the total energy of a fully relaxed surface slab of orientation *i* (containing N_{ZnS} formula units), A_i is the explicit area of the slab, ΔV is the volume change due to surface relaxation and should be relatively small (this should not be confused with *volume dilation* caused by *surface stress*, as defined in Eq 3.11), and ΔS is the entropy change which is normally dominated by the vibrational entropy from phonons. In general $-T\Delta S$ lowers the

surface free energies as T increases, but changes in the relative ordering are not expected, especially at temperatures far below the melting point. In this study, the last two terms will be disregarded, as we are concerned only with the temperature and pressure of the surrounding environment.

The second term in Eq 3.13 can be further decomposed into the chemical potential of both Zn (μ_{Zn}) and the chemical potential of S (μ_S), based on one eighth of the S_8 molecule (which retains the structure of the bulk). This is accompanied by N_{Zn} and N_S describing the numbers of the corresponding atoms in the slab. When a ZnS surface reaches its thermodynamic equilibrium, the sum of the chemical potentials $\mu_{Zn} + \mu_S$ is equal to the chemical potential of a crystalline ZnS ($\mu_{ZnS,bulk}$), and $\Delta G = 0$ for compound formation or decomposition, according to:

$$\mu_{ZnS,bulk} = \mu_{Zn,bulk} + \mu_S = \mu_{Zn,surface} \qquad \text{Eq 3.14}$$

so that,

$$\gamma_i = \frac{1}{2A_i}\left[E_i(N_{ZnS}) - N_{ZnS}\mu_{ZnS,bulk} + (N_{Zn} - N_S)\mu_S\right] \qquad \text{Eq 3.15}$$

To introduce the pressure P(S), μ_S can be related to the chemical potentials of crystalline ZnS and Zn by the bulk formation energy, $\Delta H_{f,bulk}$, according to:

$$\mu_S = \mu_{ZnS,bulk} - \mu_{Zn,bulk} - \Delta H_{f,bulk} \qquad \text{Eq 3.16}$$

At the standard state,

$$\mu_S = \mu_S^{o} + k_B T \ln\frac{P(S)}{P^{o}(S)} = \left[\mu_{ZnS,bulk}^{o} - \mu_{Zn,bulk}^{o} - \Delta H_{f,bulk}^{o}\right] + k_B T \ln\frac{P(S)}{P^{o}(S)} \qquad \text{Eq 3.17}$$

where k_B is Boltzmann's constant and T is temperature. The pressure terms ln$P$(S)/ln$P$°(S) are written above and in later chapters as ln$P$(S) for the sake of brevity.

Combining these equations gives a description of the surface energy that can be solved for various sulphur supersaturations and temperatures,

$$\gamma_i(P(S),T) = \frac{1}{2A_i}[E_i - N_{ZnS}\mu_{ZnS,bulk} + (N_{Zn} - N_S)\cdot$$

$$\left(\mu^{o}_{ZnS,bulk} - \mu^{o}_{Zn,bulk} - \Delta H^{o}_{f,bulk}\right)$$

$$+(N_{Zn} - N_S)k_B T \ln\frac{P(S)}{P^{o}(S)}] \qquad \text{Eq 3.18}$$

This will be valid for temperatures well below the melting point (as described above), and in the range of applicability for ln*P*(S). The range of ln*P*(S) is set by assigning the conditions that forbids the formation of pure Zn, $\mu_{ZnS,surface} < \mu^{o}_{ZnS,bulk}$, and the loss of S, $\mu_S < \mu^{o}_S$, so that:

$$\frac{\Delta H^{o}_{f,bulk}}{k_B T} < \ln\frac{P(S)}{P^{o}(S)} < 0 \qquad \text{Eq 3.19}$$

This robust method is well established, and allows for different chemical reactions, depending upon the definition of $\mu^{o}_{ZnS,bulk}$ and μ^{o}_S.

3.4 Density Functional Theory

Density functional theory (DFT) is built on proof provided by Hohenberg and Kohn that the total energy of an *N*-electron system is a unique functional of the electron density and that the exact ground state density of the system is that which minimises this functional[136]. This was further developed by Kohn and Sham to provide a means of using the electron density as the central quantity for performing ground state energy calculations by treating the interacting electrons as non-interacting particles in an effective potential[137].

Over the past forty years, as the method has developed and increased in accuracy, it has become the first choice for *ab initio* structure/property and quantum chemistry calculations. Computational costs are greatly reduced when compared to other approaches, such as the many-electron, Hartree-Fock based methods. This comes as a result of a one-to-one mapping

of the many-body interacting system to the single particle in an effective potential, thereby reducing ground state energy calculations from 3*N* to 3 dimensional problems. Over the last 15 years DFT has been applied to study a large range of material systems and properties, including ZnS[138-147] and CdS[148,149,150].

In this study, DFT calculations of ZnS surfaces were used to determine the surface energies and stresses of surface facets found in XRD experiments of ZnS nanoparticles. These DFT calculations were implemented via the Vienna *Ab initio* Simulation Package (VASP)[151,152].

3.5 Calculating the Bulk Properties of ZnS

3.5.1 Bulk and elastic moduli

The bulk moduli and pressure derivatives of the ZB and WZ phases were obtained by varying the unit cell volume and calculating the total energy of the cell. These energies were fitted to the third-order Birch-Murnaghan equation of state[153], as follows,

$$E(V) = E_0 + \frac{9}{8} B_0 V_0 \left[\left(\frac{V_0}{V} \right)^{\frac{2}{3}} - 1 \right]^2 + \frac{9}{16} B_0 (B_0^{'} - 4) V_0 \left[\left(\frac{V_0}{V} \right)^{\frac{2}{3}} - 1 \right]^3 \qquad \text{Eq 3.20}$$

where E_0 is the unit-cell energy, V_0 the unit-cell volume, B_0 the bulk modulus and $B_0^{'}$ the pressure derivative of the bulk modulus, all at zero pressure.

For cubic crystals the elastic constants are the second derivatives of the energy density with respect to specific strain components. There are three independent constants: C_{11}; C_{12}; and C_{44}. The C_{11} elastic constant can be determined by applying a small elastic strain in the <100> direction of the lattice (while keeping the lattice fixed in the orthogonal directions). If

δ represents strain along the <100> direction and $\frac{\partial^2 E}{\partial \delta^2}$ the second derivative of the total lattice energy with respect to this strain, the elastic constant C_{11} can be determined as follows,

$$C_{11} = \frac{1}{V_0} \cdot \frac{\partial^2 E}{\partial \delta^2} = \frac{2b}{V_0} \qquad \text{Eq 3.21}$$

where V_o is the equilibrium lattice volume and b is the quadratic coefficient in the polynomial fit to the curve of E vs δ.

When the bulk modulus and C_{11} elastic constant of a cubic crystal are known, the C_{12} elastic constant can be determined from the following relationship[154],

$$B_0 = \frac{C_{11} - 2C_{12}}{3} \qquad \text{Eq 3.22}$$

For hexagonal crystals, a symmetry-preserving distortion in the size of the basal plane (represented by lattice constant a), keeping the c-axis fixed, allows the elastic constant $C_{11}+C_{12}$ to be determined[155] according to the following expression,

$$C_{11} + C_{12} = \frac{{a_0}^2}{2V_0} \frac{\partial^2 E}{\partial a^2} \qquad \text{Eq 3.23}$$

where a_0 is the equilibrium value of the 'a' lattice parameter in the hexagonal crystal and V_0 is the equilibrium lattice volume.

The C_{33} elastic constant is determined by varying the c-axis while keeping the basal plane ('a' lattice parameter) fixed[155], according to the following expression,

$$C_{33} = \frac{{c_0}^2}{2V_0} \frac{\partial^2 E}{\partial c^2} \qquad \text{Eq 3.24}$$

where c_0 is the equilibrium value of the 'c' lattice parameter of the hexagonal crystal.

3.5.2 Energetic properties

The ZB and WZ phases of ZnS can be formed according to the following simple chemical reaction,

$$Zn + S \rightarrow ZnS \qquad \text{Eq 3.25}$$

While in reality this is the end point of a series of reactions, as described in reference[156], it is far more tractable computationally to consider the effective reaction as per Eq 3.25.

The enthalpy of formation for this reaction can be determined as follows,

$$\Delta H_{ZnS} = E_{ZnS} - (N_{Zn}\mu_{Zn} + N_S\mu_S) \qquad \text{Eq 3.26}$$

where N_i is the number of atoms of element i in the relaxed structure of ZnS and μ_i is the chemical potential of element i. Since only the final stage of the reaction sequence is treated explicitly, it is important to select μ_i carefully to match the experimental conditions. In this case Zn was calculated in its hexagonal bulk phase and S in its molecular form. However, since oxygen is not included in the reaction cycle, results for two different S molecules are included for comparison: S_2 and S_8.

The chemical potential of zinc was calculated in the hexagonal phase as follows,

$$\mu_{Zn} = \frac{1}{N} E_{Zn}^{hex} \qquad \text{Eq 3.27}$$

where E_{Zn}^{hex} is the DFT total energy of the bulk Zn metal (which has a hexagonal structure $P6_3/mmc$, space group 194) and N is the number of zinc atoms in the cell.

The chemical potential of sulphur was calculated using the cyclo-S_8 (orthorombic α-sulfur) and S_2 molecules, according to Eqs 3.28 and 3.29, respectively,

$$\mu_S(S_8) = \frac{1}{8} E_{S_8}, \qquad \text{Eq 3.28}$$

$$\mu_S(S_2) = \frac{1}{2} E_{S_2} \qquad \text{Eq 3.29}$$

where E_{S_8} and E_{S_2} are the DFT total energies of the S_8 and S_2 molecules respectively.

Chapter 4. A Comparative Density Functional Theory Investigation of the Mechanical and Energetic Properties of ZnS

4.1 Introduction

Over the past decade applications of theoretical modelling for materials have been broadening and techniques adopted more frequently as improvements in computational resources, software implementations and theoretical methodology are realised. Density functional theory (DFT), an *ab initio* ground state electronic structure method, has become the method of choice for calculating electronic ground state and mechanical properties[136,137]. DFT theoretically maps the interaction of a many-electron system onto that of a single electron in an effective exchange-correlation (XC) potential. However the exact nature of the XC energy is not known and may be approximated by one of two methods – the Local Density Approximation (LDA) and the Generalised Gradient Approximation (GGA)[157-159]. Due to the number of LDA and GGA functionals available and their relative accuracy and computational expense, DFT studies must be preceded by rigorous testing to establish which functional will provide the best results and the least trade-off between accuracy and computational cost.

In this chapter some common LDA and GGA energy functionals are employed to calculate bulk material properties belonging to ZnS in the ZB and WZ phases, and the results compared for accuracy and efficiency. A review is made of the necessary mechanical and energetic properties of ZnS and descriptions given for the functionals and the theoretical methods used to calculate these properties. Total energy and force convergence for each approach is reported, followed by the results of current and previous theoretical calculations and experimental studies of the properties described where they are available.

While this chapter is important for further DFT calculations in later chapters, it is important to know that the conclusions made with regard to the optimal functional/basis set combination (minimising the trade-off between accuracy and computational expense) *are valid for the ZnS material only and not necessarily other materials*. However the method described here, for determining the optimal functional/basis set, can be applied to other systems; therefore might be relevant to other materials in that regard and may serve as a guide to accomplishing similar tasks. The work presented in this chapter was published in reference 160.

4.1.1 Atomic arrangements of zinc sulphide

At standard temperature and pressure (STP) ZnS is stable in the ZB solid crystalline phase, otherwise known as sphalerite or the B3 phase. The ZB phase belongs to space group 216, possessing a dual basis, face-centred cubic structure with Zn occupying the Wyckoff position (0,0,0) and S at (¼,¼,¼) where neither atom possesses any internal degrees of freedom. Both zinc and sulphur atoms are tetrahedrally coordinated and the ZnS dimers are stacked in an ABCABC arrangement. A meta-stable WZ structure, also described as the B4 phase, exists at STP and becomes more stable than the ZB phase above 1020˚C. The WZ structure belongs to space group 186 with Zn at (⅓,⅔,0) and S at (⅓,⅔,⅜) where, in this case, both the Zn and S atoms possess an internal degree of freedom along the *z*-axis. The ZnS dimers are stacked in an ABAB arrangement which produces a hexagonal close-packed system with tetrahedral bonding. These crystal structures are illustrated in Figure 2.1. At high pressures (above ~15 GPa) the rocksalt phase exists and the Cinnabar phase emerges above ~65 GPa. In nanoparticle form a complex combination of factors are responsible for determining the thermodynamically preferred phase of ZnS. Experimental observations reveal ZB and WZ as the dominant phases at STP[42,48,44,56,60,107,114]. Experimentally

determined mechanical properties and other theoretical calculations of this material for the ZB and WZ phases are compared to the results of DFT calculations below.

4.2 Method

To sample a range of commonly employed *ab intio* methods, DFT calculations were performed using the plane-wave basis set simulation package VASP, with the Perdew-Wang (PW91)[159] and Perdew-Burke-Ernzerhof (PBE)[158] GGA functionals, and the Ceperly-Alder (CA)[161] LDA functional. Plane Augmented Wave (PAW) pseudopotentials were used with all functionals, and an additional ultrasoft pseudopotential (USPP) was used with the PW91 functional. For each XC and pseudopotential combination total energy convergence with respect to basis set size was determined by calculating the total energy at increasingly larger plane-wave energy cut-offs (corresponding to larger basis set sizes). A summary of the overarching methodology is shown in Table 4.1. The notation used to abbreviate the combination of DFT approximation, XC functional, pseudopotential and basis set size used in this paper will henceforth be referred to in the manner as described in the final row of Table 4.1 (Notation) with the plane-wave energy cut-off given at the end of the notation. For example, a combination of the PBE form of the GGA with a PAW pseudopotential and a basis set size limited to a plane-wave energy cut-off of 300eV is referred to as PBE|PAW|300, or PBE|PAW when the basis set size is not relevant.

For simulations of this type, computational cost scales with basis set size, which is limited to the maximum plane-wave energy cut-off. For this reason it is desirable to use a low energy cut-off (small basis set) without reducing the accuracy of the results substantially. In practise, a compromise must be reached between computational cost and accuracy.

Table 4.1 – Summary of methodology and notation convention.

Ab initio Method	DFT			
Density Approximation	LDA	GGA		
XC Hamiltonian	CA	PBE	PW91	
Pseudopotential	PAW	PAW	PAW	USPP
Plane-wave basis set kinetic energy cut-off (eV)	325 400 425 500	325 360 420 470 500	325 360 425 500	275 300 500
Notation	LDA|PAW	PBE|PAW	PW91|PAW	PW91|USPP

Adequate basis set size is particularly important when calculating mechanical properties such as elastic constants, because the plane-wave density changes during volumetric dilations. To test the effect of plane-wave energy cut-off on accuracy and cost, each structure was fully relaxed (to a convergence of 10^{-4} eV) at increasing energy cut-offs using a quasi-Newton algorithm (RMM-DIIS) to relax the ions. This was followed by static, single-point energy calculations. Following the results of these tests, bulk properties in the ZB phase were calculated with plane-wave energy cut-offs of 400, 425 and 500 eV using LDA|PAW; 360, 420, 470 and 500 eV using PBE|PAW; 360, 425 and 500 eV using PW91|PAW; and 300 and 500 eV using PW91|USPP. These points correspond to plateau regions in total energy with respect to plane-wave energy cut-off (which, as stated above, is critical for accurate mechanical property calculations involving volume dilations). Bulk

properties in the WZ phase were calculated with plane-wave energy cut-offs of 325 and 500 eV using all DFT approaches except PW91|USPP which was tested at 275 and 500 eV, due to the relatively small basis set size required to achieve convergence.

The Brillouin zone was sampled using a Monkhorst-Pack scheme generated *k*-point mesh, centred on the gamma point to allow sampling of hexagonal as well as cubic cells. Tests for total energy convergence with respect to *k*-points was performed at a number of basis-set sizes, beginning with an 8x8x8 mesh and increasing until total energy had converged to within 10^{-2} eV.

4.3 Results

4.3.1 ZB structure

Figure 4.1 shows the total energy of geometry optimised ZB structures as a function of plane-wave energy cut-off for each DFT approach. In each case, variation in the total energy about the 500 eV cut-off point is minor, indicating that 500 eV is a suitable plane wave cut-off for calculating the elastic moduli (which require energies to be calculated over small volume changes). However, minor plateaus in the total energy were produced at lower cut-offs of 350 eV using PBE|PAW and 300 eV using PW91|USPP. These cut-offs could therefore also be used with lower computational cost. In general, the total energy calculated using LDA|PAW and PW91|PAW decreased steadily from 300 eV to 500 eV with a gradient of -1×10^{-3} until convergence was effectively achieved at 500 eV with a spread thereafter of 1 and 5 meV, respectively.

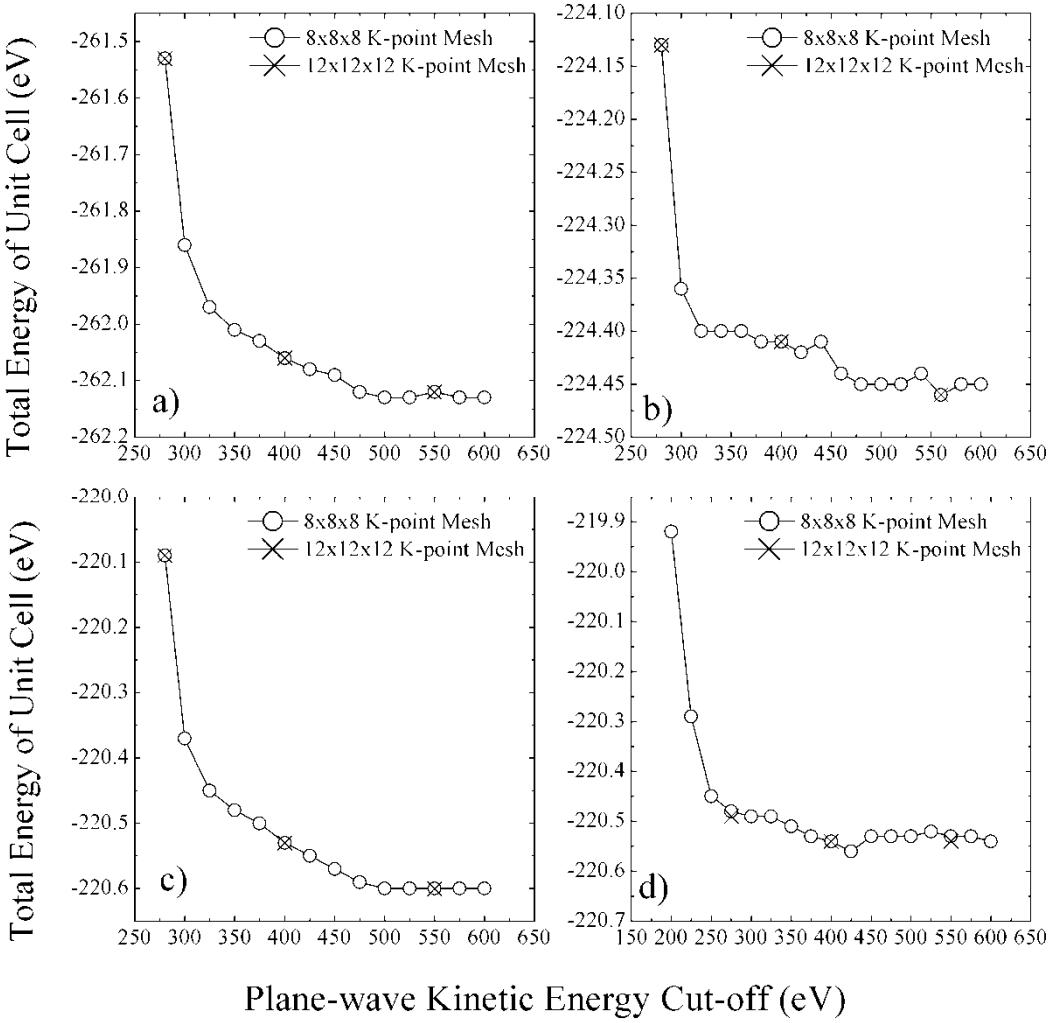

Figure 4.1 – Total energy as a function of plane-wave energy cut-off for the ZB structure using (a) LDA|PAW, (b) PBE|PAW, (c) PW91|PAW and (d) PW91|USPP with 8x8x8 (○) and 12x12x12 (X) *k*-point mesh sampling. Data lines are for visual guidance only.

With regard to testing for total energy convergence with respect to *k*-points, increasing the sampling mesh from 8x8x8 to 12x12x12 produced a change in energy of less than 10^{-2} eV. Therefore an 8x8x8 *k*-point mesh was found to be adequate for sampling the Brillouin zone (Figure 4.1).

Table 4.2 – Summary of bulk constant calculations for the Zinc Blende (ZB) structure. The total memory required (Mem Req) refers to a single static point energy calculation of the fully relaxed structure (in gigabytes).

Method	a (Å)	B_o (GPa)	B_o'	C_{11} (GPa)	C_{12} (GPa)	E/N_{fu} (eV)	ΔH_f (S_8) (kj/mol)	ΔH_f (S_2) (kj/mol)	Mem Req (GB)
LDA|PAW|400	5.300	86.179	4.517	117.485	70.526	-8.190	-176.22	-273.13	10.22
LDA|PAW|425	5.302	86.541	3.954	117.175	71.223	-8.190	-176.51	-276.26	10.84
LDA|PAW|500	5.304	85.897	4.632	116.331	70.680	-8.192	-176.56	-276.14	13.43
Other LDA	5.335[a]	83.7[a]	4.2[a]	123.7[a]	62.1[a]				
	5.328[b]	83.8[b]	4.5[b]	115.8[b]	72[b]				
	5.342[c]	89.67[c]	4.44[c]	118[c]	72[c]				
	5.339[d]	93.12[d]	4.63[d]						
	5.352[e]	83.1[e]	4.43[e]						
		82.0[f]	4.20[f]						
		84.2[g]	4.3[g]						
GGA|PBE|PAW|360	5.445	69.092	4.441	97.180	55.048	-7.013	-157.80	-238.69	9.16
GGA|PBE|PAW|420	5.443	69.030	4.527	96.649	55.220	-7.017	-157.66	-241.58	10.94
GGA|PBE|PAW|470	5.449	69.109	4.184	96.047	55.640	-7.018	-157.66	-241.59	13.09
GGA|PBE|PAW|500	5.448	68.550	4.520	94.780	55.435	-7.018	-157.88	-241.83	13.69
Other PBE	5.449[h]	70.020[h]	4.413[h]	97.206[h]	56.427[h]				
GGA|PW91|PAW|360	5.438	69.902	4.449	98.627	55.540	-6.894	-163.10	-246.99	9.04
GGA|PW91|PAW|425	5.437	69.876	4.404	97.786	55.922	-6.895	-162.86	-246.99	10.28
GGA|PW91|PAW|500	5.443	69.930	4.455	97.614	56.089	-6.897	-163.65	-247.82	13.37
Other GGA|PW91|PAW	5.60[i]	66.78[i]	3.95[i]						
GGA|PW91|USPP|300	5.446	69.591	5.481	95.052	56.860	-6.890	-167.87	-244.37	8.11
GGA|PW91|USPP|500	5.450	68.775	4.810	92.680	56.822	-6.891	-168.20	-247.40	13.97
Other GGA|PW91|USPP	5.404[j]	71.22[j]	4.705[j]	99.6[j]	57.0[j]				
Experimental	5.4102[l]	78.0[k]	4.91[l],	104.6[k]	65.3[k]		-206.53[n]		
		74.8[l]	4[m]						
	5.395[m]	79.5[m]							
	5.410[m]								

[a] LDA FP-LMTO[138]; [b] LDA Troullier-Martins[139]; [c] LDA FP-APW+lo[140];
[d] LDA LSDA FP-LAPW[141]; [e] LDA PP-PW[142]; [f] LDA LMTO[143]; [g] LDA Troullier-Martins[144];
[h] GGA PAW PBE[145]; [i] GGA PAW PW9[146]; [j] GGA PAW PW91[147]; [k] Expt.[162]; [l] Expt.[50];
[m] Expt.[163]; [n] Expt.[164]

The results of lattice constant calculations for the ZB phase are shown Table 4.2 along with theoretical and experimental results from other, previous studies. The LDA|PAW approach produced lattice constants around 5.302 Å, which is smaller than the average experimental value of 5.405 Å but consistent with other LDA calculations. In contrast, we find that the GGA calculations produced lattice constants ranging from 5.437 – 5.450 Å, which is larger than but (compared to LDA) in better agreement with the reported experimental values. Although the differences were minor, when compared to experimental values the PW91|USPP approach produced the least accurate lattice constants of 5.446 and

5.450 Å, followed by the PBE|PAW approach with 5.443 – 5.449 Å, with the most accurate by a small margin being the PW91|PAW approach with slightly smaller lattice constants of 5.437 – 5.443 Å, for similar plane-wave energy cut-offs. None of the approaches produced better comparison with experimental values of the lattice constant with increased plane-wave energy cut-off.

With respect to calculations of the bulk mechanical properties, Figure 4.2 indicates the total lattice energy values for the ZB phase with respect to minor changes in cell volume, for all functional/basis set combinations. As expected, in each case the DFT lattice energy varies quadratically for small distortions about the equilibrium volume. The results shown in Figure 4.2 were used to determine the bulk modulus and pressure derivative of the bulk modulus for each DFT approach, according to Eq 3.20. These results are shown in Table 4.2 along with a list of other theoretical and experimental values. The average experimental value for the bulk modulus in Table 4.2 is 77.4 GPa. The LDA|PAW approach produced bulk modulus values of ~ 86 GPa, which is ~ 10% larger than the experimental average. Increasing the plane-wave energy cut-off provided no significant increase in accuracy.

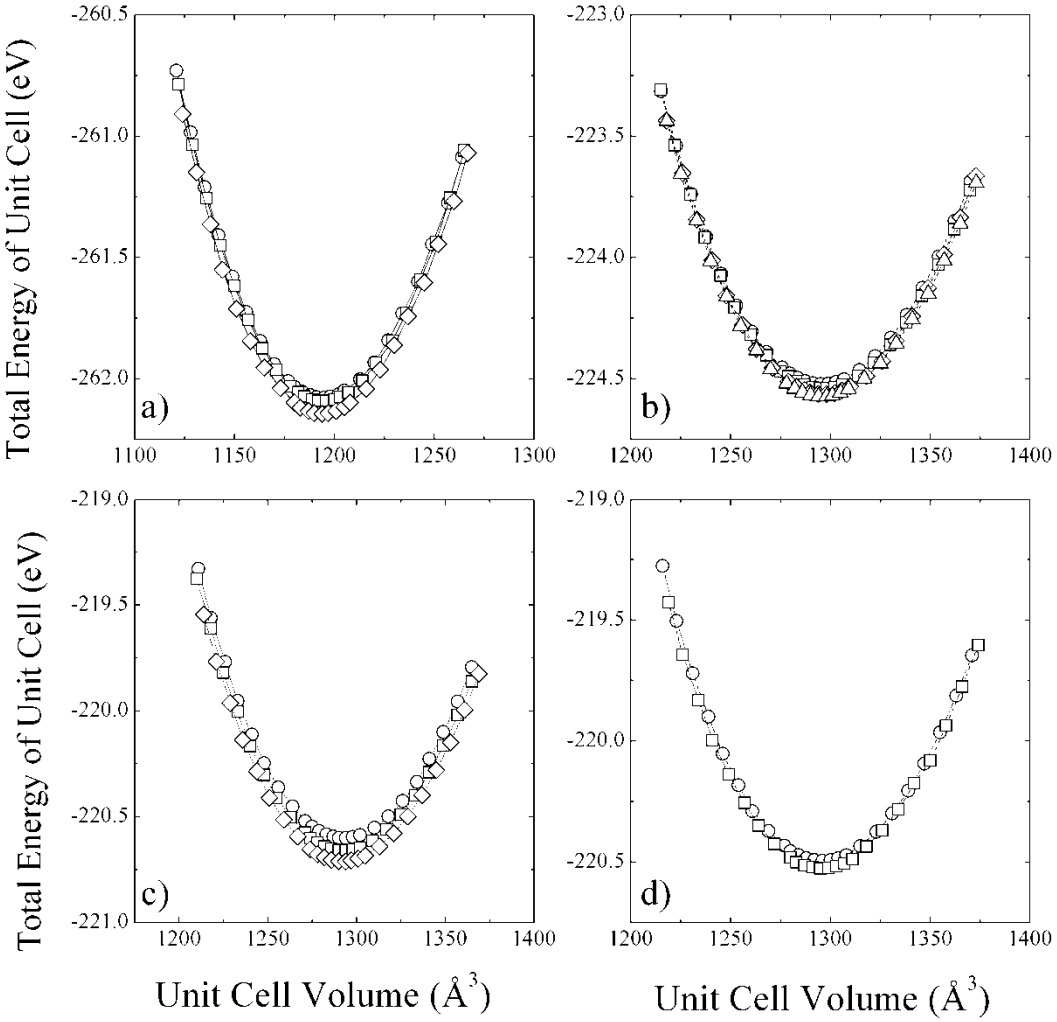

Figure 4.2 – Total energy as a function of volume for the ZB structure using the (a)LDA|PAW with plane-wave energy cut-offs of 400 (○), 425 (□) and 500 (◊) eV; (b) PBE|PAW at 360 (○), 420 (□) 470 (◊) and 500 (Δ) eV, (c) PW91|PAW at 360 (○) 425 (□) and 500 (◊) eV and (d) PW91|USPP at 300 (○) and 500 (□) eV.

Alternatively, the larger than experimental lattice constant values produced by the GGA functionals are accompanied by smaller bulk modulus values. The bulk modulus values for the GGA functionals range from 68.55 to 69.93 GPa, which is ~ 10% smaller than the average of the experimental values. The PBE|PAW performed least accurately, followed by the PW91|USPP, with the PW91|PAW gaining the highest degree of accuracy by a minor degree. No significant increase in accuracy was produced with the use of larger basis set sizes.

The results for the pressure derivative of the bulk modulus calculations vary from 3.954 – 5.481, but this is to be expected based of the functional form of Eq 3.20. As the experimental values are also spread over a moderate range of 4 – 4.91, the majority of values for $B_o^{'}$ calculated here lie within the range of the experimentally reported figures and are consistent with other theoretical values. Therefore no clear benefit could be found through the use of any particular DFT method.

Figure 4.3 shows the parabolic fits of total energy *vs.* elastic strain δ, which were used to calculate the C_{11} elastic constants. The only experimental study to found to include this constant reported a value of 104.6 GPA. The LDA|PAW approach produced values of ~ 117 GPa, which is ~ 12.5% higher than the experimental value. Marginally better agreement with experiment occurred with increasing basis set size. The GGA approximations overall produced results in very good agreement with experiment, in the range of 92.680 – 98.627 GPa with most lying in the 96 – 98 GPa range. For all the GGA functionals the C_{11} elastic constant decreased in value *away* from the experimental value with increasing basis set size. Results for these calculations were consistent with other theoretical values reported.

The C_{12} elastic constant calculations displayed a similar trend to the C_{11}, with the LDA|PAW producing values in the range of 70.526 – 71.223 GPa, which was higher than the reported experimental value of 65.3 GPa but in good agreement with two of the three previous theoretical values; while the GGA methods produced lower than experimental values in the range of 55.048 – 56.860 GPa, with the PBE|PAW providing the least accurate and PW91|USPP the most accurate results but only marginally. No increase in accuracy was found with increasing basis-set size.

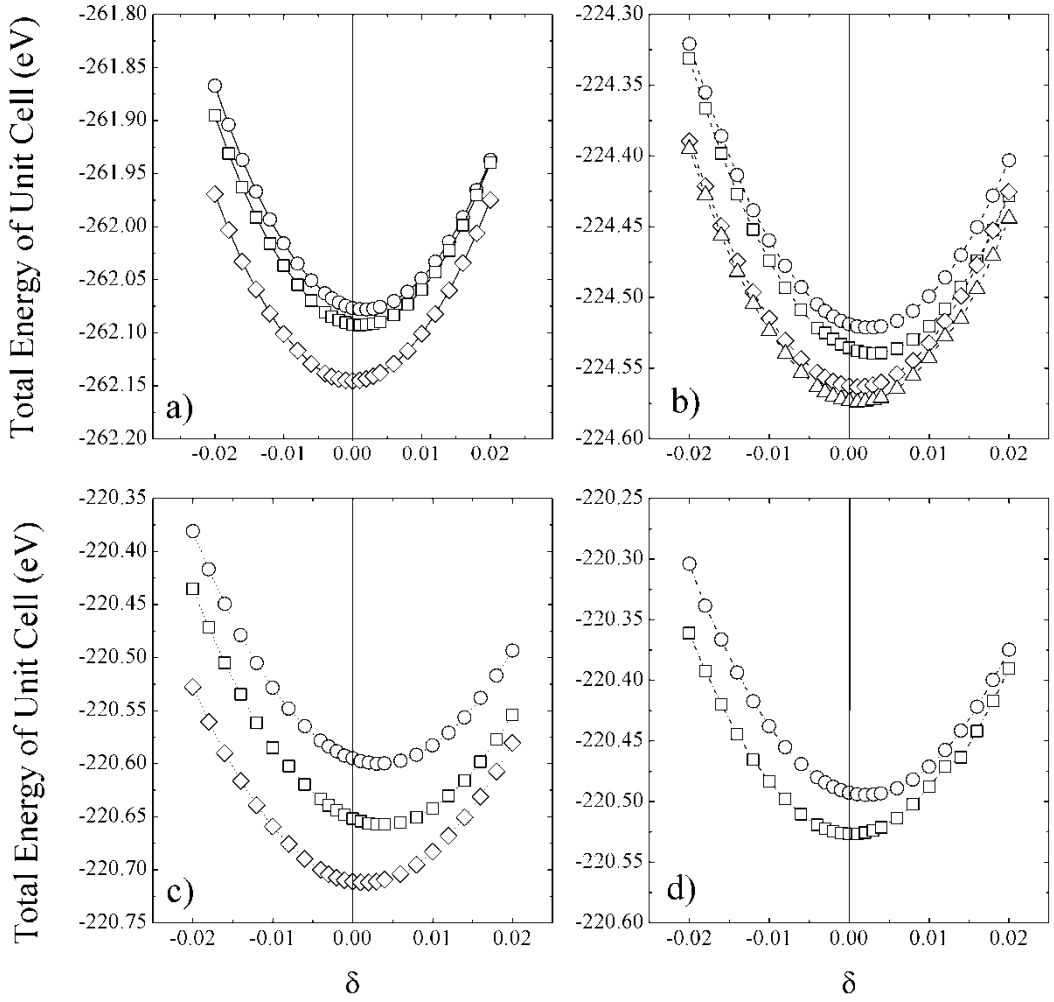

Figure 4.3 - Total cell energy as a function of elastic strain δ, used in determining the C_{11} elastic constant for the ZB structure, calculated using (a) LDA|CA|PAW with plane-wave cut-offs of 400 (O), 425 (□) and 500 (◊) eV; (b) GGA|PBE|PAWat 360 (O), 420 (□) 470 (◊) and 500 (Δ) eV; (c) GGA|PW91|PAWat 360 (O) 425 (□) and 500 (◊) eV and (d) the GGA|PW91|USPP at 300 (O) and 500 (□) eV.

For each DFT approach the enthalpy of formation for the ZB phase, calculated using the S_2 molecule to estimate the chemical potential of sulphur (μ_S), was significantly lower than the experimental value of -206.53 kJ/mol. The LDA|PAW approach came in closest with a value which was ~ 15% higher than experiment, while the PBE|PAW approach performed least effectively coming in at ~ 24% higher. In contrast, calculations of the same constant were significantly higher than experiment when using the S_8 molecule as the basis for μ_S, with the least accurate being the LDA|PAW approach producing a constant ~ 34%

higher and the most accurate the PBE|PAW which was ~ 17% higher. It should be noted that the DFT calculations are performed at zero temperature and pressure and the experimental value is determined at standard temperature and pressure (298 K, 1 atm). No studies were found to report on earlier theoretical calculations of this constant.

In the results for the LDA|PAW approach, the smaller lattice constant and larger bulk modulus in comparison to experimental values is consistent with other LDA calculations. This suggests that for ZnS the bond strength produced using the LDA is too high; while the GGA approximation appears to produce a an effective bond strength that is too low. It has been suggested previously that LDA calculations reproduce mechanical properties more accurately than GGA[165]; however these results indicate that this is *not* the case for ZB phase ZnS.

4.3.2 WZ structure

The total energy of the WZ phase was found to converge at plane-wave energy cut-off of 500eV for all methods, as can be seen in Figure 4.4. Between 325 – 500 eV the total energy using LDA|PAW and PW91|PAW decreases at the rate of -4 meV/eV. In these cases convergence is achieved with a spread in total energy of < 4 meV above a cut-off of 500 eV. The total energy of the PBE|PAW fluctuates at lower energy cut-offs with a spread of 27 meV occurring from 325 – 600 eV. This reduces to 4.4 meV beyond a cut-off of 500 eV. The GGA|PW91|USPP approach produces a spread of 35 meV for cut-offs in the range of 325 – 500 eV and 15 meV between 400 – 500 eV.

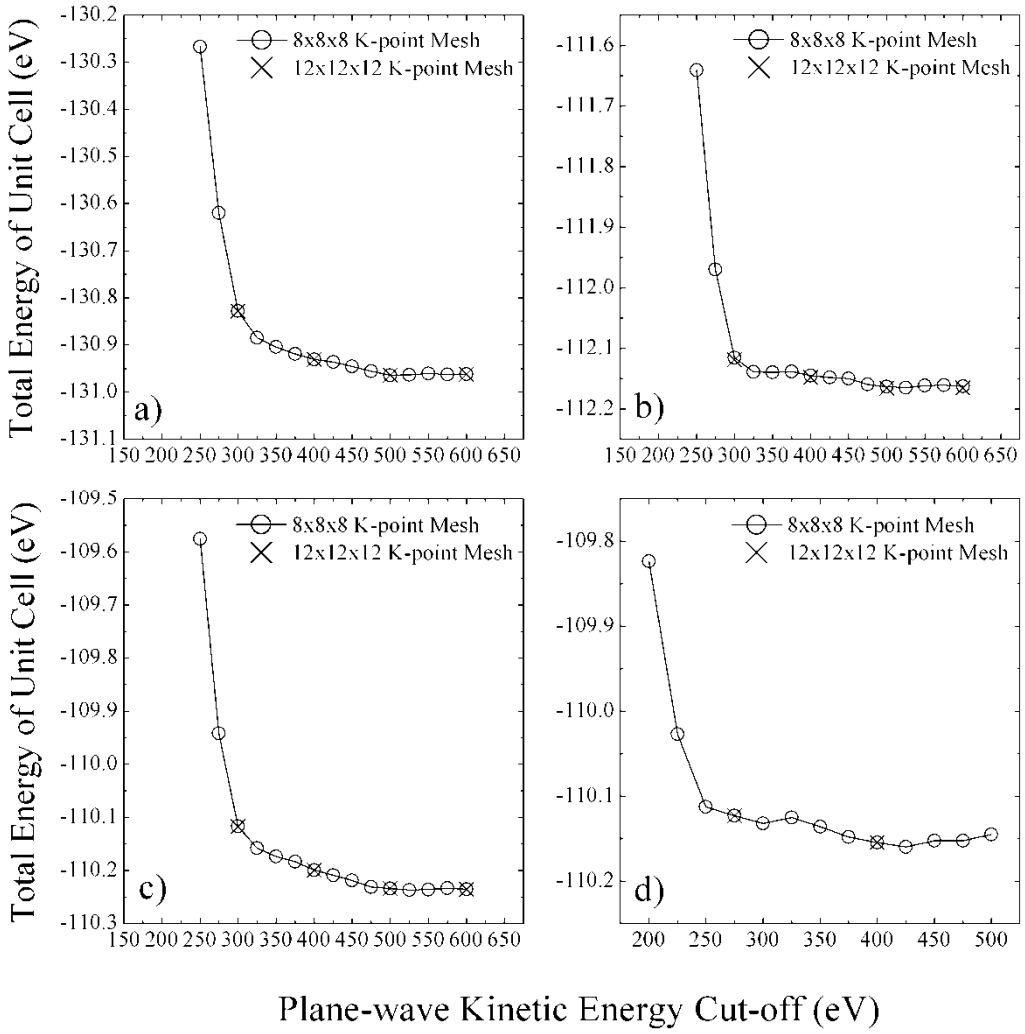

Figure 4.4 – Total energy as a function of plane-wave energy cut-off for the WZ structure, using a) LDA|PAW, b) PBE|PAW, c) PAW|PW91 and d) PW91|USPP with 8x8x8(O) and 12x12x12(X) *k*-point mesh sampling. Data points are offset for display purposes, and lines are for visual guidance only. First and last data points in each set are labelled with the calculated total energy value.

Convergence with respect to *k*-points for the WZ phase was achieved with an 8x8x8 mesh. As with the ZB phase, the change in energy after increasing the *k*-point mesh from 8x8x8 to 12x12x12 *k*-points was less than 10^{-2} eV (Figure 4.4).

Table 4.3 shows the results of bulk constant calculations for the WZ phase, which showed similar outcomes to the ZB phase. In comparison to experiment, the lattice constants for the WZ phase were more accurate using GGA than LDA. The average WZ lattice

constants calculated using LDA|PAW were 3.743 and 6.145 Å for the *a* and *c* lattice parameters, respectively. This is less than the experimentally determined values of 3.816 and 6.252 Å. Results were very consistent for methods used within the GGA. The minimum and maximum values for these approaches were 3.846 and 3.851 Å and 6.301 and 6.318 Å for the *a* and *c* lattice parameters, respectively. These values were less than ~ 0.9% of the experimental values for *a* and *c*. As for the ZB phase, the cell parameters calculated under the LDA were smaller than experiment; while those under the GGA were larger. The GGA methods were significantly more accurate than LDA, however.

The results of total lattice energy calculations for the WZ phase with respect to minor variations in the cell volume are shown in Figure 4.5. At each volume the *a* and *c* lattice parameters were allowed to relax independently, in order to achieve zero stress, subject to the constraint that the total volume remained constant. Using data from Figure 4.5 the bulk modulus and pressure derivative of the bulk modulus were calculated for each DFT method according to Eq 3.20. The results of total lattice energy calculations with respect to distortions of the *a* and *c* lattice parameters are shown in Figures 4.6 and 4.7, respectively. In these figures there can be seen minor variations in the in the minimum energy point with different plane-wave energy cut offs. This is to be expected as variations in basis set size can produce minor fluctuations in calculations beyond the point of total energy convergence. This data was used to calculate the symmetry preserving elastic constants $C_{11}+C_{12}$ and C_{33} according to Eqs 3.23 and 3.24. These results are reported in Table 4.3.

Table 4.3 – Summary of bulk constant calculations for the Wurtzite (WZ) structure. The total memory required (Mem Req) refers to a single static point energy calculation of the fully relaxed structure (in gigabytes).

Method	a (Å)	c (Å)	B_o (GPa)	B_o'	$C_{11}+C_{12}$ (GPa)	C_{33} (GPa)	E/N_{fu} (eV)	ΔH_f (S_8) (kj/mol)	ΔH_f (S_2) (kj/mol)	Mem Req (GB)
LDA|CA|PAW|325	3.741	6.140	85.635	4.397	204.544	164.969	-4.09	-174.90	-275.46	13.358
LDA|CA|PAW|500	3.745	6.150	86.158	3.928	202.467	165.215	-4.09	-175.96	-275.51	23.021
GGA|PBE|PAW|325	3.850	6.307	68.704	4.384	166.204	134.498	-3.505	-157.25	-241.08	13.349
GGA|PBE|PAW|500	3.851	6.311	68.483	4.181	173.452	132.909	-3.506	-157.33	-241.28	22.976
GGA|PW91|PAW|325	3.846	6.301	69.645	4.348	168.541	136.541	-3.446	-162.88	-246.62	12.186
GGA|PW91|PAW|500	3.848	6.305	69.567	4.411	169.145	135.705	-3.443	-163.07	-247.24	18.028
GGA|PW91|USpp|275	3.848	6.309	69.780	4.371	168.079	137.418	-3.442	-163.49	-244.02	12.114
GGA|PW91|USpp|500	3.850	6.318	69.219	4.485	164.396	133.631	-3.443	-163.31	-246.84	23.449
Other theoretical	3.982[a] 3.811[b]	6.500[a] 6.235[b]	66.093[b]		170[a] 169.2[b]	135[a] 140.0[b]				
Experimental	3.816[c]	6.252[c]	80.1[c] 76.746[d]	4[c]	184.35[d]	140.0[d]				

[a] LCAO[50]; [b] Classical MD[164]; [c] Expt.[163] ; [d] Expt.[166]

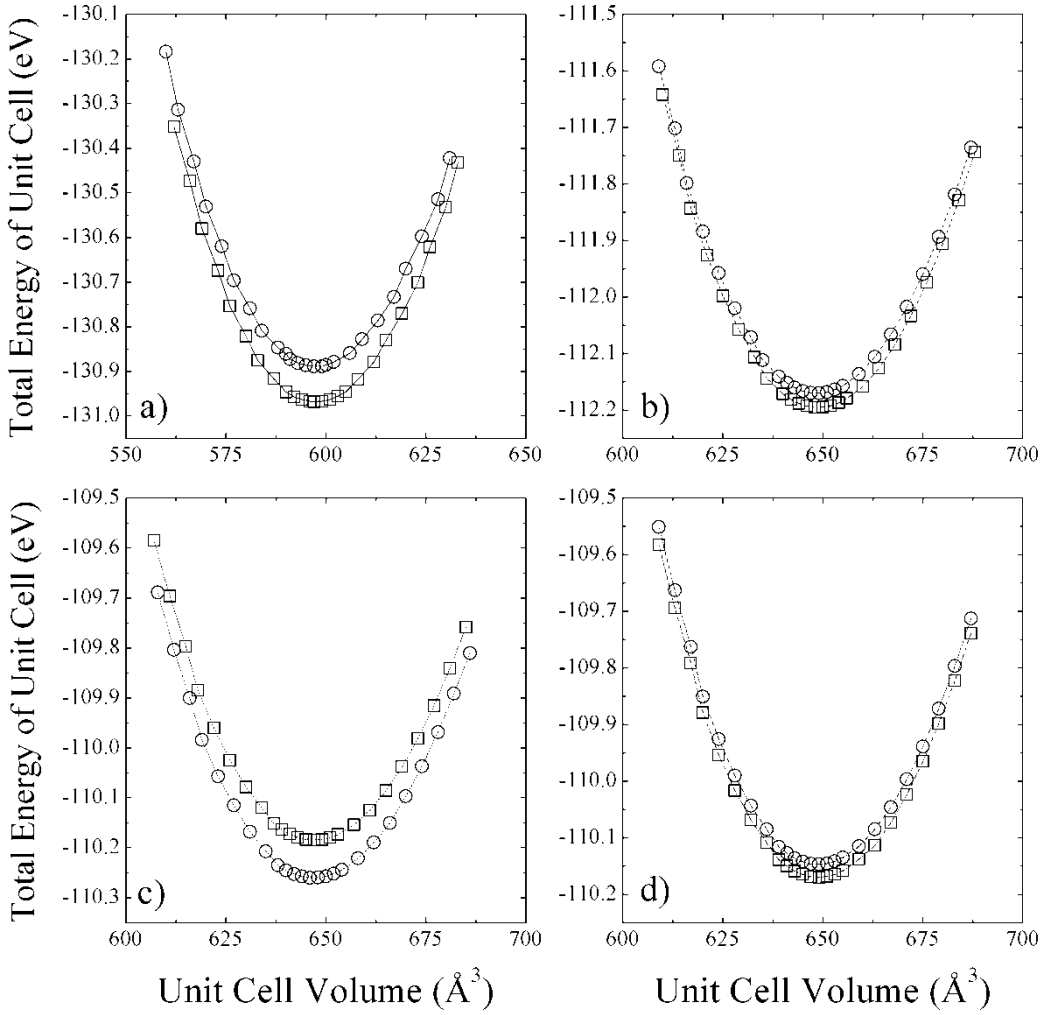

Figure 4.5 – Total energy as a function of volume for the WZ structure, using a) LDA|PAW with plane-wave energy cut-offs of 325(O), 500(□) eV; b) PBE|PAW at 325(O), 500(□) eV, c) PW91|PAW at 275(O) and 500(□) eV and d) PW91|USPP at 325(O) and 500(□) eV.

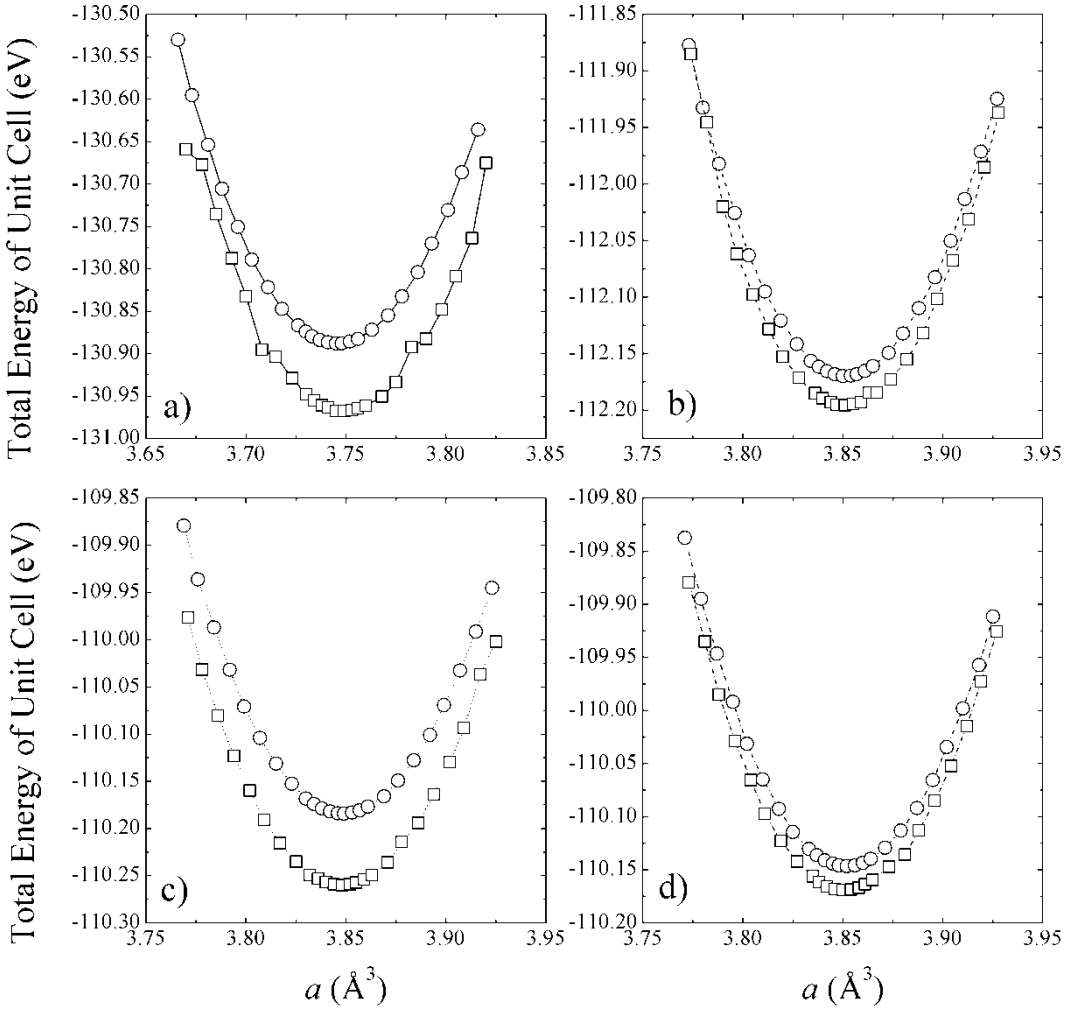

Figure 4.6 – Calculations of total energy as a function of the a lattice parameter, used in determining the sum of the $C_{11} + C_{12}$ elastic constant for the WZ structure, calculated using a) LDA|PAW with plane-wave cut-offs of 325(□) and 500(Δ) eV; b) PBE|PAW at 325(□) and 500(Δ) eV; d) PW91|PAW at 325(□) and 500(Δ) eV and d) PW91|USPP at 275(□) and 500(Δ) eV.

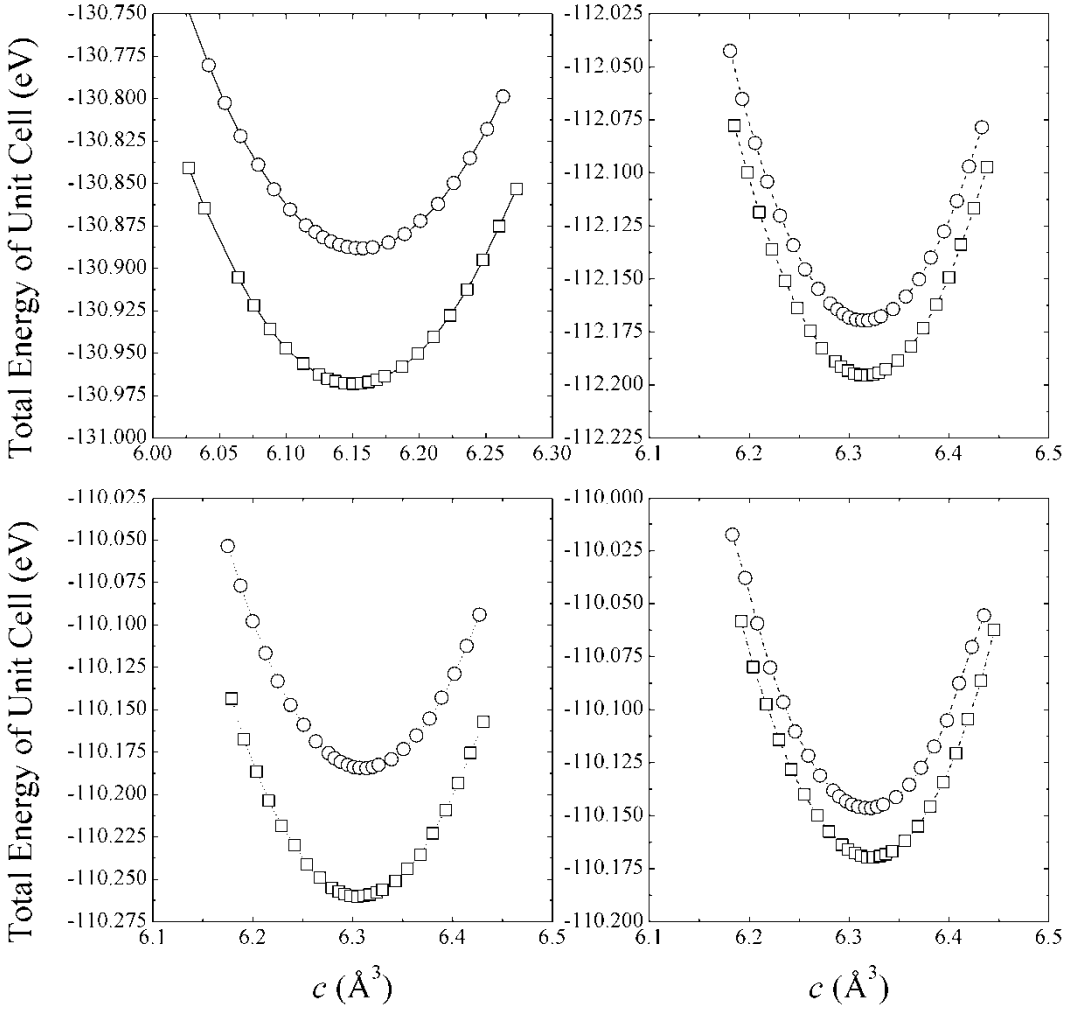

Figure 4.7 – Calculations of total energy as a function of the *c* lattice parameter, used in determining the C_{33} elastic constants for the WZ structure, calculated using a) LDA|PAW with plane-wave cut-offs of 325(O) and 500(□) eV; b) PBE|PAW at 325(O) and 500(□) eV; c) PW91|PAW at 325(O) and 500(□) eV and d) PW91|USPP at 275(O) and 500(□) eV.

The bulk modulus calculated under the LDA was higher than the two experimentally reported values; while under the GGA it was lower. This might be expected considering that the LDA produces a higher Zn-S bond strength. All methods produced values which were ~ ±10% of the average of the two experimental values reported in Table 4.2. The $C_{11} + C_{12}$ and C_{33} elastic constants also probe the Zn-S bond strength so it is not surprising that these elastic constants calculated under the LDA are higher and under the GGA lower than experiment. For these constants slightly greater accuracy is found for the GGA methods over LDA, with no significant change between the GGA methods.

As can be seen in Table 4.3, the calculated enthalpies of formation for the WZ phase using the S_8 and the S_2 molecule are similar to those obtained for the ZB phase, suggesting that the lattice energies are similar for these two phases.

With the continued development of parallel computing and availability of distributed clusters, it is usually accessible memory that limits the size of a DFT calculation rather than number of CPUs. Therefore in Tables 4.2 and 3.3 we also list the memory requirements for our calculations. These results are dependent on a number of factors, such as hardware architecture, number of CPUs and software compilation and operating parameters, so the exact memory requirements may be misleading and only the relatively trends should be considered. The results show that the LDA and GGA require similar memory requirements, and the only important consideration for the case of ZnS is the basis set size. This contrasts with a common assumption that the LDA is typically a less computationally expensive method.

4.4 Conclusions

The results of this study and recommendations for studying ZnS using plane-wave DFT are summarised below. These considerations may also apply to structures of lower dimensionality (for example slabs and rods).

1. For bulk systems an 8x8x8 (Monkhorst-Pack) *k*-point mesh was adequate for sampling over the Brillouin zone. For structures of lower dimensionality, the same mesh density should be used in the periodic directions.
2. A plane-wave cut-off of 500 eV is a safe value for calculating elastic moduli which require calculations of the total energy with volumetric distortions, based on Figures 4.2 and 4.5.

3. For isotropic or symmetry preserving distortions (B_0 or $C_{11}+C_{12}$, C_{33}) an appropriate value for plane-wave cut-off can be lower than 500 eV, based on the results of Table 4.3.
4. GGA provides greater accuracy for calculations of cell parameters over LDA.
5. LDA typically produces a higher Zn-S bond-strength. This leads to smaller cell parameters and larger elastic moduli in comparison to experimental values.
6. Conversely GGA produces a lower Zn-S bond-strength, leading to larger cell parameters and smaller values for elastic moduli.
7. GGA shows remarkable uniformity in its calculations of structural (cell parameters) and mechanical (elastic moduli) properties of ZnS with PBE and PW91 giving very similar results largely independent of pseudopotential (USPP or PAW) or basis set size (over the cut-off range studied).
8. LDA gives larger values for the formation enthalpy over GGA and it is not possible to determine which of these gives results closer to experiment as this is also dependent on the appropriate choice of material for calculating the chemical potentials.
9. In terms of formation enthalpy, the PBE|PAW results are converged for plane-wave cut-offs greater than 420 eV and the PW91 results seem to converge at 500eV independent of the pseudopotential used.
10. In terms of memory requirements for the calculation, the only consideration is plane-wave energy cut-off.

Based on these findings, the PAW|PW91|500 approach was found to be the most suitable DFT approach for studying ZnS, and was used in further studies presented in the following chapters.

Chapter 5. Morphological and Phase Stability in the Zinc Blende and Amorphous Phases

5.1 Introduction

This chapter presents the results of first principle computer simulations (based on the comparative study in Chapter 4) and advanced theoretical modelling (described in Chapter 3) which were used to investigate the relative stabilities of nanoparticle shapes in the ZB phase through a comparison of relative free energies as a function of size. The relative free energies of shapes in the ZB phase were also compared to the free energies of an amorphous (AM) phase nanoparticle in order to determine if a size dependent ZB to AM phase transformation is expected. The work presented in this chapter was published in reference 167.

5.2 Theoretical and Computational Method

At standard temperature and pressure (STP) ZnS is stable in the zinc-blende (ZB or B3) phase, otherwise known as sphalerite. The ZB phase possesses a dual basis, face-centred cubic structure with an internal parameter of (¼, ¼, ¼). Both zinc and sulphur atoms are tetrahedrally coordinated and the ZnS dimers are stacked in an ABCABC arrangement. In the present study the specific surface energies for the {100}, {111}, {110} and {311} surfaces were included as they are often observed experimentally in samples of ZB ZnS nanoparticles[108, 112-114]. The properties of these surfaces have been calculated using density functional theory (DFT) according to the most effective method found in Chapter 4.

5.2.1 Surface structure and energetics

Surface energies were calculated according to Eq 3.13. Explicit dipole corrections for the slab calculations were not included as a full correction is only possible for cubic supercells in VASP. Therefore to minimize the effect of dipoles in the direction perpendicular to the surface plane a large vacuum space was used as the dipole-dipole and monopole-quadrupole

interactions scale as $1/L^3$. In each case a stoichiometric two dimensional slab was generated comprising of 20 atomic layers, surrounded by 20 Å of vacuum space perpendicular to the crystallographic plane of interest (*i*), and the entire structure was fully reconstructed and relaxed prior to the calculation of the energy and stress. The terminal layer of the {110} surface contains both Zn and S atoms (see Figure 5.1a). However, in the case of the {111}, {100} and {311} surfaces (see Figures 5.1b, 5.1c and 5.1d, respectively), one surface is terminated by a layer of Zn atoms, and the other by a layer of S atoms. It is possible to unambiguously define the specific surface energies of these unique surfaces in terms of the chemical potentials of the constituents (μ_{Zn} and μ_S), however when investigating the shape of regular (symmetric) nanocrystals the total surface energy difference does not depend on μ_{Zn} or μ_S, and the sum of the surface energies of polar surfaces is always a constant. This is a consequence of the fact that both surfaces must be present on the nanocrystal to preserve the stoichiometry of the entire nanoparticle. Therefore, in the present study, an "average value" of surface energy was used for the {111}, {100} and {311} and surfaces. A comparison of our results of the surface formation energies γ_i, i = 100, 111, 110 and 311, is provided in Table 5.1, along with some previously reported polar surfaces (that are not directly comparable). The isotropic surface stresses σ_i were computed from the trace of the surface stress tensor, which is output directly by the VASP code. No previous results could be located for comparison with the calculated values of $\sigma_{100} = 0.19$ Jm^{-2}, $\sigma_{111} = -0.49$ Jm^{-2}, $\sigma_{110} = 0.41$ Jm^{-2}, $\sigma_{311} = 0.37$ Jm^{-2}.

Table 5.1 – Comparison of surface energies for ZnS in the ZB structure calculated using different computational methods, in J/m^2.

Method	{110}	{111}	{100}	{311}
Lattice statics simulation, IAP[a]	0.53	1.01 [e] 0.87 [f]	1.12 [e] 1.30 [f]	
DFT, GGA (PW91) [a]	0.46			
MD [b]	0.65	1.82 [e] 1.12 [f]	1.25 [e] 1.31 [f]	
MD [c]	0.39	1.84	2.56	
DFT, GGA (PW91) [d]	0.43	1.36 [g]	2.03 [g]	1.73

[a] Ref [64]; [b] Ref [168]; [c] Ref [54]; [d] This Study; [e] Zn-terminated; [f] S-terminated; [g] Averaged over Zn- and S-terminated

Amorphous ZnS was produced by expanding and heating (using NVT molecular dynamics) a 3x3x3 supercell of crystalline ZB structured ZnS, containing 216 atoms. The volume of the supercell was initially expanded to ~20% above its equilibrium value, then thermally annealed in various stages up to 1500 K, and finally quenched down to 300 K. NVE molecular dynamics was then conducted until the system reached thermal equilibrium. Once thermal equilibrium was obtained the volume of the supercell was uniformly contracted in stages, allowing for full atom relaxation at each stage, to determine the equilibrium volume. A radial distribution function of the system at equilibrium mass density was then calculated and showed a very diffuse second order peak and no definitive structure at long range indicating the system had amorphised.

Figure 5.1 – Schematic representations of the stoichiometric 2-dimensional zinc blende periodic slabs following relaxation using DFT. Each slab is oriented perpendicular to (a) the <220> direction, (b) the <111> direction, (c) the <200> direction, and (d) the <311> direction, and separated by a 2 nm vacuum layer. Also shown is (e) the 2-dimensional amorphous slab.

From the amorphous bulk a vacuum space of approximately 30 Å was created to form an amorphous slab (Figure 5.1e). This slab was then relaxed by successive molecular dynamics/geometry optimisation runs to fully relax the surface layers. Throughout the

amorphisation procedure the initial molecular dynamics calculations were conducted using the lattice program GULP[169]. Subsequent molecular dynamics and all geometry optimisations were conducted using DFT. For the geometry optimisations the same methodology as for crystalline ZnS calculations was used except that the *k*-point sampling was reduced to 2x2x2 or 2x2x1 for the bulk and surface runs respectively. Testing at higher *k*-point sampling resolution showed the total energy was the same as for 2x2x2 to within a few meV.

5.2.2 Thermodynamics and nanomorphology

The shape-dependent thermodynamic model in Eq 3.12 was used to model ZB shapes in this section and predict their relative stabilities. The four crystalline surfaces included in this study are the {110}, {311}, {100} and {111}. These peaks provide an indication of the surfaces found on ZB ZnS nanoparticles; however they do not represent an efficient criterion alone to predict equilibrium crystal morphologies. The equilibrium structure is defined by the relative proportion of these facets, as expressed in Eq 3.12. Atmospheric external pressure is assumed, and a lattice parameter of 5.443 Å and bulk modulus B_0 = 69.9 GPa are used, which have been shown to be in good agreement with the corresponding experimental values (as reported in Chapter 4). The *q* and *f* expressions for ZB shapes are given in Appendix A.

5.3 Results and Discussion

5.3.1 Shape selectivity in the ZB phase

Using these values of γ_i provided in Table 5.1, and σ_i as listed above, energies were modelled for a collection of shapes enclosed by different combinations of these low index surfaces, as shown in Figure 5.2.

In this collection, four morphologies are enclosed entirely by one type of surface,

presenting as the Catalan rhombic dodecahedron (Figure 5.2a), the Platonic octahedron (Figure 5.2b), the Catalan deltoidal icositetrahedron (Figure 5.2c), and the Platonic regular hexahedron (Figure 5.2d, also known as the cube). These shapes are enclosed by {110}, {111}, {311} and {100} facets, respectively.

The free energies for the more complicated shapes (those enclosed by more than one type of surface) were also calculated, and are presented in Figure 5.3, with respect to bulk ZnS. Here it can be seen that, although a small truncation has the effect of lowering the surface-to-volume ratio, the degree of surface energy anisotropy is significant, and a departure from the ideal polyhedra is still thermodynamically unfavourable unless only lower energy facets are introduced. For example, irrespective of the direction of truncation the rhombic dodecahedron remains the lowest energy shape, since (although Figures 5.2(ab), 5.2(ac) and 5.2(ad) have lower surface-to-volume ratios) all other facets are significantly higher in energy than the {110}. However, if we were to begin at the bottom of Figure 5.2, with the regular hexahedron Figure 5.2(d), then the modifications of the shape that introduce additional {111}, {110} and {311} facets (shown in Figures 5.2(db), 5.2(da) and 5.2(dc), respectively) both lower the surface-to-volume ratio and the total surface energy. As a rule of thumb, truncation of the hexahedron is always favourable, and truncation of the other high energy shapes depends sensitively on the relative energy of the different facets and the degree of truncation. This is not to say that higher energy shapes (such as those in Figure 5.2, or other combinations not included in this study) cannot form, merely that these shapes are thermodynamically unfavourable with respect to a morphological transformation to a rhombic dodecahedron. The transformation may or may not be spontaneous depending upon the kinetic barriers present, and the driving force applied.

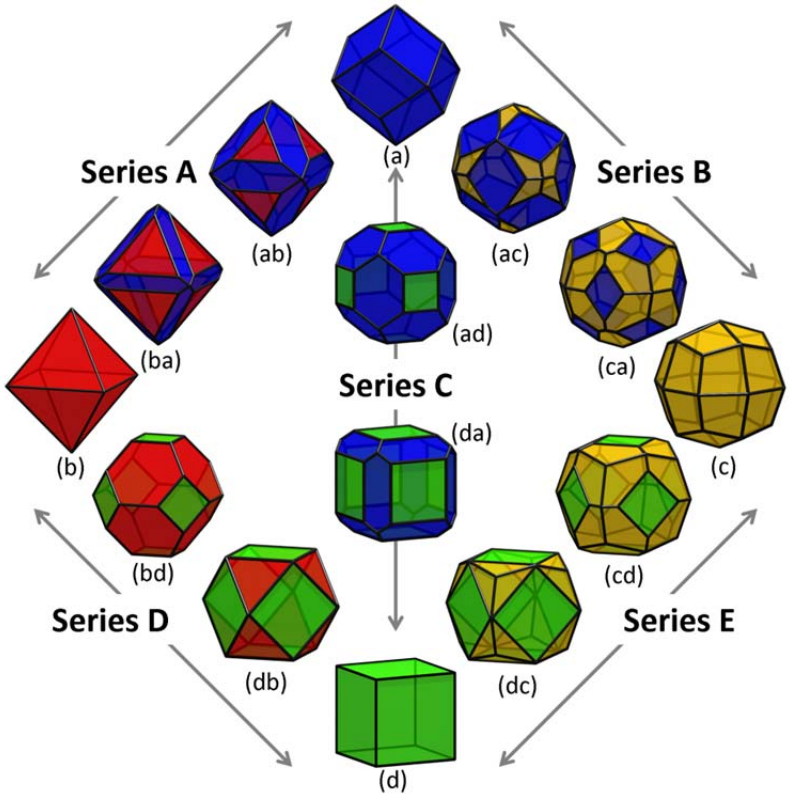

Figure 5.2 – Shapes of zinc blende ZnS nanoparticles explored in this study, with truncation series terminated by (a) the Catalan rhombic dodecahedron, (b) the Platonic regular octahedron, (c) the Catalan deltoidal icositetrahedron, and (d) the Platonic regular hexahedron (or cube). The stationary points in each series are chosen such that the fraction of surface area attributed to the minority and/or majority facets conform to the ratio defined by the Platonic truncated octahedron (bd) and Archimedian cuboctahedron (db). The {220} facets are shown in blue, {111} facets are shown in red, {311} facets are shown in yellow, and {200} facets are shown in green.

These results will have implications for the way ZB ZnS nanoparticles interact with their surroundings (and each other). The {110} facets are non-polar and will interact via weak van der Waals forces (see Figure 5.1a). The {111}, {311} and {100} facets are polar (see Figures 5.1b, 5.1c and 5.1d), and if introduced kinetically, will allow the nanoparticles to interact via stronger electrostatic attraction and repulsion. The former gives rise to loosely bound aggregates or isolated particles given suitable perturbation, whereas the latter are stronger interactions that are often associated with self-assembly or the formation of robust ordered superstructures[170]. This will influence the agglomeration behaviour, and hence the bioavailability of dry samples.

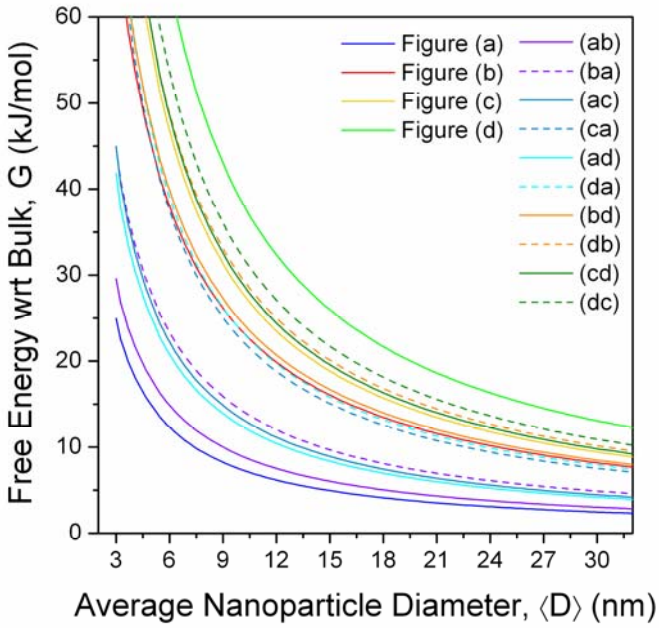

Figure 5.3 – Relative free energy of formation of zinc blende structured zinc sulphide nanoparticles, as a function of size and shape, showing the rhombic dodecahedron (a) is the thermodynamically preferred shape, and the regular hexahedron the least preferred. The shapes are defined in Figure 5.2, and the results are calculated with respect to bulk ZB ZnS.

These results are in good agreement with those reported previously based on lattice statics simulations and DFT[64,65,69], where large ZnS ZB particles were found to prefer rhombic dodecahedral morphologies. At smaller sizes, Spano *et al*.[69] estimated the global energy minimum of small, individual ZnS structures ranging in size from 10 to 47 atoms. Using simulated annealing method and a classical inter-atomic potentials (supported by DFT), these explicit calculations produced 'bubble' clusters (appearing as hollow structures consisting of 4, 6 and 8 atom rings), where all the atoms in the structure are three-fold coordinated, as opposed to the tetrahedral four-fold coordination encountered in "larger" structures (which are still much smaller than those observed experimentally). Similar studies of n = 50 to 80 produced onion-like structures, where one bubble cluster was enclosed inside another with tetrahedral bonding between the two[65,69]. This is similar to the formation of core-shell bucky-diamond structures which is well known in carbon[171,172], and is attributed to delamination of the (111) facets. Again, a change in shape will promote or suppress this instability.

5.3.2 Size-dependent crystallinity

In addition to morphological instability introduced by the presence of high energy facets, or kinetically grown shapes, ZnS may also undergo solid-solid phase transformation under ambient conditions. Zhang, Gilbert, Huang, Banfield and others observed reversible structural transformations in ZnS nanoparticles at room temperature induced by aggregation-disaggregation and absorption-desorption of methanol and water[44]. These studies were supported by classical MD simulations of the interaction between methanol and water and the surface S and Zn ions, which showed that the surfaces of nanoparticles in methanol undergo reconstruction that penetrates several atomic layers, leading to a crystalline core surrounded by a disordered shell. However, water was found to decrease the surface free energy, and promote crystallinity throughout the nanoparticle.

If the change in the interfacial free energy provides a driving force for a change in degree of crystallinity, then it follows that that the size-dependent free energy of the entire nanoparticle (which is dominated by the surface energy term at small sizes) will also play an important role, irrespective of the chemical environment. To investigate this issue, the same theoretical and computational method describe above was used to calculate the properties of amorphous ZnS (see Figure 5.1e), which were then used to calculate the free energy of an amorphous ZnS spherical nanoparticle to compare with low energy ZB structures over 3 nm in size.

The appropriate choices of the bulk free energy of formation, ΔG_f, for both the ZB and amorphous materials, is an important aspect of this analysis. In general, the free energy is the energy difference from reaction that may include a variety of reactants and products. The final value depends upon the temperature and the species participating in the chemical reaction, since some reactions are more favourable than others. For example, experimental

values for the bulk ZB enthalpy of formation are -206.53 kJ/mol as measured by Deore and Navrotsky[131], between -21.87 and -105.45 kJ/mol by Daskalakis and Helz[173], and between -18.84 and -30.26 kJ/mol by Hayashi, Sugaki and Kitakaze[174]. For amorphous ZnS an experimental value for the bulk free energy of formation can vary between -33.52 and -62.87 kJ/mol, as shown by Gubeli and Marie[175]. In order to accurately compare the free energy difference between ZB and amorphous ZnS it is necessary to ensure that the same reaction is considered, but this is problematic since a single reaction rarely produces two different ZnS products. None of these values originate from identical reactions. Therefore, these value were calculated by subtracting the energy per ion of Zn in the hexagonal phase and S in the S_8 dimer from the average Zn-S bond energy determined from our ZB and amorphous supercells, so that they are both calculated using the same computational method (as described above) and reaction, $(ZnS)_8 = (Zn)_8 + S_8$. This gave a value of -166.28 kJ/mol for bulk ZB ZnS and -116.47 kJ/mol for bulk amorphous ZnS, with a free energy difference of 49.78 kJ/mol.

Using the surface free energy and isotropic surface stress of amorphous ZnS, the free energy for spherical nanoparticles was determined using Eq 3.12, and is compared to the results for the four lowest energy shapes for ZB nanoparticles (which now include the bulk free energy of formation). These results are provided as a function of molar surface area in Figure 5.4, and show that the ZB phase is expected to be stable relative to the AM phase at all sizes. The introduction of higher energy, polar facets is not expected to affect the stability of ZB nanoparticles with respect to a phase transformation to the AM phase.

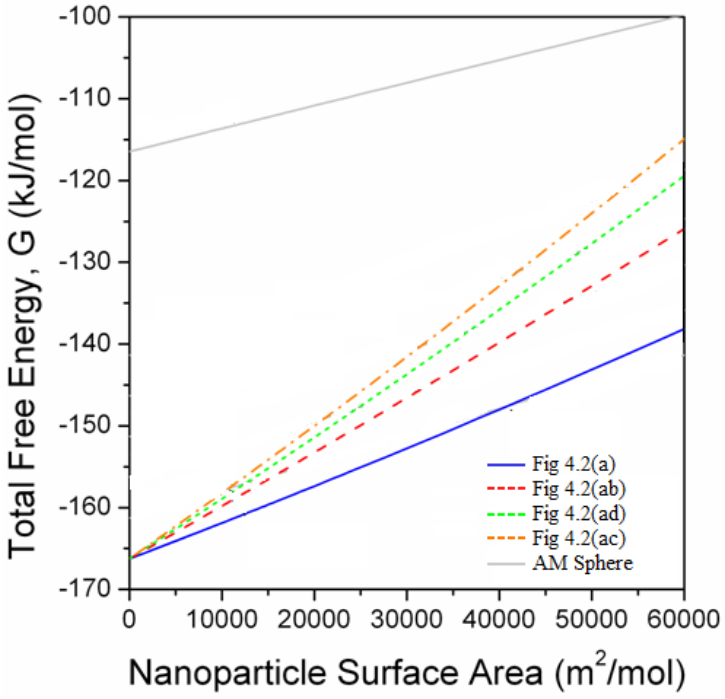

Figure 5.4 – Relative free energy of formation of low energy shapes of zinc blende structured zinc sulphide nanoparticles (as defined in Figure 5.2), as a function of surface area, compared to the free energy of formation of an amorphous ZnS sphere. The absence of a cross-over between the AM and ZB structures indicates that the ZB phase is expected to be stable at all sizes relative to the AM phase.

5.4 Conclusions

In this study, first principles calculations and shape dependent thermodynamic modelling were used to predict the equilibrium shapes of ZnS nanoparticles in the ZB phase as a function of size. The results show a preference for the rhombic dodecahedron morphology at all sizes, which is enclosed by {110} facets. Of the four facets types observed in ZB ZnS nanoparticles, the {110} is the only non-polar. Therefore the equilibrium morphology in the ZB phase will effect the agglomeration behaviour of this material. As polar surfaces are required for many applications, the introduction of such surfaces and the effect this might have on the stability of the material should be taken into consideration; however the introduction of polar surfaces is not expected to affect the stability of ZB phase nanoparticles with respect to the amorphous phase i.e. a ZB/AM phase transformation is not expected at any size for if ZB nanoparticles consisting of {110} surfaces (entirely or pre-dominantly) are produced.

Chapter 6. Size- and Shape-Dependent Phase Transformations in Wurtzite ZnS Nanostructures

6.1 Introduction

Concerning hexagonal phase ZnS nanoparticles, the aspect ratio is often the most critical factor for tuning the material properties[176,177]. This typically comes as a result of differences in surface polarity or atomic density between alternate facets. Tuning the aspect ratio and controlling the fraction of surface area for specific facets is heavily reported in literature[176,178,179]. With respect to these experimental processes and the applications of WZ nanoparticles and nanorods, it is important to know how the aspect ratio of WZ nanoparticles affects stability, as well as the thermodynamic preference for other aspects of the WZ shape. This chapter contains the result of thermodynamic modelling of the WZ phase of ZnS nanoparticles as a function of particle size. In addition, phase transformation sizes between the WZ and ZB phases are revealed by comparing the results of WZ modelling with results from Chapter 5. The work presented in this chapter was published in reference 180.

6.2 Theoretical and Computational Method

The shape-dependent thermodynamic model in Eq 2.12 was used to model WZ shapes in this section and predict their relative stabilities. This modelling included the {0002}, $\{10\bar{1}0\}$, $\{11\bar{2}0\}$, $\{10\bar{1}1\}$, $\{10\bar{1}2\}$ and $\{10\bar{1}3\}$ surfaces, based on the results of experimental XRD studies (JCPDS card: 36-1450). The expressions for q and f for the corresponding WZ shapes are given in Appendix B. The most effective DFT approach for ZnS, as reported in Chapter 4, was used to calculate these surfaces, which were constructed in VASP using 2x2x2 conventional supercells. Energy convergence with respect to vacuum space and slab thickness was achieved at 20 Å and 20 atomic layers. Surface energies and stresses are reported in Tables 5.1 and 5.2.

6.2.1 Shape parameters for defining WZ morphologies

With reference to Figure 6.1, WZ shapes can be defined using four parameters (irrespective of size): (i) the prism aspect ratio x (not to be confused with the *total aspect ratio* referred to in other works, which includes the pyramidal "caps"), where $0 < x$ for prisms capped with {0002} basal planes and $0 \leq x$ for shapes with pyramidal "caps"; (ii) the degree of $\{10\bar{1}0\}$ prism truncation in the $<11\bar{2}0>$ direction x', where $0 \leq x' \leq 1$; (iii) the degree of truncation of the pyramidal caps x'' in the <0001> directions, where $0 \leq x'' \leq 1$; and (iv) the basal plane or pyramidal cap orientation. Note that $x' = 0$ and 1 correspond to prism walls formed entirely of $\{10\bar{1}0\}$ or $\{11\bar{2}0\}$ planes, respectively (as seen in Figures 6.4 (a) and (f)). Maximum truncation of the pyramidal cap ($x'' = 1$) is defined to be the point where the $(0002)/(000\bar{2})$ and $(10\bar{1}0)$ or $(11\bar{2}0)$ planes intersect. This definition slightly reduces the generality but significantly reduces the geometric complexity of the model (see Appendix B).

6.2.2 Nomenclature

Owing to the multiple orientations considered, a naming convention is hereby introduced for convenience of reporting, based on the geometric parameters described above. Shapes are referred to using the following convention: $[x,x',x'']_l$; where x, x' and x'' refer to the prism aspect ratio, degree of truncation of the $\{10\bar{1}0\}$ planes in the $<11\bar{2}0>$ direction, and pyramidal cap truncation, respectively, as indicated in Figure 6.1. For pyramidal caps $\{10\bar{1}1\}$, $\{10\bar{1}2\}$ and $\{10\bar{1}3\}$, the value of l is 1, 2 and 3, respectively, in reference to the l index in the standard $\{hjkl\}$ notation. In the case of flat {0002} basal planes with no pyramidal capping, l will have a value of 0. For example, $[2.0, 0.50, 0.2]_3$ indicates a prism with an aspect ratio of 2.0, $\{10\bar{1}0\}$ and $\{11\bar{2}0\}$ planes in comparable proportions making up the prism walls, and $\{10\bar{1}3\}$ planes forming the pyramidal cap which is truncated to 20% of the maximum degree (as defined above). Note that in the case of $l = 0$, x'' exists as a redundant variable and will be omitted.

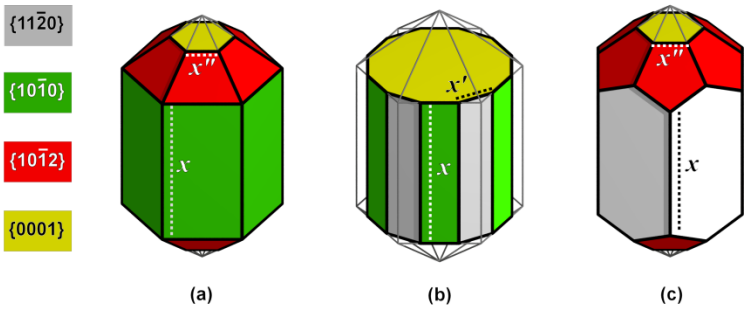

Figure 6.1 – A complete set of wurtzite shapes can be defined using four geometric parameters: *x, x',x''* and *l*. These parameters are illustrated above, using three examples of WZ shapes. These shapes are described using the $[x,x',x'']_l$ convention as (a) $[2.0,0.0,0.2]_2$, (b)$[2.0,0.5,-]_0$ and (c)$[2.0,1.0,0.2]_2$.

6.2.3 Sampling the WZ morphology space

The Gibbs free energy expression in Eq 2.12 and the surface energies and stresses from Tables 5.2 and 5.3 were used to model successive sets of shapes spanning the WZ morphology phase space. The shape sets, their succession and the method of assessing the energy landscape in each region, were designed to thoroughly survey the large, multi-parameter WZ morphology phase space in an intuitive manner. Firstly, the *x* parameter space was sampled at opposite extremes of *x'* (0 and 1) within the limited region occupied by *l*=0 (using the method described in the next paragraph). This was followed by a survey of *x'* space within the limits of *l*=0 and in the region of the optimum value of *x* found previously. These steps were repeated for *l* = 1, 2 and 3, with additional sampling of *x''* space carried out last in the region of optimum values for of *x* and *x'*.

Within each region described above, the <*x*,*x'*,*x''*> parameter space was probed by discretely varying the relevant parameter and comparing the resulting free energies as a function of size. The shape parameter was then effectively varied continuously in an attempt to find the single, optimum value which minimised $\int G\partial D$. Optimisation was performed using a conjugate gradient routine with respect to particle size to find a minimum energy shape at each stage. Once the optimum value for more than one shape variable was found, the

optimisation procedure was repeated for the relevant variables self-consistently. This was performed for l=0 to 3 (except for x'' when l=0, which is a redundant variable). The results reported on in this chapter consist of sets of free energy plots as a function of size and a low energy shape self-consistently optimised in x, x' and x'' for each value of l. In addition, an investigation of the free energy as a function of size and prism aspect ratio was conducted, with the results shown in the form of a free energy surface in the domain of x and D.

6.2.4 Comparison with results of ZB modelling

Using the results of WZ modelling and the results of ZB modelling in Chapter 5, a set of low energy shapes from each phase was selected and their free energies compared as a function of surface area per mole. This revealed the presence of energetic crossovers, corresponding to phase transformation sizes, which varied with shape. The exact nature of these size- and shape-dependent phase transformations are reported in the results of this chapter.

6.3 Results and Discussion

6.3.1 Surface calculations

The results of surface energy and stress calculations are shown in Tables 1 and 2. Surface energy calculations reported in earlier studies are provided for comparison (where they are available). The present results are in good agreement with existing reports. For the purpose of comparison, an extensive search of the literature did not find any existing studies reporting WZ surface stresses.

6.3.2 Influence of prism aspect ratio (x) with {0002} basal planes

The primary geometric feature used to define the shape and anisotropy of nanoparticles is the aspect ratio; whether it is a nanoplatelet or a nanorod. Commencing in the manner described

Table 6.1 – The surface free energies of WZ ZnS in J/m^2, calculated using different computational methods.

Method	{0002}	{10$\bar{1}$0}	{11$\bar{2}$0}	{10$\bar{1}$1}	{10$\bar{1}$2}	{10$\bar{1}$3}
PW91|PAW (present)	1.394	0.431	0.427	1.557	1.201	0.767
MD[a]	1.52	1.00	0.28			
MD[b]	0.9	0.52	0.49			
DFT, GGA (PW91)[c]		0.367	0.385			
DFT, LDA-CAPZ[c]		0.51	0.50			
Broken-bond[c]		0.66	0.67			

[a] Ref [54], [b] Ref [64], [c] Ref [181]

Table 6.2 – The surface stresses of WZ ZnS in J/m2, calculated using the PW91|PAW approach as described in Chapter 5.

Method	{0002}	{10$\bar{1}$0}	{11$\bar{2}$0}	{10$\bar{1}$1}	{10$\bar{1}$2}	{10$\bar{1}$3}
PW91|PAW	0.198	-0.238	-0.406	-0.357	-0.105	-0.084

in Section 6.2.3, the $[x,0.0,-]_0$ shapes were modelled for x = 0.5, 1, 3, 5 and 10 (Figure 6.2), with the results show in Figure 6.3. The prism aspect ratio of x = 0.5 (Figure 6.2a) was the highest energy shape, followed by a prism aspect ratio of x = 1 (Figure 6.2b). Shapes with prism aspect ratios of x = 3, 5 and 10 (Figure 6.2c to e) were in relative thermodynamic co-existence and were the lowest energy shapes modelled in this set. Following this, the $[x,1.0,-]_0$ shape was modelling for the same values of x above. The results, shown in Figure 6.3b, revealed a similar trend to the $[x,0.0,-]_0$ shape, with the prism aspect ratio of 0.5 being highest in energy and prism aspect ratios of 3, 5 and 10 forming a low energy group. The optimum prism aspect ratio was 5.5 for the $[x,0.0,-]_0$ shape and 4.8 for the $[x,1.0,-]_0$ shape; indicating that nanorods may be thermodynamically preferred over quasi-spherical nanoparticles.

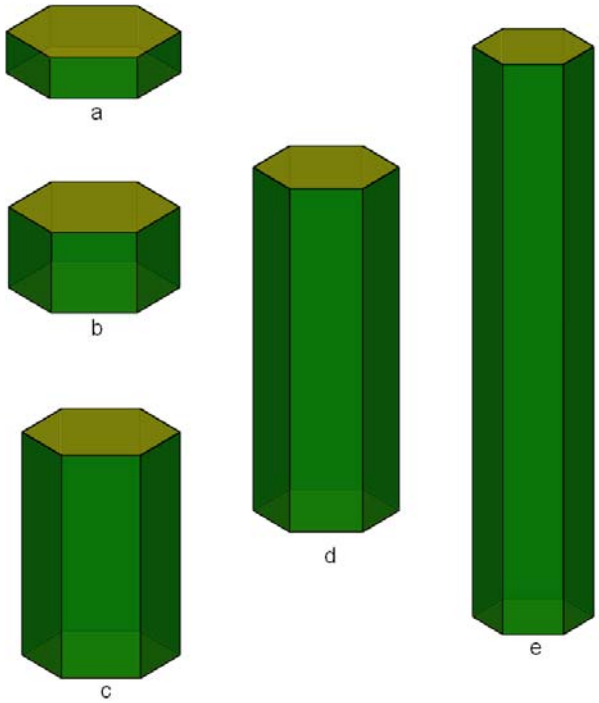

Figure 6.2 – Hexagonal prisms of [x,0.0,–]0 type shapes, composed of {10$\bar{1}$0} (green) and {0002}/{000$\bar{2}$} (yellow) planes, with aspect ratios of x = (a) 0.5, (b)1.0, (c)3.0, (d)5.0, and (e)10.

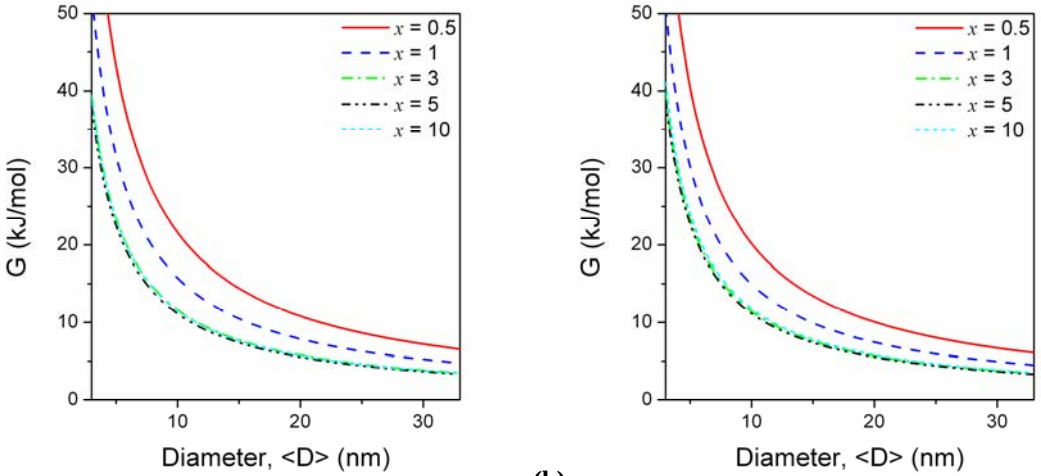

(a) **(b)**

Figure 6.3 – Free energy (G) as a function of average nanoparticle diameter, <D> in nm for (a) the [x,0.0,–]$_0$ shape and (b) the [x,1.0,–]$_0$ shape with prism aspect ratios ranging from $0.5 \leq x \leq 10$.

6.3.3 Influence of prism orientation (x') with {0002} basal planes

Irrespective of the aspect ratio, the prism facets perpendicular to the <0002> direction may present in a number of different orientations. The most commonly observed are the low index $\{10\bar{1}0\}$ and $\{11\bar{2}0\}$ orientations, which both present as (albeit alternate) hexagonal prisms. A combination of both facet types along the length of the prism will produce a dodecagonal prism, which may be irregular depending upon the relative fraction of $\{10\bar{1}0\}$ and $\{11\bar{2}0\}$. Using the optimum aspect ratios (x) identified above as a guide, the $[5.2,x',-]_0$ shapes with x'=0.0, 0.2, 0.4, 0.6, 0.8 and 1.0 (Figure 6.4) were modelled. These different prisms were found to be in relative thermodynamic coexistence but the mathematically optimum value for x' was 0.51, which represents an almost perfect dodecagonal prism.

While not shown graphically, it was noted that as x approached 0.0 (a platelet) the optimum value of x' approached 1.0 (entirely $\{11\bar{2}0\}$) and as x increased above ~10, the optimum value of x' approached ~0.4 (slightly more $\{10\bar{1}0\}$ than $\{11\bar{2}0\}$). However, as stated above, these shapes are in relative thermodynamic coexistence and therefore shape selection is likely to be governed by kinetic factors alone. Self-consistent (simultaneous) optimization of x and x' yielded values of 5.5 and 0.51 for the $[x,x',-]_0$ shape, respectively, corresponding to a shape which would exist between Figure 6.4 (c) and (d).

6.3.4 Influence of x with pyramidal caps

While the introduction of pyramidal facets at the end of the nanorods eliminates the abrupt 90° angle between the prism facets and the {0002} basal planes, it does introduce an apex that is likely to be truncated (or rounded) in real specimens.

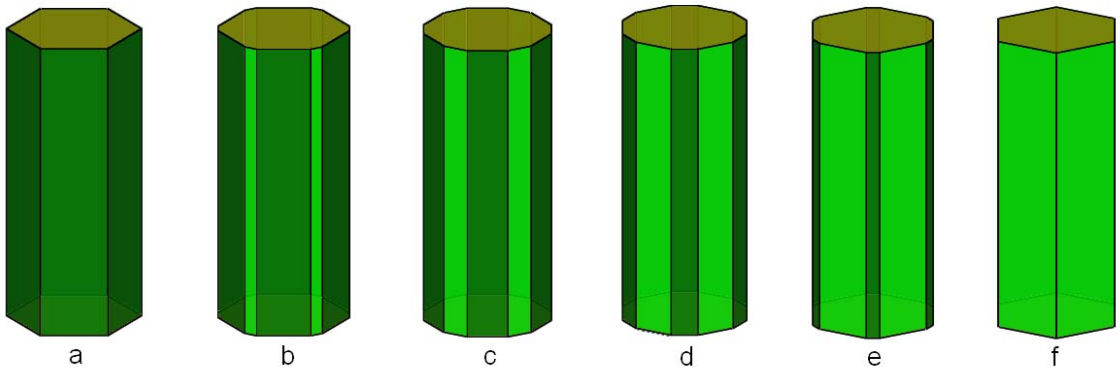

Figure 6.4 – Isovolumetric $[5.2,x',-]_0$ shapes for x' = (a)0, (b)0.2, (c)0.4, (d)0.6, (e)0.8 and f)1.0. Planes are coloured $\{10\bar{1}0\}$ dark green, $\{11\bar{2}0\}$ light green and $\{0002\}$ yellow.

Using the optimum value x' in the $[x,x',-]_0$ shape as a guide, the $[x,0.51,0.0]_l$ shapes were modelled for l=1 – 3 (hexagonal prisms with pyramidal caps of $\{10\bar{1}1\}$, $\{10\bar{1}2\}$ and $\{10\bar{1}3\}$ orientations) and x=0.0, 0.5, 1, 3, 5 and 10 (Figure 6.5). As can be seen in Figure 6.6, the energetically preferred prism aspect ratios are: ~5-10 for l=1; ~3-10 for l=2; and ~1-3 for l=1. The optimum prism aspect ratio, at x'=0.51, was 10.2 for l=1, 5.0 for l=2 and 2.5 for l=3.

6.3.5 Influence of x' with pyramidal caps

Using the optimum values of x (above) the $[x_{opt},x',0.0]_l$ shapes were modelled for x' = 0.0, 0.2, 0.4, 0.6, 0.8 and 1. As with the $[x,x',-]_0$ shapes, the resulting energies were in thermodynamic co-existence. The self-consistently optimised values of x and x' in the $[x,x',0.0]_l$ shapes were, respectively: 10 and 0.51 for l=1; 5.0 and 0.51 for l=2; and 2.5 and 0.52 for l=3.

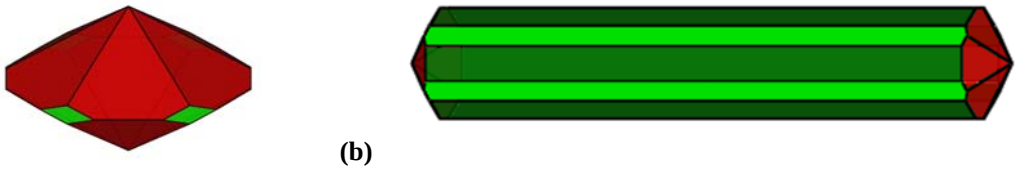

(a) (b)

Figure 6.5 – The $[x,0.51,0.0]_3$ shapes, where x = (a) 0.0 and (b) 10.

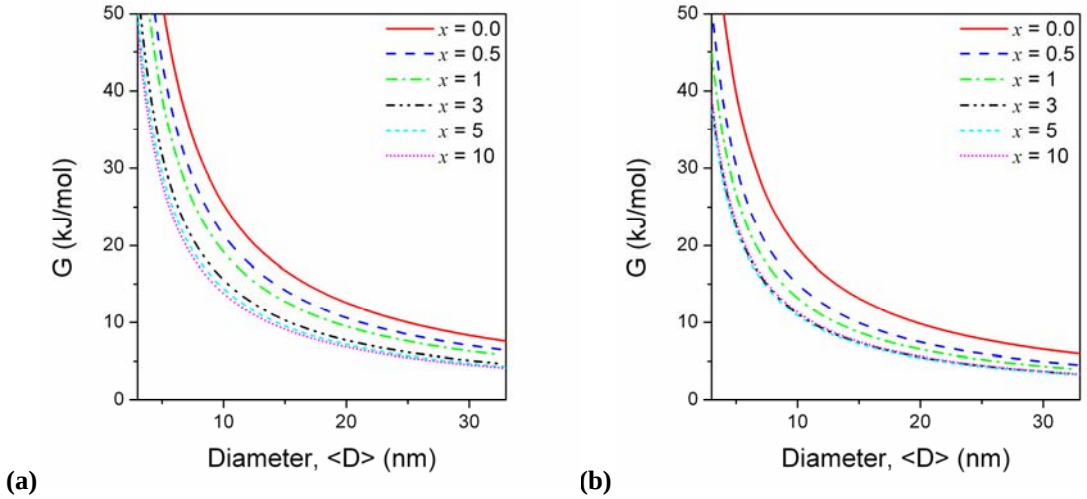

(a) (b)

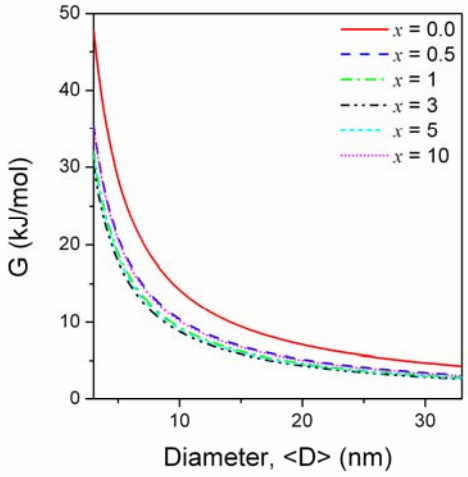

(c)

Figure 6.6 – Free energy as functions of size for the $[x,0.51,0.0]_l$ shapes where l = (a) 1, (b) 2 and (c) 3.

6.3.6 Influence of x'' with pyramidal caps

Using these optimum values of x and x' the $[x_{opt},x'_{opt},x'']_l$ shapes were modelled for x'' = 0.0, 0.2, 0.4, 0.6, 0.8 and 1. Results for the $[10,0.51,x'']_1$ shape, shown in Figure 6.7a, revealed a thermodynamic preference for maximum truncation of the $\{10\bar{1}1\}$ cap in the <0002>

direction (x''=1). Due to the manner in which it is defined however, some {10$\bar{1}$1} surface remains when x''=1 and $x' > 0$; therefore x'' was optimised with x'=0 with the same result. Results for the $[5.0,0.51,x'']_2$ shape, shown in Figure 6.7(b), revealed no significant thermodynamic preference for any amount of truncation of the {10$\bar{1}$2} plane in the <0002> direction; however an optimum value was x''=0.76. This suggests that the apices of the {10$\bar{1}$2} pyramids may be eroded post-synthesis without any thermodynamic penalty, or that a 'rounded' termination is just as likely as a sharp one. Results for the $[2.5,0.52,x'']_3$ shape, shown in Figure 6.7(c), reveal a low energy group formed by truncation of the {10$\bar{1}$3} cap between $0 \leq x'' \leq 0.4$. The optimum value of x'' for the l = 3 shape was 0.0, illustrating that the sharp apex may be preserved only when a low angle is subtended at that apex (or conversely, when the index in the *c*-direction is high).

The self-consistently optimised values of x, x' and x'' in the $[x,x',x'']_l$ shapes were, respectively, 5.0, 0.51 and 0.76 for l=2; and 2.5, 0.51 and 0.0 for l=3. For l=1 the self-consistently optimised values were 5.5, 1.0 and 1.0, which is by definition the same shape found when optimising x, x' and x'' for l=0. With x'' held constant at 0.0 the optimised values of x and x' were 10 and 0.51, respectively. In general, the higher the index of the facets decorating the ends of the nanorod, the shorter the nanorod is likely to be.

6.3.7 Minimum energy morphology

The results above highlight how the optimal values of x, x' and x'' are intrinsically linked. A delicate balance exists between these geometric features, and identification of the minimum energy shape for WZ ZnS requires that each shape be optimised self-consistently. Self-consistent optimisation of x, x' and x'' in the $[x,x',x'']_l$ shapes resulted in values of 5.0, 0.51 and 0.76 for l = 2; and 2.5, 0.51 and 0.0 for l = 3. For l=1 these values were 5.5, 0.51 and 1.0; or for x''=0.0 the optimised values of x and x' were 10 and 0.51, respectively.

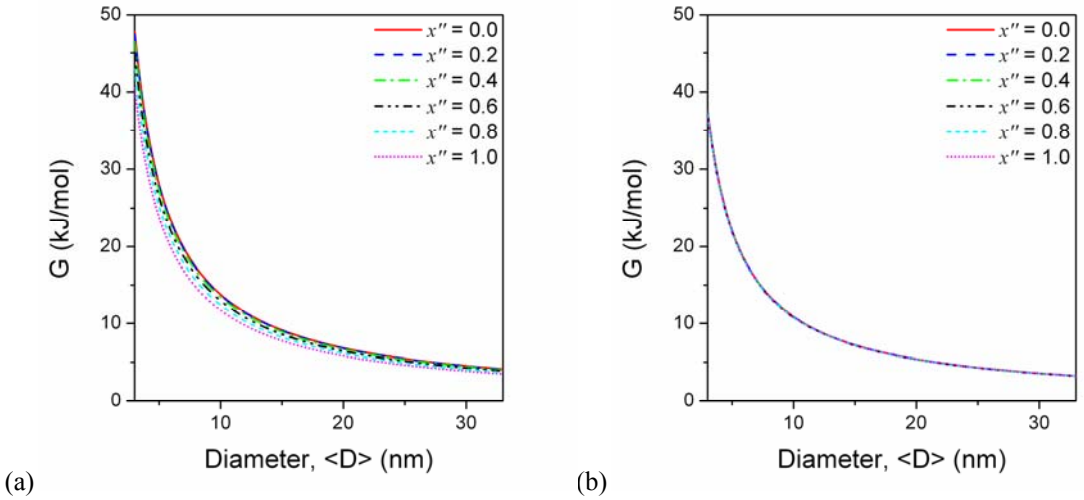

(a) (b)

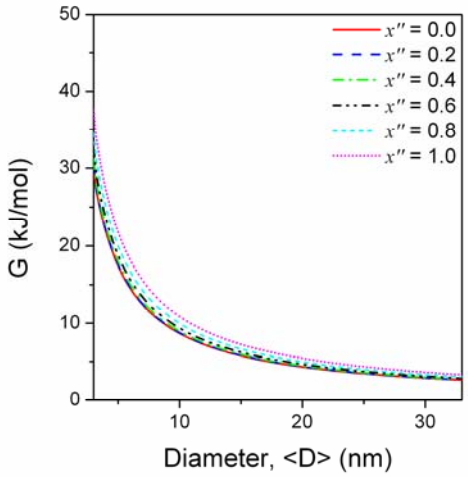

(c)

Figure 6.7 – Free energies for $[x_{opt},x'_{opt},x'']_l$ shapes for l = (a) 1, (b) 2 and (c) 3.

Figure 6.8 shows a comparison of the free energies for shapes optimized in x, x' and x'' with the exception of $[10,0.51,0.0]_1$ which is optimized in x, x' and held constant at x''=0 (to prevent this shape converging to the identical $[5.5,0.51,-]_0$ shape). In general, capping with l = 3 is favourable at all optimum prism aspect ratios. At higher ratios ~20 the l = 0, 2 and 3 caps are in co-existence.

Further insight into the equilibrium morphology was gained by taking a closer examination of how the aspect ratio affects the free energy across all sizes. The aspect ratio was varied between $0 \le x \le 20$ at sizes ranging from $3.0 \le D \le 18$ nm. The other shape

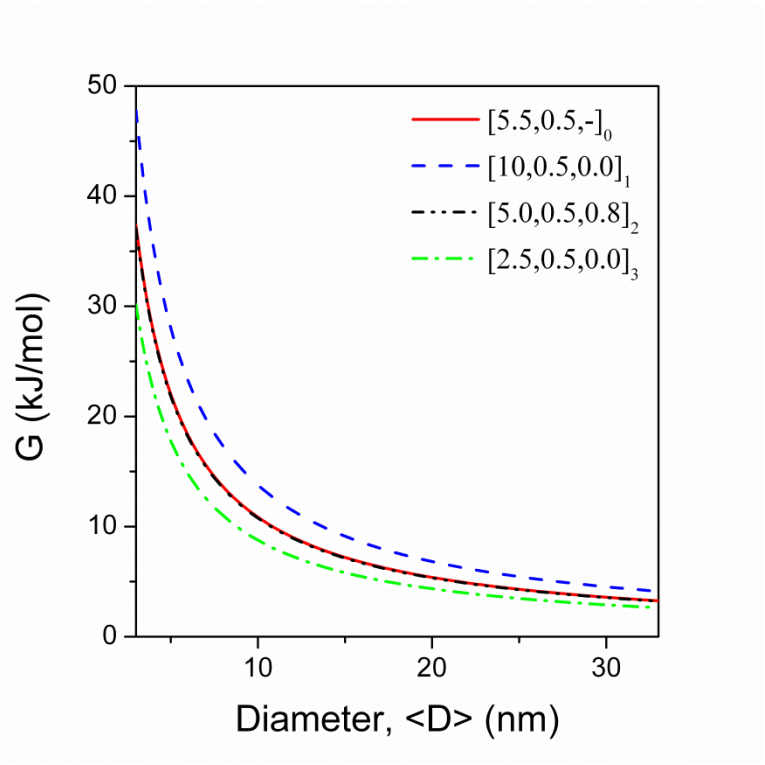

Figure 6.8 – Free energy of $[x,x',x'']_l$ shapes with optimized values of x, x' and x'' as a function of particle diameter.

variables, x', x'' and l were optimised self-consistently at every value of x to obtain the minimum free energy at each point in $<x,D>$ space. The optimum values for l and x'' were 3 and 0.0, respectively, for all x and D.

The resulting free energy surface in Figure 6.9 shows how the influence of aspect ratio on nanoparticle/nanorods stability changes with particle size. At smaller sizes (~3.0 – 10 nm) there is considerable thermodynamic advantage to be gained from producing nanoparticles with aspect ratios close to the equilibrium aspect ratio (~2), whereas at larger sizes, where the free energy surface becomes relatively flat, there is less change in the relative free energies, suggesting that in this region of particle size large variations in the aspect ratio are thermodynamically possible.

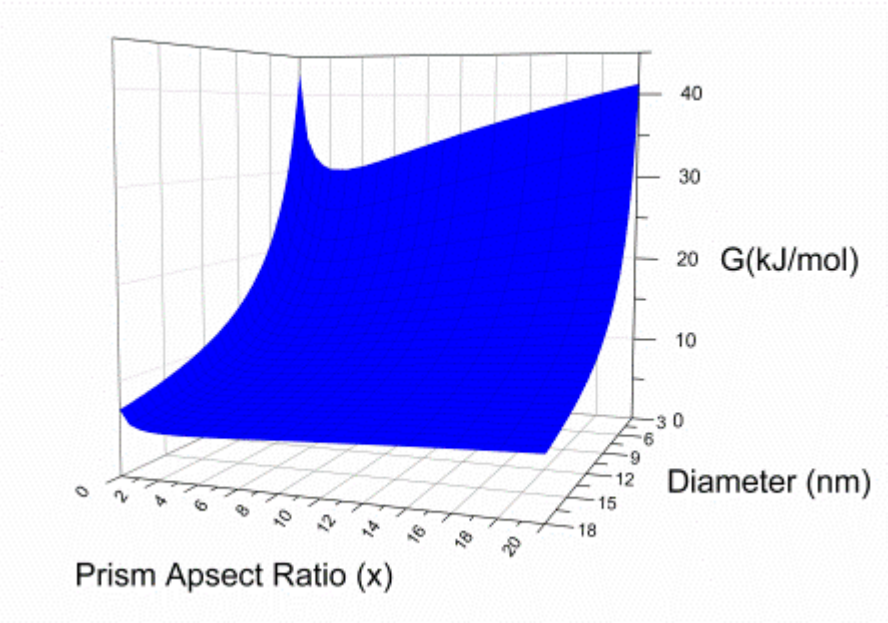

Figure 6.9 – The free energy surface with respect to prism aspect ratio (x) and average particle diameter (D) for which all other shape variables (x', x'' and l) where optimized at each point in $<x,D>$ space.

6.3.8 Wurtzite to zinc blende phase transformations

The occurrence of phase transformations in nanoparticles is often reported with reference to size alone. However, as shown below, variations in morphology effects the size at which phase transformations between ZB and WZ nanoparticles occur. Therefore, phase transformations were investigated with respect to size and shape. As prism aspect ratio is commonly reported in literature, the WZ shapes chosen for this part of the study had varying prism aspect ratios of x=0.5, 2.5 and 20. The aspect ratio of 2.5 was chosen as this produces the lowest free energy given complete degrees of freedom in the other shape variables (x', x'' and l). Aspect ratios of 0.5 and 20 were selected as small and large extremes. To obtain the minimum free energy shape for each aspect ratio the remaining shape variables were optimised for each value of x. This gave the $[0.5,1.0,0.0]_3$, $[2.5,0.5,0.0]_3$ and $[20,0.4,0.0]_3$ shapes. The free energies of these shapes were compared to three ZB shapes which were found in Chapter 5 to be members of a low energy ZB group across the nanoparticle size range $3 \leq D \leq 33$ nm. These ZB shapes are the pure rhombic dodecahedron (RD), composed

entirely of non-polar {220} facets, and the RD truncated by either {111} or {200} polar surfaces (Figure 6.10).

In order to appropriately determine the relative stabilities of these shapes, their free energies were plotted with respect to surface area per mole (m^2/mol). This description includes the surface-to-volume ratio *q*, and therefore captures both the size- and shape-dependence of the systems. From a comparison of the free energies of each these nanoparticles we find that a number of possible phase transformation sizes exist, depending on the specific shape being considered within each phase, as shown in Figure 6.11. For example, the ZB-RD shape is energetically preferred at all sizes, so no phase transformation to any WZ structure is expected should this pure shape be successfully formed. However, if {111} surfaces are introduced to the ZB-RD shape, the ZB phase is only thermodynamically stable above 44 nm (with respect to the WZ shapes described in this section), suggesting that a phase transformation to WZ is likely to occur in nanoparticles below this size. Alternatively, if {200} facets are introduced to the ZB-RD shape, this phase transformation size increases to 87 nm.

These transformation sizes assume that WZ has the opportunity to adopt the minimum energy shape, but we find that these cross-over points are elastic with respect to the aspect ratio of the WZ shapes (as well as being sensitive to the ratio of polar to non-polar facets on the ZB shapes). For example, in comparison to the ZB-RD shape truncated in the <111> direction, the $[0.5,1.0,0.0]_3$ WZ shape is predicted to be thermodynamically stable below 4.8 nm while the $[2.5,0.5,0.0]_3$ is thermodynamically favourable up to 33 nm and the $[20,0.4,0.0]_3$ up to 88 nm. With respect to the ZB-RD truncated in the <200> direction, the $[0.5,1.0,0.0]_3$ shape is predicted to be stable up to 46.5 nm, the $[2.5,0.5,0.0]_3$ up to 74 nm and the $[20,0.4,0.0]_3$ up to 159 nm.

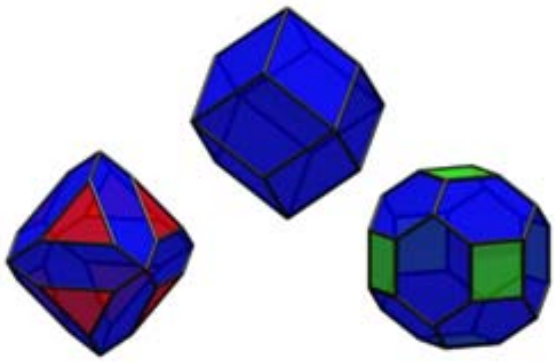

Figure 6.10 – ZB structure rhombic dodecahedrons truncated in (from left to right) the <111> direction (red), not truncated and truncated in the <100> direction (green). The proportions of {111} and {100} surfaces to the total surface area of the ZB shapes is 22%. These shapes were used to assess shape-dependent ZB/WZ phase transformation sizes.

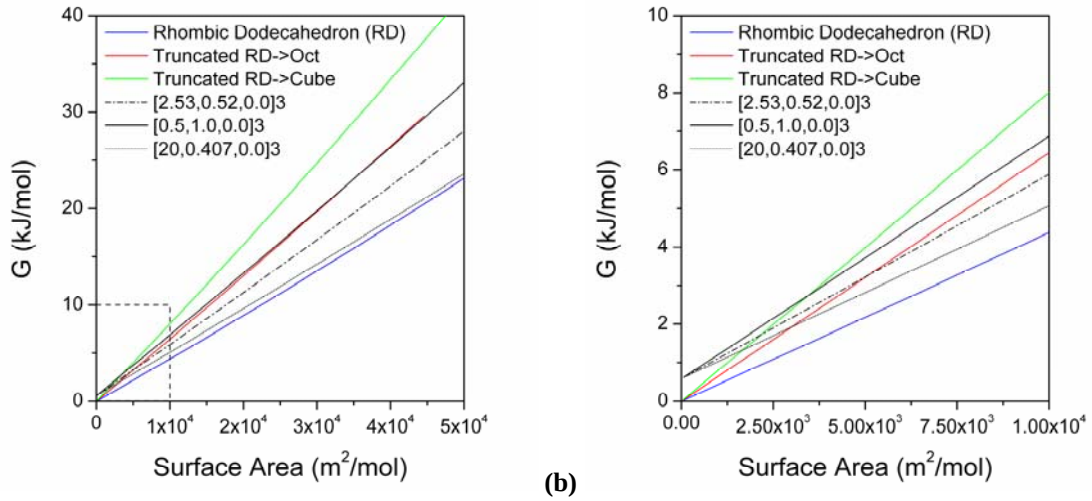

Figure 6.11 – Free energies for low energy WZ shapes with aspect ratios of 0.5, 2.53 and 20 and low energy ZB shapes from Figure 6.11. The relative free energies suggest that the pure rhombic dodecahedron morphology in the ZB phase is stable at all sizes, however with respect to other ZB morphologies a shape dependent ZB/WZ phase transformation sizes exist.

These sizes refer to the ZB diameter based on a spherical approximation (see Chapter 2), so it is pertinent to point out that when converting these values to the corresponding anisotropic WZ shapes one should consider whether or not an aspect ratio of 20 and an average diameter of 88 nm produces a WZ nanoparticle with a basal plane diameter greater than 3.0 nm (the size limit of applicability/range of interest for this order of shape dependent modelling). As a guide, if the basal plane diameter is 3 nm and the aspect ratio 20, this corresponds to a prism length of 30 nm. The average of these two diameters is 17.5 nm which, for nanoparticles with aspect ratios of 20, is the smallest nanoparticle diameter for which the model holds. Therefore, provided the ZB diameter is greater than 6 nm when we are comparing to a WZ nanostructure with an aspect ratio of 20, then the comparison is valid.

Beyond the inter-relationship between the different morphological parameters discussed above, these results also indicate that the size, shape and phase are intrinsically linked, and we are confronted with *shape-dependent ZB/WZ phase transformation sizes*, which sits in contrast to the conventional wisdom of a purely size-dependent phase transformation. Variations in the shape of the ZB nanoparticles, including the introduction of polar facets, will encourage a transformation to the WZ phase at small sizes; while decreasing the prism aspect ratio of WZ nanoparticles, or introducing the lower indexed pyramidal capping facets, will cause the nanoparticle to be more susceptible to a transformation to ZB as the size increases.

This is a 4-dimensional problem, but the relationship can be mapped in a 2-dimensional plane. The effect of the WZ aspect ratio and basal plane diameter on the ZB phase transformation size is shown in Figure 6.12, with respect to RD nanoparticles with various degrees of truncation in the <111> direction (as indicated). Alternatively, by determining the size at which phase transformations from WZ to ZB occur, at varying degrees of the RD shape in the <111> direction, we can determine the corresponding prism aspect ratio for any

basal plane diameter at which a phase transformation is expected. This allows us to produce a phase map which shows the regions in which each phase is stable for any WZ or ZB shapes. Depending on which features are best manipulated experimentally (the ZB shape or the WZ shape), this phase diagram provides a way of anticipating nanoparticle stability. This is highly desirable, when significant effort and expense has gone into fabricating specific ZnS nanostructures intended for particular optical, electronic and photovoltaic devices.

6.4 Conclusions

Surface and materials properties were calculated using DFT and a shape-dependent thermodynamic model used to explore the relationship between size, shape and stability of wurtzite ZnS nanostructures. By testing and optimising the aspect ratio, it was shown that WZ nanostructures exhibit a preference toward anisotropy. Nanorods are thermodynamically preferred over quasi-spherical nanoparticles, and the surface properties will be dominated by the facets decorating the sides of the prism (perpendicular to the principal axis of the nanorod). With respect to the preferred orientation of these facets might be, an almost equal mix of $\{10\bar{1}0\}$ and $\{11\bar{2}0\}$ facet is preferred (producing a dodecagonal prism), but alternative prisms are in thermodynamic coexistence within the accuracy of the model, so the orientation of the prism facets is likely to be governed by kinetic factors.

In regard to pyramidal terminations ('caps') on the ends of the nanorods, the higher the index of the capping facet, the shorter the nanorod is likely to be. Furthermore, flat {0002} terminations are preferred over $\{10\bar{1}1\}$ facets, pyramid terminations with $\{10\bar{1}2\}$ facets will be truncated in the <0002> direction (giving a more 'rounded' appearance), and pyramid terminations with $\{10\bar{1}3\}$ facets may retain their sharp apices.

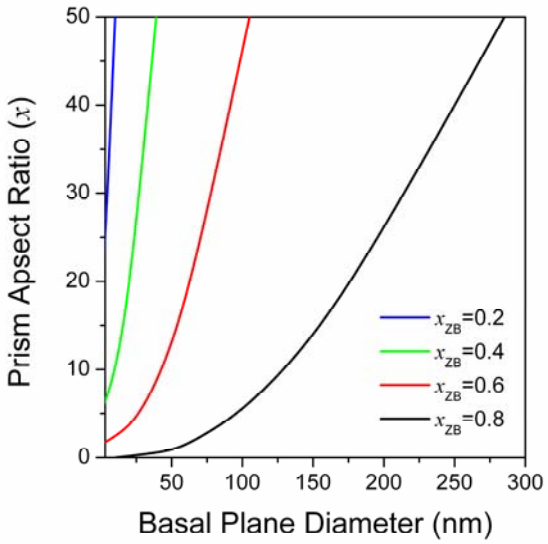

Figure 6.12 – The effect of the WZ aspect ratio and basal plane diameter on the ZB phase transformation size. The ZB shapes concerned are the rhombic dodecahedron morphology truncated in the <111> direction to an extent indicated by xZB, where 0 would represent the RD and 1 a pure octahedron covered by {111} planes. This phase diagram provides a way of anticipating when ZnS nanoparticles are likely to be stable, with WZ prism aspect ratio/basal plane diameter combinations being stable above respective ZB transformation boundary.

In general, there is a delicate balance between these different geometric features, and identification of the minimum energy shape for WZ ZnS requires that each shape be optimized self-consistently. Once identified, the free energies of low energy WZ shapes were compared with low energy ZB shapes (identified in Chapter 5), revealing a tenuous relationship between the morphology of WZ and the morphology of ZB and phase transformations sensitive to both. The size, shape and phase were shown to be intrinsically linked, and the shape-dependent ZB/WZ phase transformation size in the space defined by the important geometric features was mapped.

These results show that variations in the shape of the ZB nanoparticles, including the introduction of polar facets, will encourage a transformation to the WZ phase at small sizes; while decreasing the prism aspect ratio of WZ nanoparticles, or introducing the lower indexed pyramidal capping facets, will cause the nanoparticle to be more susceptible to a transformation to ZB as the size increases. This behaviour (shape dependent phase

transformation) is an important issue to consider when designing nanomaterials with shape and phase dependent properties that must remain stable for their effective use. However, there are a range of environmental considerations that may also include shape and phase selectivity. These include finite temperatures, different supersaturation of sulphur and adsorbed groups (such as water) on the surface. The topic of temperature/supersaturation affects are investigated in subsequent Chapters 7 and 8.

Chapter 7. Modelling Nanoscale Cubic ZnS Morphology and Thermodynamic Stability Under Sulphur-Rich Conditions

7.1 Introduction

The temperature and partial pressure of vapour phase elements can have a strong influence over the morphology and surface states[182-184] of nanoparticles during synthesis, as well as in broader, post-synthesis environments. As a result, these thermodynamic variables are frequently manipulated in order to accomplish specific experimental aims, such as fabricating useful morphologies and restricting the distribution of sizes (*D*) and shapes. However, owing to the highly complex, multi-dimensional phase space involved, an accurate description of morphological response to changes in thermodynamic states remains highly elusive. As discussed in Chapters 1 and 2, thermodynamic cartography is a powerful method which is useful in meeting this challenge, by predicting the low energy or equilibrium shapes (those that are expected given sufficient time or thermodynamic driving force) with respect to the dominant thermodynamic state variables. For systems where thermodynamic influence is significant, the morphology can be mapped, and used as a guide for modifying experimental conditions to meet synthesis aims, as well as increasing post-synthesis stability by facilitating structure prediction and restricting the occurrence of unwanted, thermodynamically driven morphology transformations.

The effect of sulphur temperature (*T*) partial pressure (*P*) on the stability of polar faceted ZB morphologies is reported in this chapter. Of the many promising applications of ZnS nanoparticles described in Chapter 1, catalytic and bio-technology applications in particular require specific polar surfaces with either cation or anion terminations to determine the available catalytic reactions[120,185,186] or functionalisation with particular molecules[9,29-31]. This makes a study of polar faceted morphologies highly valuable, with a view to enhancing

the efficiency of synthesis techniques and preventing post-synthesis morphology transformations. The work presented in this chapter was published in reference 187.

7.2 Theoretical and Computational Method

The shape-dependent thermodynamic model in Eq 3.12 was used to model ZB shapes in this section and predict their relative stabilities. The three polar, crystalline surfaces included in this study are the {311}, {100} and {111}, as identified in the X-ray diffraction (XRD) peaks for cubic phase ZnS (JCPDS card: 77-2100). These peaks provide an indication of the surfaces found on ZB ZnS nanoparticles; however they do not represent an efficient criterion alone to predict equilibrium crystal morphologies. The equilibrium structure is defined by the relative proportion of these facets, as expressed in Eq 3.12. The non-polar {110} XRD peak is also reported in literature and was studied in Chapter 5. The investigation in this chapter was restricted to polar surfaces, which are crucial to the kinds of applications described above. In addition, this allows for the use of *ab initio* thermodynamic techniques (which require a non-stoichiometric condition to establish temperature and sulphur supersaturation dependence (Eq 3.15)).

These polar surfaces possess a dipole moment perpendicular to the surface plane. This must be considered when performing DFT calculations to minimise contributions to the total energy associated with this dipole. Primarily, it is the interaction of surfaces across the crystalline slab and with the periodic images of the DFT cell which must be treated. These effects are counteracted by generating a slab of sufficient thickness and introducing ample vacuum space to achieve convergence of the surface energy[188] (according to Eq 3.15). Furthermore, surface relaxations (Figure 7.3, Table 7.1) during geometry optimisation will alter this dipole moment, ideally leading to physically accurate surface arrangements and dipole moments.

The most effective DFT approach for ZnS, as reported in Chapter 4, was used to calculate these surfaces, which were constructed in VASP using 2x2x2 conventional supercells. Convergence with respect to slab thickness was established when the bulk-like lattice constant was preserved at the centre of the slabs following a full relaxation, and was achieved at 25 atomic layers. Total energy convergence with respect to vacuum space was achieved at 30 Å for the {111} and {100} surfaces and 20 Å for the {311} surface, as shown in Figure 7.1. The atomic species (Zn or S) of the coloured atoms in Figure 7.1 is arbitrary as a result of the symmetry of the space group. Therefore these slabs may represent either the S- or Zn-terminated surfaces equivalently, but not concurrently (with respect to the alternate faces of an individual single slab). With respect to differences in opposing faces of the {111} and {311} slabs, the geometric nature of the thermodynamic model ensures that the nanoparticle will possess equal proportions of each (e.g. (111) and ($\bar{1}\,\bar{1}\,\bar{1}$)). Therefore explicit calculations of opposing faces are unnecessary, as the calculations involving twin-surface slabs shown here will be consistent within the symmetric framework of the model.

Surface energies were calculated according to Eq 3.18, subject to the range of applicability for ln$P(S)$ in Eq 3.19. The values of E_i, $\mu_{ZnS,bulk}$, $\mu^{o}_{ZnS,bulk}$, $\mu^{o}_{Zn,bulk}$ and $\Delta H_{f,bulk}$ in Eq 3.18 are reported in Chapter 4.

each case.

7.2.1 Modelling ZB shapes with polar surfaces

The shapes enclosed entirely by each of the {311}, {100} and {111} surfaces are, respectively, the deltoidal icositetrahedron (DI), regular hexahedron or cube (C), and octahedron (O). A continuous spectrum of morphologies can be formed by combining these surfaces in varying proportions; therefore, to facilitate effective analysis a sub-set shapes was created to make an initial sample of this morphology space (Figure 7.2). Thermodynamic modelling of these shapes was followed by a shape optimisation routine to find the exact

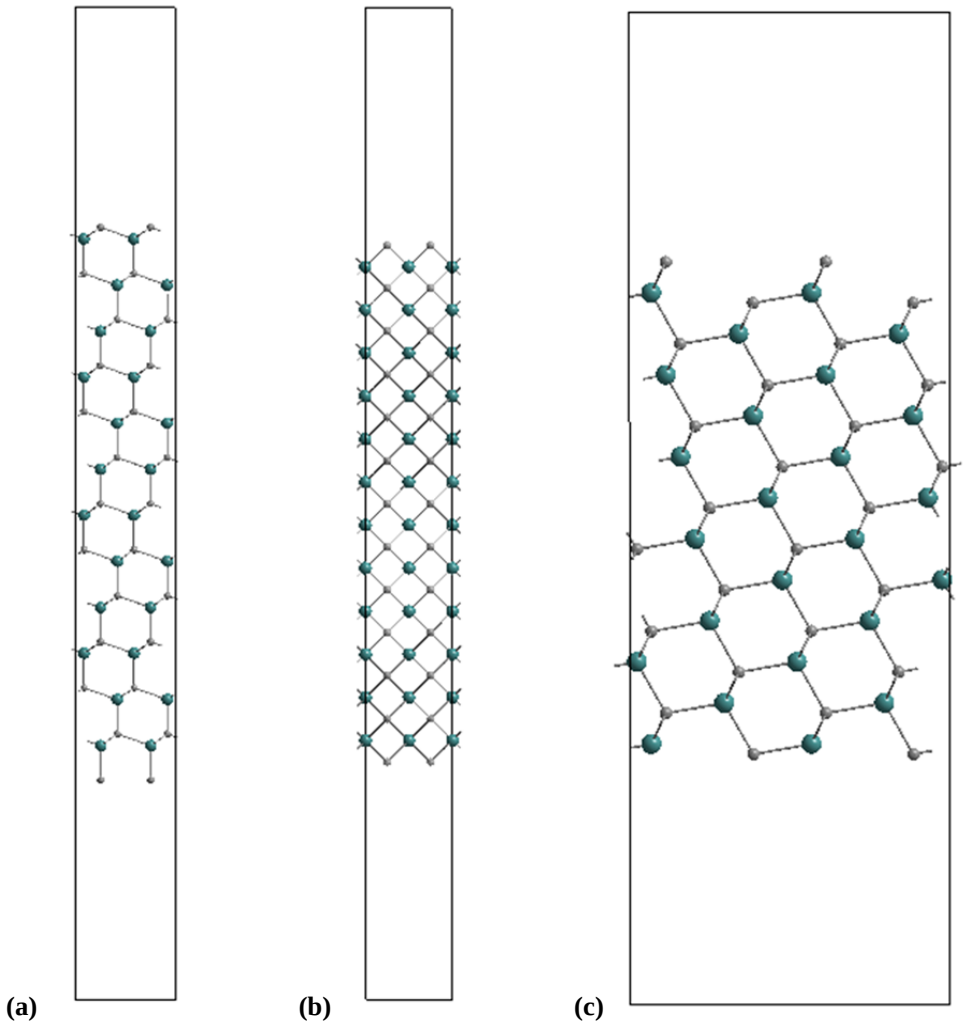

Figure 7.1 – Non-stoichiometric slabs, containing 25 atomic layers of ZnS, oriented to represent (a) {111}, (b) {100} (c) {311} surfaces. Vacuum space of 30 Å was required for energy convergence of the {111} and {100} slabs and 20 Å for the {311}. Owing to the symmetry of the zinc blende space group, Zn and S can be assigned arbitrarily to either blue or grey coloured atoms, as each can occupy similar sites depending on the terminating species i.e. the terminating species is definitively represented by the small, grey atoms, which have greater abundance over the large blue atoms in each slab. The requirement of non-stoichiometry, that both surfaces are terminated with the same atomic species, is satisfied in

point within the morphology continuum where the free energy modelled with respect to size, temperature and pressure is minimised.

The shape-dependent parameters contained in the thermodynamic model (Eq 3.12) are the surface-to-volume ratio q and the facet weighting factors f_i. Appendix A provides the expressions for q and f_i required for the shapes shown in Figure 7.2. By varying the shape

truncation factor x contained in the q and f_i parameters between the limits of $0 \leq x \leq 1$ the morphology space between shapes can be modelled continuously. For example, the shape truncation factor for the (O-DI) shape is 0.65. However, in the region $0 \leq x \leq 1$ the q and f_i expressions for all shapes between (DI-O) and (O) can be determined, where the limit $x=0$ is equivalent to (O) and $x=1$ equivalent to (DI-O).

For this study, a naming convention was formed from abbreviations of the shape names above. In the case of shapes with facets of more than one orientation, the abbreviations are ordered with respect to the shape corresponding to the dominating facet. For example, in the case of the cubeoctahedron (C-O), which has the quality of being an Archimedean solid, 63% of the surface area is faceted by {100} planes, while the remaining 37% is {111}, therefore in the label (C-O) the abbreviation for cube C precedes that of octahedron (O). The ratio of {111}/{100} surfaces covering the truncated octahedron (O-C) shape, also an Archimedean solid, is 0.78/0.22. This ratio was used to define the (DI-C) and (O-DI) shapes, which share the ratios of their respective {311}/{100} and {111}/{311} surfaces in common with the truncated octahedron. The (C-DI) and (DI-O) shapes represent truncation limits between the (C) and (DI) shapes, and the (O) and (DI) shapes, respectively.

7.3 Results and Discussion

7.3.1 Surface modelling

Relaxed S- and Zn-terminated surfaces from geometry optimisation calculations in VASP are shown in Figure 7.3. Atomic displacements of the two terminating layers (one Zn and one S) from each end of the slab, in directions normal to the surface planes, are labelled in Figure 7.3 and the values given in Table 7.1.

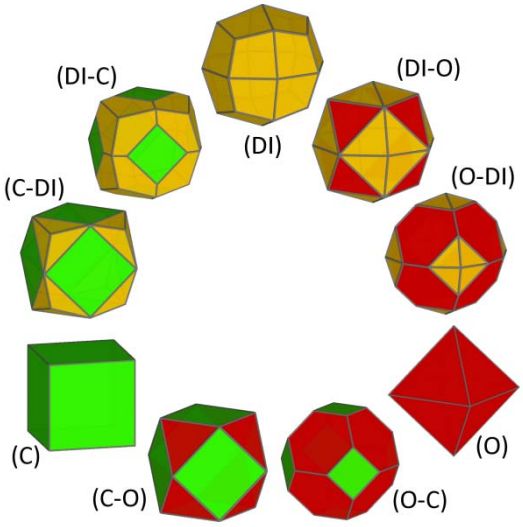

Figure 7.2 – A sub-set of shapes enclosed by the polar ZnS surfaces of cubic ZnS, as identified by XRD (JCPDS card: 77-2100). This sub-set spans the continuous, closed morphology space defined by the polar surfaces of cubic ZnS, and was used to determine the region in which the minimum free energy, or equilibrium shape would be located. Optimization of the truncation factor (a continuous variable which defines the proportion of each surface facet in the model) was also performed to determine the precise equilibrium morphology with respect to <*D*,*T*,*P*> space.

7.3.2 Shape modelling

Surface energies were calculated according to Eq 3.18 and are shown in Figure 7.4 at T=300 K. The ln$P$(S) limits correspond to Zn-rich/S-poor conditions at the lower end of the ln$P$(S) scale and S-rich/Zn-poor conditions at ln$P$(S)=0.0 (corresponding to the standard state condition in Eq 3.17). As seen in Figure 7.4, the surface energies of Zn-terminated surfaces increase and S-terminated surfaces decrease linearly with ln$P$(S). From Eqs 3.18 and 3.19 it is evident that varying the temperature will alter the defined range of ln$P$(S), however the surface energies themselves across this range are naturally independent of T.

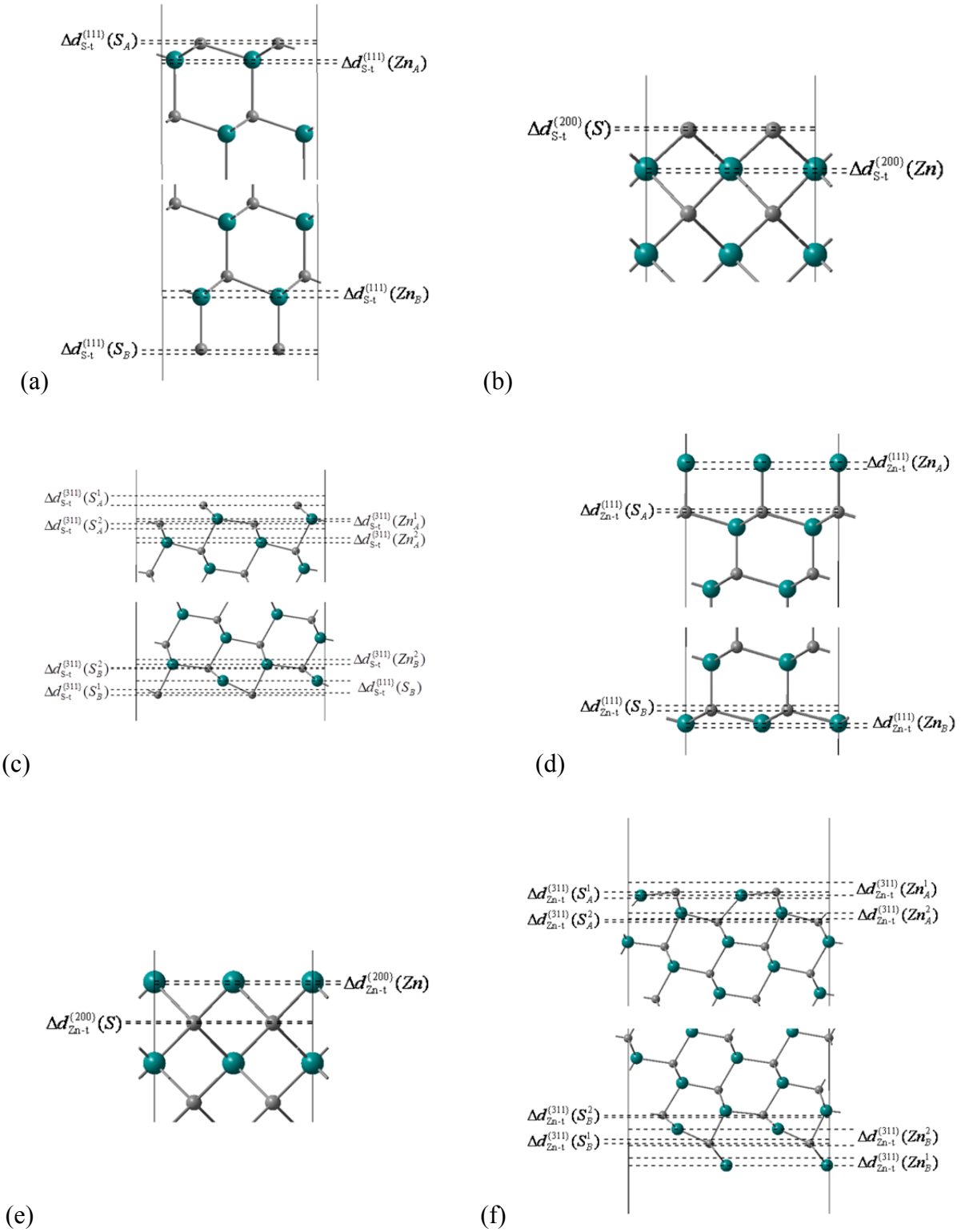

Figure 7.3 – Relaxed surface configurations following DFT geometry optimisation calculations. Labels for the atomic layer displacements refer to the surface orientation in superscript, the terminating species in subscript (S-t = S-terminated; Zn-t = Zn-terminated), the layer atomic species in brackets, and an arbitrarily assigned value (A or B) used to differentiate opposing surface configurations at each end of the crystal slab (not required for the {100} due to symmetry about the axis normal to the surface). For the {311}, the second terminating layer was also included due to the degree of exposure of these layers to the vacuum space. These labels include a superscript value on the atomic species which indicates the order of each layer with respect to the vacuum space.

Table 7.1 – Displacements Δd of the S and Zn surface layers in the direction normal to the surface plane. All values are in Angstroms. Positive displacement occurs in the direction of the above surfaces in Figure 7.3.

$\Delta d_{S-t}^{\{111\}}(S_A) = -0.04$	$\Delta d_{S-t}^{\{311\}}(S_A^1) = -0.27$
$\Delta d_{S-t}^{\{111\}}(Zn_A) = 0.05$	$\Delta d_{S-t}^{\{311\}}(S_A^2) = 0.12$
$\Delta d_{S-t}^{\{111\}}(S_B) = 0.03$	$\Delta d_{S-t}^{\{311\}}(Zn_A^1) = 0.04$
$\Delta d_{S-t}^{\{111\}}(Zn_B) = -0.08$	$\Delta d_{S-t}^{\{311\}}(Zn_A^2) = 0.10$
	$\Delta d_{S-t}^{\{311\}}(S_B^1) = -0.14$
$\Delta d_{Zn-t}^{\{111\}}(Zn_A) = 0.10$	$\Delta d_{S-t}^{\{311\}}(S_B^1) = -0.01$
$\Delta d_{Zn-t}^{\{111\}}(S_A) = -0.04$	$\Delta d_{S-t}^{\{311\}}(Zn_B^1) = 0.40$
$\Delta d_{Zn-t}^{\{111\}}(Zn_B) = 0.04$	$\Delta d_{S-t}^{\{311\}}(Zn_B^2) = -0.13$
$\Delta d_{Zn-t}^{\{111\}}(S_B) = -0.07$	
	$\Delta d_{Zn-t}^{\{311\}}(Zn_A^1) = -0.38$
$\Delta d_{S-t}^{\{200\}}(S) = -0.05$	$\Delta d_{Zn-t}^{\{311\}}(Zn_A^2) = 0.16$
$\Delta d_{S-t}^{\{200\}}(Zn) = 0.06$	$\Delta d_{Zn-t}^{\{311\}}(S_A^1) = 0.24$
	$\Delta d_{Zn-t}^{\{311\}}(S_A^2) = -0.04$
$\Delta d_{Zn-t}^{\{200\}}(Zn) = 0.06$	$\Delta d_{Zn-t}^{\{311\}}(Zn_B^1) = -0.28$
$\Delta d_{Zn-t}^{\{200\}}(S) = 0.01$	$\Delta d_{Zn-t}^{\{311\}}(Zn_B^2) = 0.39$
	$\Delta d_{Zn-t}^{\{311\}}(S_B^1) = -0.13$
	$\Delta d_{Zn-t}^{\{311\}}(S_B^2) = 0.05$

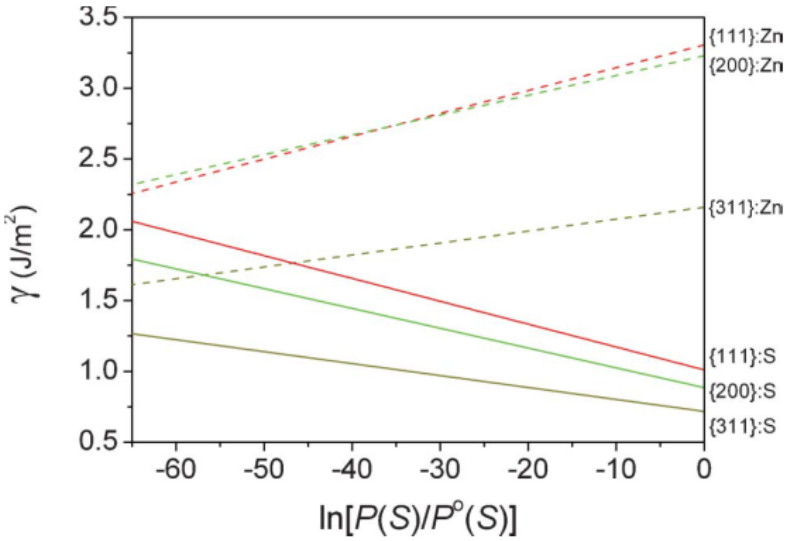

Figure 7.4 – Specific surface energies of formation for S- and Zn-terminated surfaces with respect to the partial pressure of sulphur.

To commence investigating the relationship between equilibrium morphology and the thermodynamic variables of temperature and pressure <*D,T,P*> space was first sampled by comparing the free energies of the (DI), (O) and (C) shapes at several broadly distributed *D, T, P* points. For this purpose, values of <*D*> = 5 and 50 nm, *T*=300, 450, 600 K, and ln*P*(S)= -32.5, -18.6 and 0.0 were chosen. Results are shown in Figure 7.5, revealing an overall preference for the (DI) shape covering this broad <*D,T,P*> region. However the extent of the thermodynamic preference varies considerably and in some regions is very minor. For example, while temperature has little effect on the relative stabilities of these three shapes, changes in the sulphur supersaturation effect the relative stabilities more significantly. Thermodynamic preference for the S-terminated (DI) shape is greater in S-poor conditions, while in S-rich conditions the S-terminated (C) and (O) shapes are almost energetically equivalent to the (DI). This relationship between equilibrium morphology and sulphur supersaturation indicated that when kinetic processes are to be used in the formation of non-equilibrium shapes it would best be done under S-rich conditions, where thermodynamics have less influence.

For Zn-terminated surfaces the reverse trend is seen, with the (DI) shape becoming increasingly favourable with ln*P*(S). There is also a greater thermodynamic preference for the Zn-terminated (DI) morphology over the (C) and (O) shapes (when compared to the relative free energies of the S-terminated shapes) throughout this region of <*D,T,P*> space. This increase in the energetic preference indicates that when Zn-terminated surfaces are formed, the significance of thermodynamics in determining morphological selectivity is also increased.

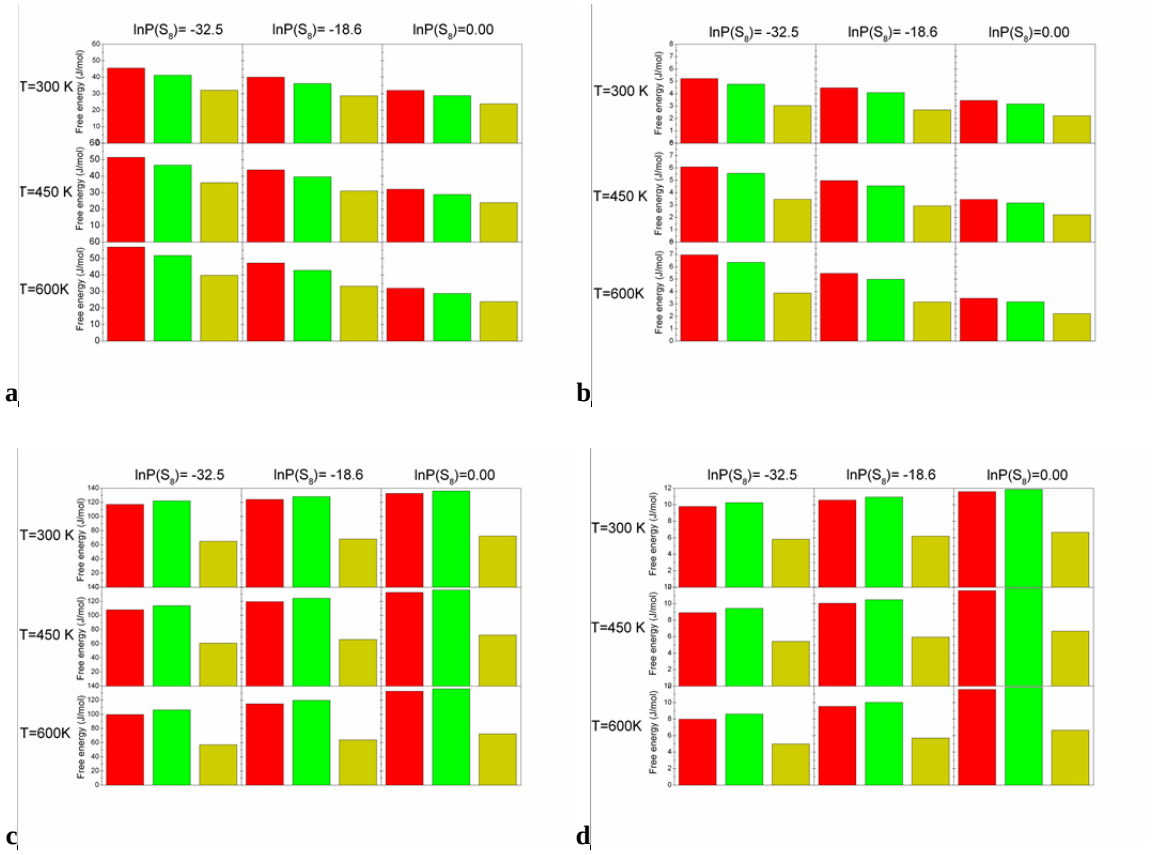

Figure 7.5 – An initial sample of <*D*,*T*,*P*> space, taken by comparing the total free energies belonging to 5 nm ((a) and (c)) and 50 nm ((b) and (d)) (O), (C) and (DI) shapes (coloured red, green and yellow, respectively) with S-terminated ((a) & (b)) and Zn-terminated ((c) & (d)) surfaces at nine different temperature/pressure points.

To examine the equilibrium morphology occupying this <*D*,*T*,*P*> space in greater detail, free energies as functions of size were compared for all shapes in Figure 7.2, under S-rich and S-poor conditions at 300 K. In the resulting set of free energy curves (Figure 7.6) the S-terminated (DI) shape is clearly favourable across a large size range. However, these results also reveal the existence of a low energy *group* consisting of the (DI), (DI-O) and (DI-C) shapes. This group includes the (C-DI) shape when the concentration of sulphur is high. Furthermore, within this group there appears to be some convergence in the free energies at very small sizes; however this is difficult to ascertain from Figure 7.6, using energy as a function of size. In Figure 7.7, we see the results of plotting energy as a function of surface area per mole. These results show multiple crossover points between the low energy {311} dominated and the {100} dominated shapes. Comparing the results for the two partial pressures (Figures 7.7 (a) and (b)), there is a shift in the crossover points towards larger sizes

as sulphur concentration increases. To clarify this, the energetic intersection of the (DI) and (C) shapes under both sets of conditions are indicated by arrows. This shift and the existence of energetic crossovers suggests that a large variety of shapes, with {311}, {100} and/or {111} surfaces, could be formed with the use of kinetic processes, providing sulphur concentrations are favourably rich and sizes are kept small. Further mapping of $<D,T,P>$ space required additional analysis similar to that conducted above; however no significant finds were made which effected the conclusions drawn from the analysis above.

Having established thermodynamic preference for the (DI) shape, the optimised equilibrium shape in a continuous morphology space was established by varying the value of x in the expressions for q, f_{311} and f_{111} or f_{200} for each of the (DI-O) and (DI-C) shapes, respectively, until a minimum value for the sum of the free energies over all sizes was found. The optimisation minimises any trade-off that could occur between the need to maximise coverage of low energy facets and minimise the surface to volume ratio and surface tension (even at the expense of introducing higher energy facets). In both directions, an optimum value of x=0.0 was found, indicating there is no thermodynamic advantage in truncating the (DI) shape, consisting entirely of relatively low energy {311} surfaces, in order to lower the surface to volume ratio or relieve strain caused by {311} surface tension.

7.4 Conclusions

Vapour pressure and temperature are commonly used to control the formation and growth of nanoscale morphologies. An accurate description of the relationship between these thermodynamic variables and equilibrium morphology has the potential to bring about improvements in methods for targeted nanostructure engineering, and provides a tool to assess and encourage long-term stability of equilibrium and non-equilibrium nanostructures.

Figure 7.6 – Free energy as a function of size for S-terminated shapes (Figure 7.2) at 300 K and ln$P$(S) = (a) -32.5 and (b) 0.0.

In this work, a shape-dependent thermodynamic model was used to examine the relationship between the equilibrium morphologies of cubic ZnS nanoparticles enclosed by polar {111}, {100} and {311} facets, their size (D) and the partial pressure (P) and temperature (T) of sulphur vapour in the surrounding environment. Initially a series of points in <D,T,P> space was sampled using a three shapes, revealing trends in energy along the sulphur partial pressure domain and between the alternate surface terminating species. These trends led to conclusions in regards to how experimental conditions could be tailored to target specific needs. Specifically, a lower variance in energy for structures under S-rich conditions (when compared to S-poor) was observed. Also for the Zn-terminated surfaces, a significantly larger thermodynamic preference for the (DI) over the (O) and (C) occurs (when

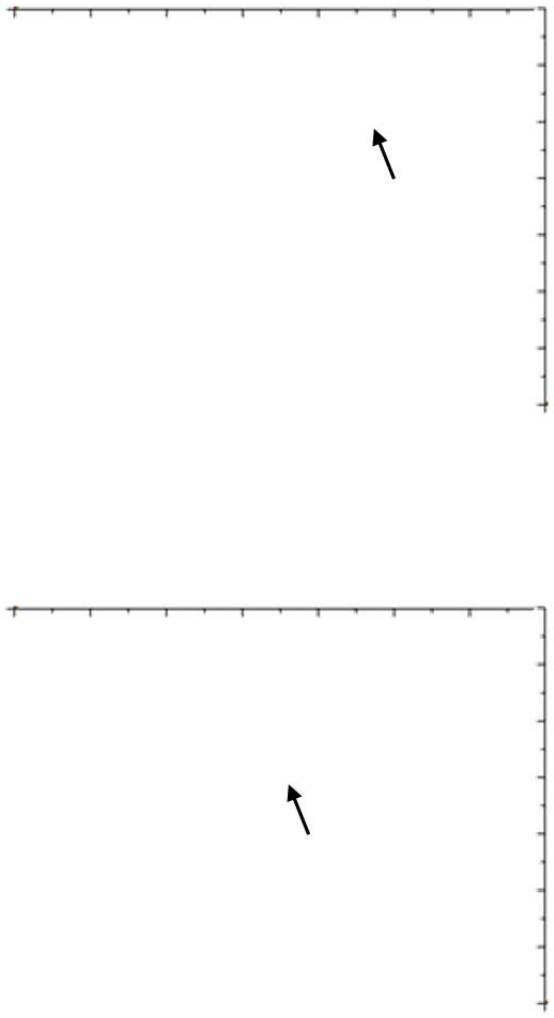

Figure 7.7 – Free energy as a function of surface area per mole for S-terminated shapes (Figure 7.2) at 300 K and ln*P*(S)= (a) -32.5 and (b) 0.0.

compared to the preference for the (DI) with S-terminations). However it is important to note that the (DI) shape enclosed by S-terminated surfaces is significantly lower in energy than the (DI)/Zn-terminated.

Based on these findings, if non-equilibrium structures are to be formed, a S-rich environment will assist these outcomes, as thermodynamic influence appears weakest under these conditions. Suppressing growth or restricting Zn-terminated surfaces will also aid these processes, while encouraging Zn-terminated surfaces to form will increase the influence of

thermodynamics over morphological selectivity, resulting in a greater likelihood of forming a low energy equilibrium or quasi-equilibrium arrangement.

Having identified the effects caused by changes in sulphur partial pressure, and finding that little effect was caused by changes in temperature, a more detailed examination of the equilibrium morphology was performed by modelling an additional six shapes, to make a total of nine, and plotting their energies with respect to size at 300 K and the extremes of the range of sulphur partial pressures [ln$P$(S)=-32.5 and 0.0] as defined by Eq 3.18. These energies were also plotted against surface area per mol, to aid in the identification of thermodynamic crossovers. The findings and conclusions made from these results are as follows:

1. The (DI) shape is found to have the lowest energy across a broad range of sizes irrespective of the abundance of sulphur.
2. The energies of the (DI-O) and (DI-C) shapes appear only slightly higher than (DI), irrespective of sulphur concentration and size. These shapes form a low energy *group* in which shape selection may be governed by kinetics.
3. Under S-rich conditions the (C-DI) shape is also part of this group. This suggests that increasing the concentration of sulphur in the environment causes a spread in the domain of thermodynamically favoured or equilibrium shapes.
4. The thermodynamic crossover points shift to larger sizes as sulphur concentration increases.
5. At small sizes and under suitably S-rich conditions growth of the polar facets will most likely be controlled by kinetics.
6. A shape optimisation was performed to find the exact point within the continuous morphology space which minimises the overall free energy. The (DI) shape with no truncations was produced in this process.

7. With reference to a set of experimental studies which reveal competing octahedron and tetrahedron tetrapod core morphologies, the octahedron morphology was found to be thermodynamic preferred in the size range 3 – 33 nm at T=1000^{o}C, irrespective of sulphur concentrations. For the formation of a tetrahedron core, S-rich conditions are most favourable. Importantly, the S-rich condition is critical when particle sizes are small, as the thermodynamic preference for the octahedron shape is highest for small nanoparticles in Zn rich environments.

Chapter 8. Modelling polar wurtzite ZnS nanoparticles: the effect of sulphur supersaturation on size- and shape-dependent phase transformations

8.1 Introduction

As discussed in Chapter 7, the temperature (T) and pressure (P) of vapour phase elements have a strong influence over nanoparticle phase and morphology. In this chapter the thermodynamic influence of sulphur vapour temperature and supersaturation on the morphology of ZnS nanoparticles in the WZ phase is reported. Equilibrium shapes as a function of the dominant thermodynamic variables are established, the significance of thermodynamics in determining the shape selectivity is assessed, and the regions where kinetics might be best employed for non-equilibrium shape control are highlighted. These results are compared to those in Chapter 7 relating to the ZB phase, to reveal size- and shape-dependent phase transformations, and the thermodynamic regions in which specific shapes, once formed, can be considered stable across a broad thermodynamic regime. The work presented in this chapter was published in reference 189.

8.2 Theoretical Method

The shape-dependent thermodynamic model in Eq 3.12 was used to model WZ shapes in this section and predict their relative stabilities. The four polar, crystalline surfaces included in this study are the {0002}, {10$\bar{1}$1}, {10$\bar{1}$2} and {10$\bar{1}$3} surfaces, as identified in the XRD peaks for wurtzite phase ZnS (JCPDS card: 36-1450). The non-polar {10$\bar{1}$0} and {11$\bar{2}$0} XRD peaks are also reported in literature and were studied in Chapter 6. The investigation in this chapter was restricted to polar surfaces, which are crucial to the kinds of applications highlighted in Chapter 7. In addition, this allows for the use of *ab initio* thermodynamic techniques (which require a non-stoichiometric condition to establish temperature and sulphur supersaturation dependence (Eq. 3.15)). As discussed in Chapter 7, surface dipole effects were treated through geometry optimisations and generating a slab of sufficient thickness and

introducing ample vacuum space to allow convergence of the surface energy(according to Eq. 3.15).

The most effective DFT approach for ZnS, as reported in Chapter 4, was used to calculate these surfaces, which were constructed in VASP using 2x2x2 conventional supercells. Convergence with respect to slab thickness was established when the bulk-like lattice constant was preserved at the centre of the slabs following a full relaxation, and was achieved for the {0002}, {10$\bar{1}$1}, {10$\bar{1}$2} and {10$\bar{1}$3} surfaces at 21, 30, 31 and 41 atomic layers, respectively. Total energy convergence with respect to vacuum space was achieved at 30 Å, as shown in Figure 8.1. The atomic species (Zn or S) of the coloured atoms in Figure 8.1 is arbitrary as a result of the symmetry of the space group. Therefore these slabs may represent either the S- or Zn-terminated surfaces equivalently, but not concurrently (with respect to the alternate faces of an individual single slab). As stated in Chapter 7, with respect to differences in alternate faces of each slab, the geometric nature of the thermodynamic model ensures that the nanoparticle will possess equal proportions of each (e.g. (0002) and (000$\bar{2}$)). Therefore explicit calculations of opposing faces are unnecessary, as the calculations involving twin-surface slabs shown here will be consistent within the symmetric framework of the model. Surface energies were calculated according to Eq 3.18, subject to the range of applicability for ln$P$(S) in Eq 3.19. The values of E_i, $\mu_{ZnS,bulk}$, $\mu^{o}_{ZnS,bulk}$, $\mu^{o}_{Zn,bulk}$ and $\Delta H_{f,bulk}$ in Eq 3.18 are reported in Chapter 4.

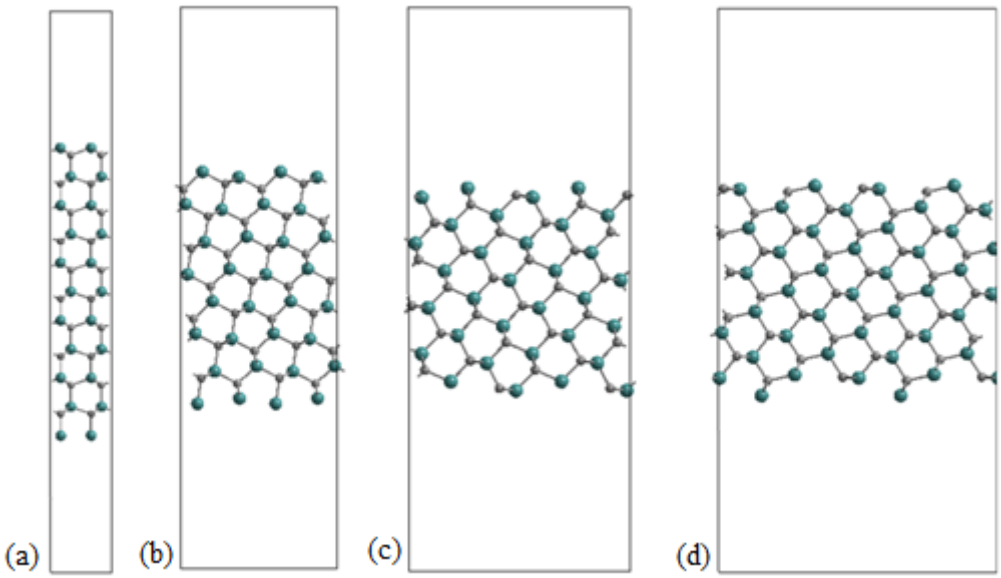

Figure 8.1 – Non-stoichiometric slabs representing (a) {0002}; (b) {10$\bar{1}$1}; (c) {10$\bar{1}$2}; and (d) {10$\bar{1}$3) surfaces. Owing to the symmetry of the wurtzite space group, Zn and S can be assigned arbitrarily to either blue or grey coloured atoms, as each can occupy similar sites depending on the terminating species i.e. the terminating species is definitively represented by the larger, blue atoms, which are greater in number than the smaller, grey atoms in each slab. The requirement of non-stoichiometry, that both surfaces are terminated with the same atomic species, is satisfied in each case.

8.2.1 Modelling WZ shapes with polar surfaces

For the purpose of this study on polar surfaces a closed set of nanoparticle shapes was established, consisting of hexagonal bipyramids consisting of {10$\bar{1}$1}, {10$\bar{1}$2} or {10$\bar{1}$3} facets with truncation in the <0001> directions to form {0002} facets on opposing apexes. Similar to Chapter 6, truncation in the <0001> direction was represented by the shape modelling variable x'' within the range $0 \leq x'' < 1$, where $x''=0$ represents no truncation and $x''=1$ is complete truncation of the pyramidal facets (note that as $x'' \rightarrow 1$, volume$\rightarrow$0, hence $q \rightarrow \infty$ and $G \rightarrow \infty$, so $x<1$ for all shapes). For convenience, when describing specific shapes, the {10$\bar{1}$1}, {10$\bar{1}$2} and {10$\bar{1}$3} surfaces will furthermore be referred to by their l index, with respect to standard {$hjkl$} nomenclature (as described in Figure 8.2).

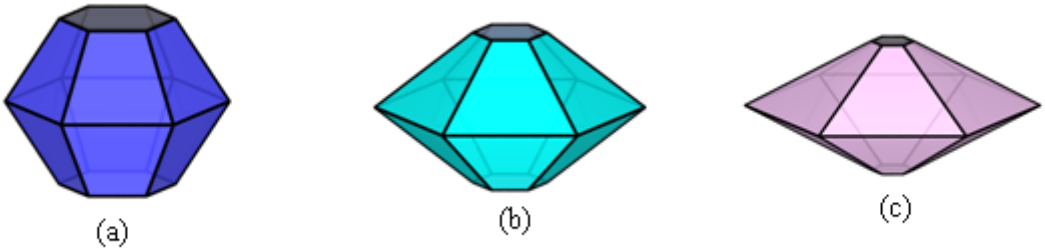

Figure 8.2 – WZ shapes formed from the {10$\bar{1}$1}, (10$\bar{1}$2}, {10$\bar{1}$3} and {0002) surfaces. Irrespective of *D, T, P* and surface termination, each shape can be described completely using only the shape parameters *l* and *x''*, such as (a) *l*=1, *x''*=0.5; (b) *l*=2, *x''*=0.35; and (c) *l*=3, *x''*=0.2.

To determine equilibrium shapes as a function of *D*, *P*, and *T*, expressions for *q* and f_i in Eq 3.12 must contain variables for the discrete dependence on the surface orientations of the pyramidal facets (represented by the *l* index, as described above) and continuous dependence on the degree of truncation of the apex of these facets in the <0001> directions (see Appendix B). In this way the morphology space can be thoroughly surveyed using a continuous method. The truncation factor was optimised for each *l* in order to find the exact shape which minimises the free energy with respect to *D, T* and *P*.

8.3 Results and discussion

8.3.1 Shape modelling

Surface energies were calculated according to Eq 3.18 and are shown in Figure 8.3 for *T* = 300 K. As seen in Figure 8.3, the surface energies of Zn-terminated surfaces are proportional and the S-terminated inversely proportional to ln*P*(S). From Eqs 3.18 and 3.19 it is evident that varying the temperature will alter the range over which ln*P*(S) is defined, however the surface energies themselves across this range are independent of *T*.

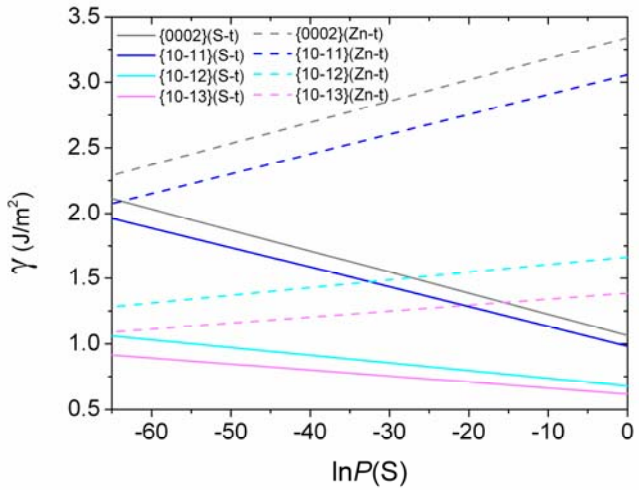

Figure 8.3 – Specific energies of formation for S- and Zn-terminated surfaces with respect to the partial pressure of sulphur at 300 K.

Using these surface energies in Eq 3.12, the equilibrium shapes were established for S-terminated and Zn-terminated surfaces. This was perfromed over a broad range of thermodynamic conditions, by sampling <*D,T,P*> space at a set of distant points. The <*D,T,P*> points were defined from combinations of *D*=5 nm and 50 nm, *T*=300 K, 600 K and 900 K and ln*P*(S)=0.0, -22, -33 and -65, with respect to the limits of ln*P*(S) set by Eq 3.19. The shape variable *x* was optimised for each combination of facet orientation *l* and species termination at every point in <*D,T,P*> space. The equilibrium shape at each point was a mixture of S-terminated $\{10\bar{1}2\}$ and $\{10\bar{1}3\}$ faceted structures with *x*=0.0 for all <*D,T,P*> (Figure 8.4(a) and (b)).

The effect of changes in temperature and pressure on morphology was established through a comparison of the free energies of equilibrium and non-equilibrium shapes over the <*D,T,P*> space defined above (Figure 8.5). Pressure was found to have greater effect, however temperature was also found to be significant. Therefore, while both thermodynamic variables are considered to be important in determining morphology, *D* and *P* dependence was the primary focus of proceeding multi-dimensional analysis in <*D,T,P*> space.

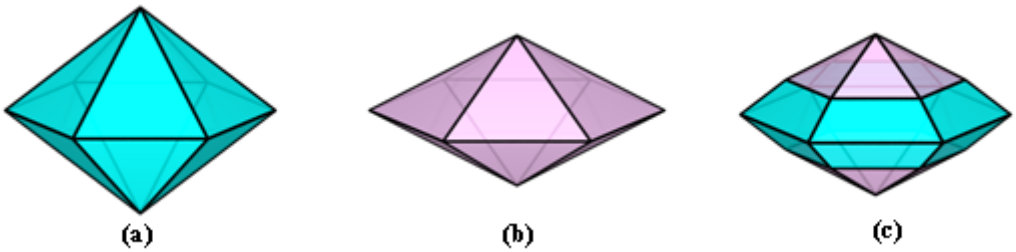

Figure 8.4 – The equilibrium shapes located over the region of <*D*,*T*,*P*> defined in the main text, formed from (a) {10$\bar{1}$2} and (b) {10$\bar{1}$3} facets and (c) combined at a ratio of 0.4/0.6 (*x'''*=0.8).

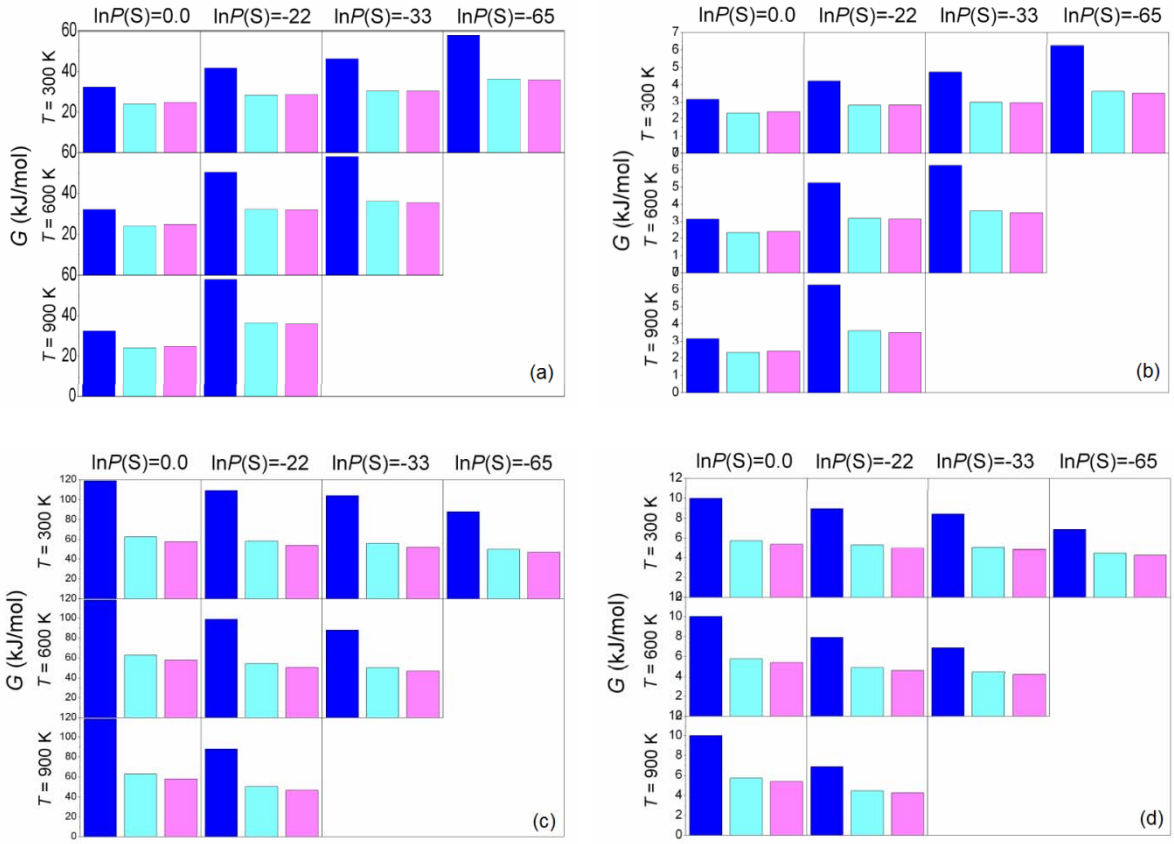

Figure 8.5 – An initial sample of <*D,T,P*> space, taken by comparing the total free energies belonging to 5 nm (a and c) and 50 nm (b and d) shapes with S-terminated (a & b) and Zn-terminated (c & d) surfaces at nine different temperature/pressure points. Shapes were formed from {10$\bar{1}$1} and {0002}(blue), {10$\bar{1}$2}(cyan) and {10$\bar{1}$3}(pink) surfaces. Truncation in the <0001> direction was optimised for each shape at each <*T,P*> point.

To assess the influence of thermodynamics in shape selection and surface termination, the facet orientations l and the apex truncation x were varied separately and the free energies plotted with respect to ln$P$(S) for 5 nm S- and Zn-terminated shapes at T = 900 K, the results of which are shown in Figure 8.6. These results show a strong thermodynamic preference for S-terminated {10$\bar{1}$2} and {10$\bar{1}$3} facets with little or no apex truncation in the <0001> directions. However, no significant preference for either S-terminated shape is apparent and only minor preference for {10$\bar{1}$3} when terminated by Zn. In contrast, the {10$\bar{1}$1} surface is found to be more stable when terminated by sulphur under S-rich conditions.

Zn-terminated surfaces are not thermodynamically preferred under any conditions; however Zn-rich conditions are significantly preferable over S-rich if suitable kinetic processes are put to use. Preference for formation of the {0002} facets (as a result of <0001> truncation) is greatest when {10$\bar{1}$1} facets are present; however this is not to say that this shape gives the most stable {0002} surface. The formation of {0002} on more stable shapes with higher index surfaces is also favourable, although the proportion of {0002} favoured is less (x''=0.2 for l=2 and l=3 as opposed to x''=0.5 for l=1). In general, no significant preference was found for truncation in the range $0.0 \leq x'' \leq 0.2$ for l = 2 and l = 3.

The similarity in energies of the l=2 and l=3 bipyramids suggests that additional stability could be gained (via a reduction of the surface-to-volume ratio q) by combining the {10$\bar{1}$2} and {10$\bar{1}$3} surfaces within a single morphology. This multi-faceted bipyramid structure (l=2|3) was modelled using an additional shape variable x''', which represents the truncation of {10$\bar{1}$2} surfaces in the <10$\bar{1}$3> directions. This variable spans the range $0 \leq x''' \leq 1$, where 0 is no truncation and 1 is complete (effectively Figure 8.4(a) and (b), respectively).

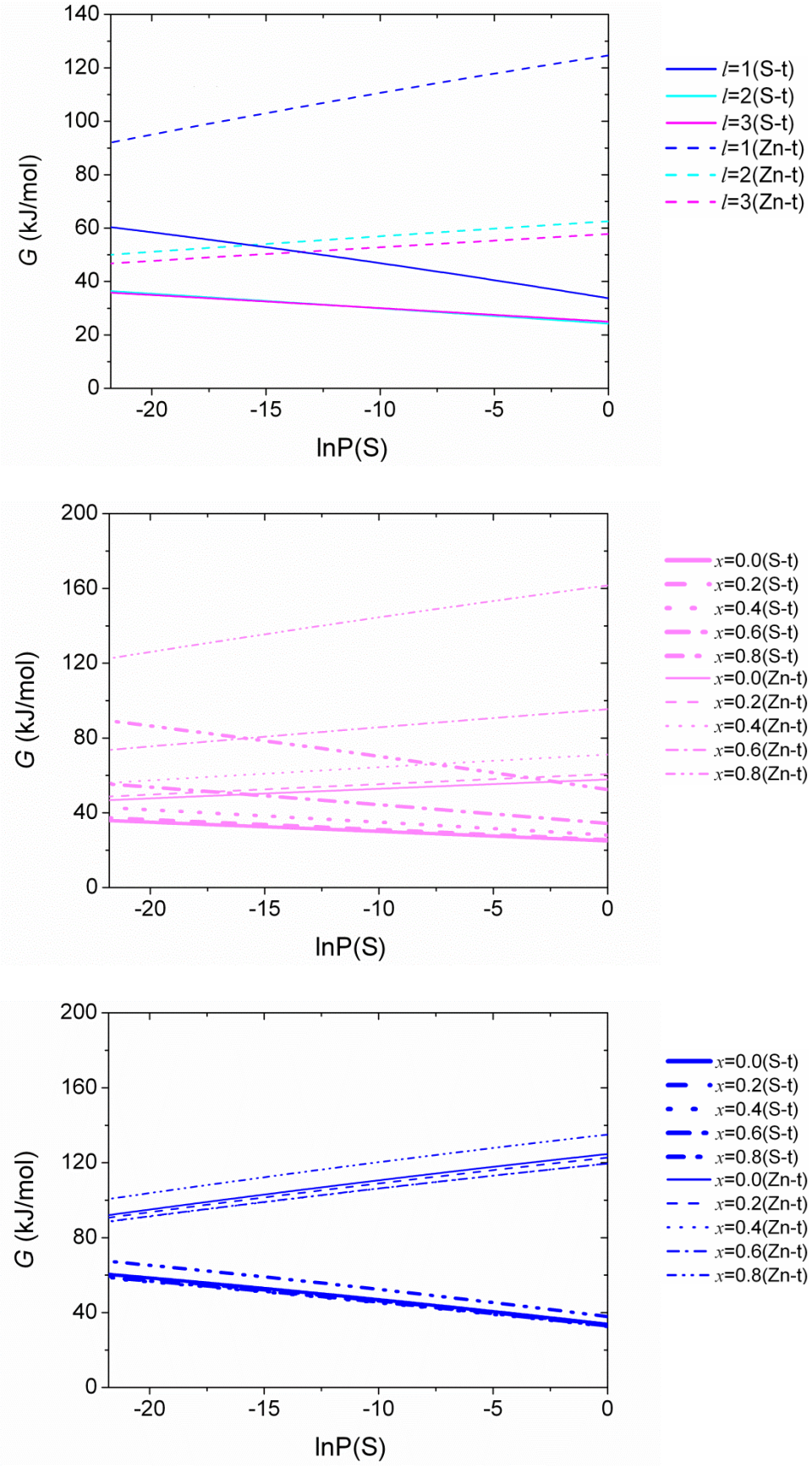

Figure 8.6 – The influence of pressure on surface termination and shape selection is established by comparing the free energies of for (a) l=1, 2 and 3 with x=0; (b) and (c) l=3 and l=1, respectively with x varied as shown.

Using the same method applied to the simple bipyramids, the values of x'' and x''' for l=2|3 were self-consistently optimised with respect to temperature, pressure, size and termination. Truncation in the <0002> direction is now limted to the $\{10\bar{1}3\}$ surfaces, as any truncation of the $\{10\bar{1}2\}$ surfaces in this direction forms a shape which is described by l=2. An optimum value of x''=0.0 was found under all conditions. Optimum values of x''' with respect to pressure were $0.64<x'<0.79$ for S-terminated and $0.81<x'''<0.88$ for Zn-terminated shapes (where low pressure favoured high x''' for S-terminated and *vice-versa* for Zn-terminated). Subsequently, optimum values with respect to temperature were within these ranges at all pressures tested. Truncation in the range $0\leq x'''\leq 1$ revealed only slight thermodynamic preference for the optimum values, while no significant preference was found within the range $0.64<x'''<0.88$. An example of the l=2|3 shape (with x''' =0.8) is shown in Figure7.4(c).

8.3.2 Phase transformations between WZ and ZB

The study of WZ/ZB phase transformations involved four WZ shapes and three ZB shapes: the WZ l=1, x''=0.5 (Figure 8.2(a)); l=2, x''=0.0 (Figure 8.4(a)); l=3, x''=0.0 (Figure 8.4(b)) and l=2|3, x''=0.0, x'''=0.8 (Figure 8.4(c)); and the ZB shapes enclosed entirely by the polar {111}, {200} and {311} surfaces (Figure 8.7), forming respectively, the octahedron (O), regular hexahedron or cube (C) and deltoidal icositetrahedron (DI).

In order to appropriately compare the free energies of these shapes and determine their relative stabilities their free energies with respect to surface area per mole were compared under the set of conditions described below. The expression for surface area per mole includes the surface-to-volume ratio q, and therefore captures both the size- and shape-dependence of the systems. From a comparison of the free energies of these shapes a number of possible phase transformation sizes were identified, depending on the temperature, sulphur supersaturation and the specific shape being considered within each phase.

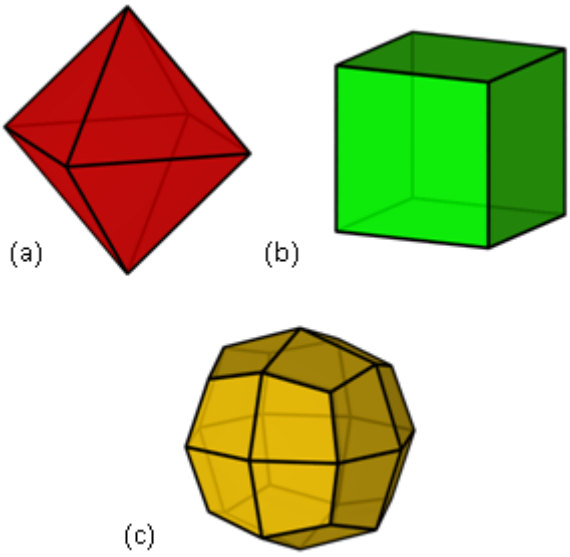

Figure 8.7 – ZB shapes enclosed by the {111}, {200} and {311} facets, forming the (a) octahedron (O), (b) regular hexahedron or cube (C) and (c) deltoidal icositetrahedron (DI). The free energies of these were compared with WZ shapes to predict possible WZ/ZB phase transformations.

Free energies were plotted as a function of surface area per mole under the following set of conditions (labelled $\mathscr{A}$ to $\mathscr{F}$ for further reference), with the estimated phase transformation sizes indicated in square brackets (identified as the largest size at which a free energy crossover between a ZB and WZ shape occurs, being the ZB (DI) and WZ l=3 morphologies in each case, such that the WZ phase is favoured *below* this size):

$\mathscr{A}$. S-terminated surfaces; ln$P$(S) = 0.0; 900 K; [35 nm]

$\mathscr{B}$. Zn-terminated surfaces; ln$P$(S) = 0.0; 900 K; [255 nm]

$\mathscr{C}$. S-terminated surfaces; ln$P$(S) = -22; 900 K; [110 nm]

$\mathscr{D}$. Zn-terminated surfaces; ln$P$(S) = -22; 900 K; [175 nm]

$\mathscr{E}$. S-terminated surfaces; ln$P$(S) = -22; 300 K;[62 nm]

$\mathscr{F}$. Zn-terminated surfaces; ln$P$(S) = -22; 300 K; [230 nm]

These are representative of high temperature synthesis conditions ($\mathscr{A}$ to $\mathscr{D}$) and room temperature ($\mathscr{E}$ and $\mathscr{F}$). Shape-dependent phase transformation sizes were identified from

crossovers in the free energies with respect to surface area per mole. Surface terminating species and pressure were most significant in determining the phase transformation sizes and the degree of thermodynamic preference (particularly at small sizes). Figure 8.8 indicates how shape-dependent phase transformation sizes were identified for S-terminated morphologies at 900 K and ln$P$(S) = 0.0 (*A*). Phase transformations were identified at sizes ranging from 255 nm to 14 nm; however, the degree of thermodynamic *preference* for each phase, and shapes within these phases, varied significantly. These relative thermodynamic stabilities revealed regions which are more conducive to the formation of non-equilibrium shapes and conditions for synthesised structures which will increase their broader thermodynamic stability.

For example, for S-terminated surfaces under S-rich conditions at 900 K (*A*), a phase transformation occurred at ~35 nm between ZB (DI) and WZ (l = 3), such that the WZ shape is favoured below this size (Figure 8.8). A second crossover between ZB (DI) and WZ (l = 2) occurs at ~14 nm. The crossover between ZB (DI) and WZ (l=2|3, x''' = 0.8)occurs between these sizes at 22 nm. These WZ shapes are also favoured over the ZB (O) and (C) shapes above 100 nm; however it was noted that the preference for these WZ shapes, in relation to the ZB (C), decreased significantly below ~ 6 nm, as seen in Figure 8.9. At ~3nm there is very only minor preference for the WZ shapes over the ZB (C).

Under Zn-rich conditions, thermodynamic preference for the l=2, l=3 and l=2|3 WZ shapes increases *at all sizes*, as can be seen in Figure 8.10(b) for S-terminated surfaces under Zn-rich conditions at 900 K (*C*). A far greater increase in preference for these WZ shapes, particularly at small sizes, was found for Zn-terminated surfaces under all pressure and temperature conditions (*B*, *D* and *F*), as seen for example in Figure 8.10(a) and (c)at 900 K for S-rich conditions (*B*) and Zn-rich conditions (*D*), respectively.

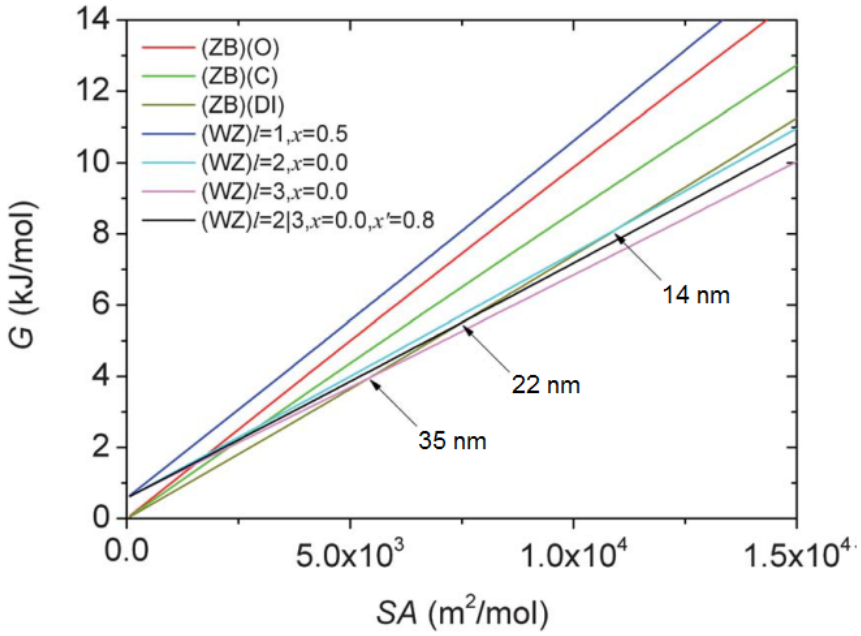

Figure 8.8 – Free energies of S-terminated WZ and ZB shapes under S-rich conditions (ln$P$(S)=0.0) at 900K ($\mathscr{A}$), indicating shape-dependent phase transformation sizes.

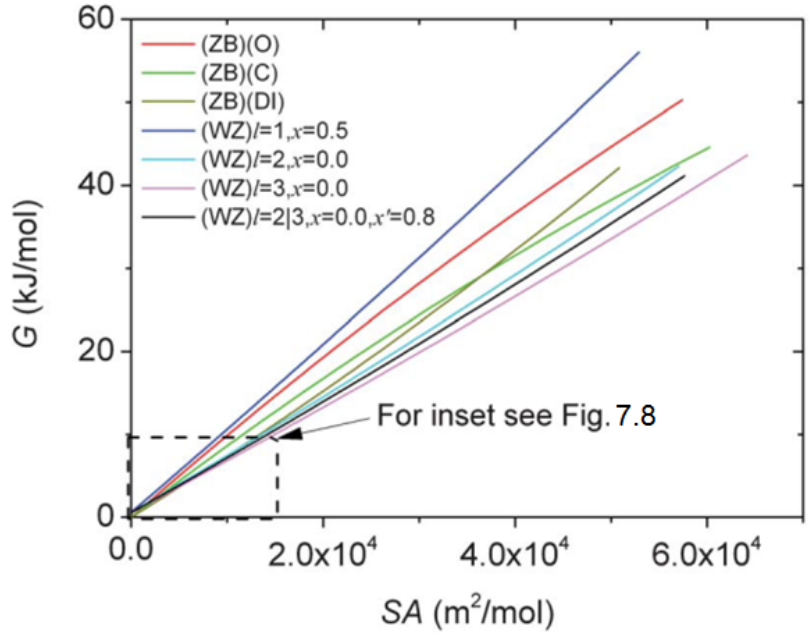

Figure 8.9 – Total free energies of S-terminated WZ and ZB shapes under S-rich conditions at 900 K (A), showing WZ shapes favoured across a large size range. A significant decrease in WZ preference over the ZB (C) shape occurs below ~6 nm (corresponding to a surface area per mole of ~3.5x10^4 m^{2}mol^{-1}). Inset is shown in Figure 8.8.

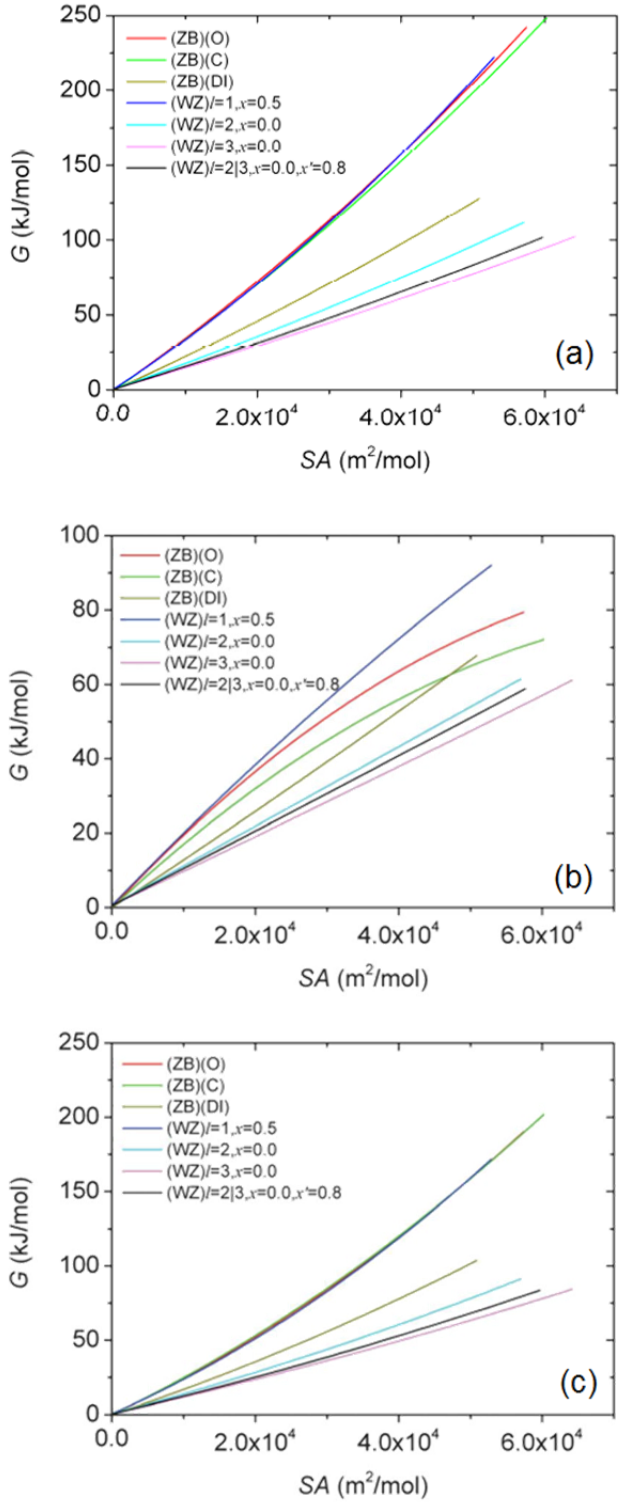

Figure 8.10 – Free energy as a function of surface area per mole at 900 K under (a) S-rich conditions for Zn-terminated surfaces (ℬ) and under Zn-rich conditions for (b) S-terminated (𝒞) and (c) Zn-terminated (𝒟) surfaces. The higher index WZ shapes are thermodynamically favoured at all sizes. In comparison to Figure 8.9 there is also an increased preference for these shapes, particularly at small sizes and for Zn-terminated surfaces.

Zn-terminated surfaces place the *l*=1 shape with {0002} facets in thermodynamic coexistence with respect to the ZB (O) and (C) shapes (as in Figure 8.10(b) for example); however they are most unstable under these conditions with respect to the remaining ZB and WZ shapes. In general, Zn-rich conditions are more conducive to the formation of WZ nanoparticles with further preference given Zn-terminated surfaces (Figures 8.9 and 8.10); however S-terminated WZ shapes formed under Zn-rich conditions are at greater risk of undergoing a phase transformation to ZB, especially at small sizes, under altered pressure conditions.

Truncation of WZ shapes in the <0001> direction can always be expected. Note that {0002} facets are also thermodynamically favourable (though in smaller proportions) when formed from truncation of the $\{10\bar{1}2\}$ and $\{10\bar{1}3\}$ facets. Under Zn-rich conditions at 300 K the ZB to WZ phase transformations involving the ZB (DI) and WZ *l*=3 shapes occured at 63 nm for S-terminated (*E*) and 230 nm for Zn-terminated (*F*) surfaces (Figures 8.11 and 8.12).

8.4 Conclusions

Using shape-dependent, *ab initio* thermodynamic modelling the equilibrium shapes for polar WZ nanoparticles were determined as a function of size, temperature and the partial pressure of sulphur. The high index $\{10\bar{1}2\}$ and $\{10\bar{1}3\}$ facets were found to be highly favoured thermodynamically. Selection between these two surfaces is likely to be determined kinetically, with preference occuring for a shape combining the $\{10\bar{1}2\}$ and $\{10\bar{1}3\}$ surfaces to form a a multi-faceted bipyramidal morphology. A minor proportion of {0002} facets may be formed due to kinetic influences; however no thermodynamic advantage was found from reduction of the surface-to-volume ratio caused by truncating the pyramidal apexes in the <0001> directions.

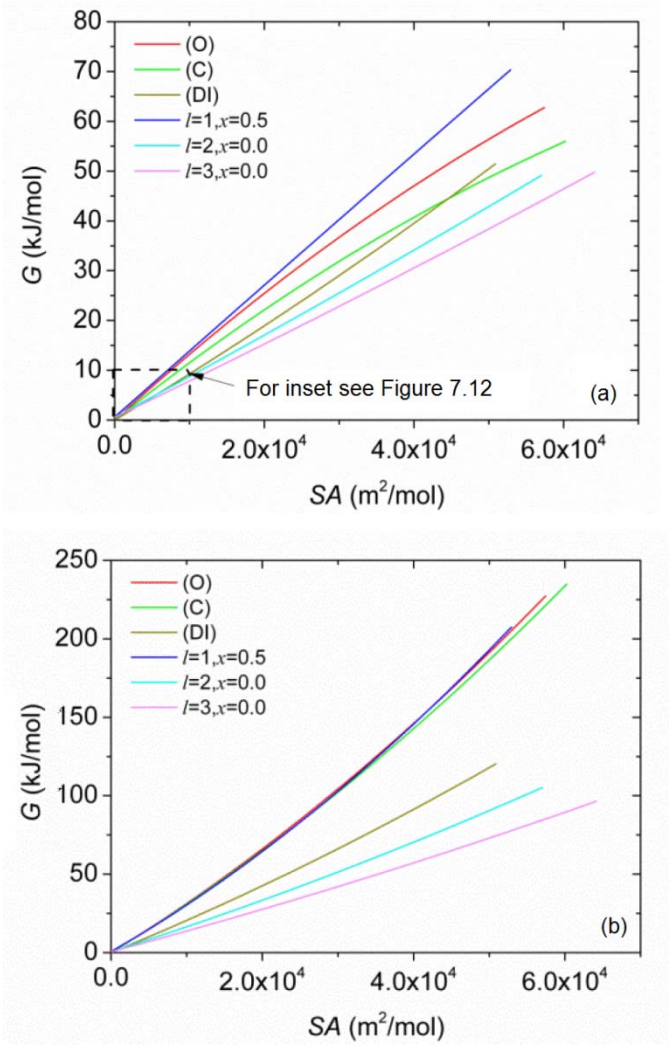

Figure 8.11 – Free energies at 300 K under Zn-rich conditions for (a) S-terminated (Ⓔ) and (b) Zn-terminated (Ⓕ) shapes.

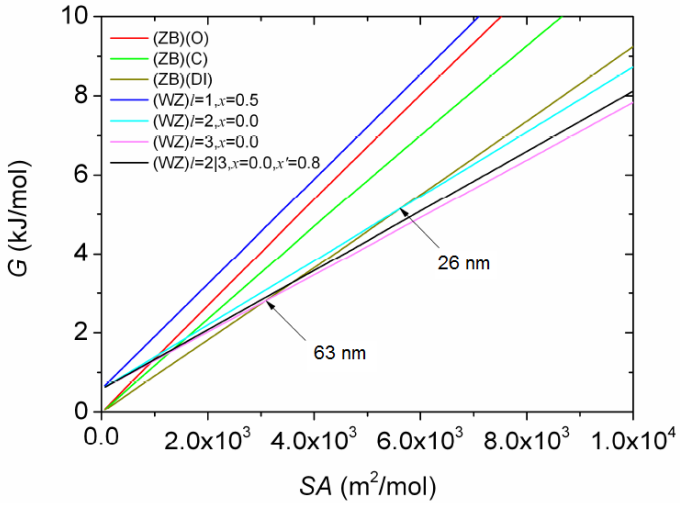

Figure 8.12 – Inset from Figure 8.11(a) showing energetic crossovers between S-terminated ZB and WZ shapes at 300 K under Zn-rich conditions (Ⓔ).

The free energies of ZB and WZ shapes were compared to establish possible phase transformation sizes and thermodynamic conditions most conducive to the formation of specific morphologies and their broader environmental stability. For the formation of ZB shapes S-terminated surfaces are preferable, particularly for the octahedral and cubic morphologies; while Zn-rich conditions increase longer term stability if suitable intervention from kinetic processes can be applied during synthesis. For Zn-terminated surfaces, octahedrons and cubes require very strong kinetic intervention if they are to be formed, particularly at small sizes where the thermodynamic incentive for formation of competing morphologies is greatest. However, if formed under these conditions, these shapes are expected to remain stable in a wide range of temperature/pressure conditions. S-rich conditions are most favourable for the formation of ZB shapes given S-terminated surfaces; however given suitable thermodynamic incentive a phase transformation to the WZ phase is more likely to occur once sulphur partial pressure or temperature decreases. Thermodynamically, WZ shapes are preferably formed with Zn-terminated surfaces and in this form are expected to remain stable up to and above 100 nm under broad temperature/pressure conditions. If S-terminated surfaces are required, the use of Zn-rich conditions could be critical during the early growth stage to avoid formation of ZB morphologies, as S-rich conditions provide at best slight preference for S-terminated WZ shapes. At sizes less than 35 nm WZ phase nanoparticles are generally expected to be most stable; however phase transformations can occur well above this size and depend sensitively on the chemical conditions at all sizes.

Chapter 9. Mixed Zinc Blende/Amorphous and Zinc Blende/Wurtzite Arrangements

9.1 Introduction

In Chapters 5 and 7 the equilibrium morphologies of zinc blende (ZB) nanoparticles were established as a function of size. In this chapter we study the thermodynamic stabilities of mixed ZB/wurtzite (WZ) and ZB/amorphous (AM) phases. The relative thermodynamic stabilities of these structures are presented in this chapter. This work was published in reference 167.

9.2 Mixed ZB/AM core/shell structures

9.2.1 Size-Dependent Crystallinity

In addition to morphological instability introduced by the presence of high energy facets, or kinetically grown shapes, ZnS may also undergo solid-solid phase transformation under ambient conditions. Zhang, Gilbert, Huang, Banfield and others observed reversible structural transformations in ZnS nanoparticles of ~3 nm in size at room temperature[44], induced by aggregation-disaggregation and absorption-desorption of methanol and water. It was therefore suggested that water decreases the surface free energy, and promotes crystallinity throughout the nanoparticles. These studies were complemented by classical MD simulations of the interaction between methanol and water and the surface S and Zn ions, which showed that the surfaces of nanoparticles in methanol undergo reconstruction that penetrates several atomic layers, leading to a crystalline core surrounded by a disordered shell (Figure 2.3). However, insufficient structures were sampled in this study to definitively attribute the emergence of the core-shell structure as a byproduct of surface chemical reactions, and it can not be ruled out that crystalline/amorphous core-shell structures are simply more energetically favourable at small sizes.

9.2.2 Theoretical and computational method

Depending upon the number of atomic layers participating in the amorphous shell a core-shell particle will consist of differing volumetic ratios of ZB and amorphous materials (see Figure 9.1), as well as a free amorphous surface and a ZB/amorphous interface, all of which scale with size. If the change in the surface and interfacial free energy provides the driving force for a change in degree of crystallinity, then it follows that that the various size-dependent free energies and energy differences (which is dominated by the surface energy term at small sizes) will also play an important role, irrespective of the chemical environment.

To investigate this issue, the same theoretical and computational method described in Chapter 5 was used to calculate the properties of an ZB/amorphous interface (see Figure 9.2), and, together with the AM surface energy reported in Chapter 5, was used to calculate the free energy of core-shell nanoparticles with different ZB/amorphous volumetric ratios (see Figures 9.1(a)-(e)). These were compared to low energy ZB structures over 3 nm in size along with a complete amorphous ZnS spherical nanoparticle (Figure 9.1(f)). The core-shell particles were modelled by subtracting the volume of the crystalline core from the centre of the amorphous sphere, and adding a ZB core enclosed by the {110} interfaces characterised by the interfacial energy. Each region retained the characteristic bulk modulus, bulk density and bulk formation energy.

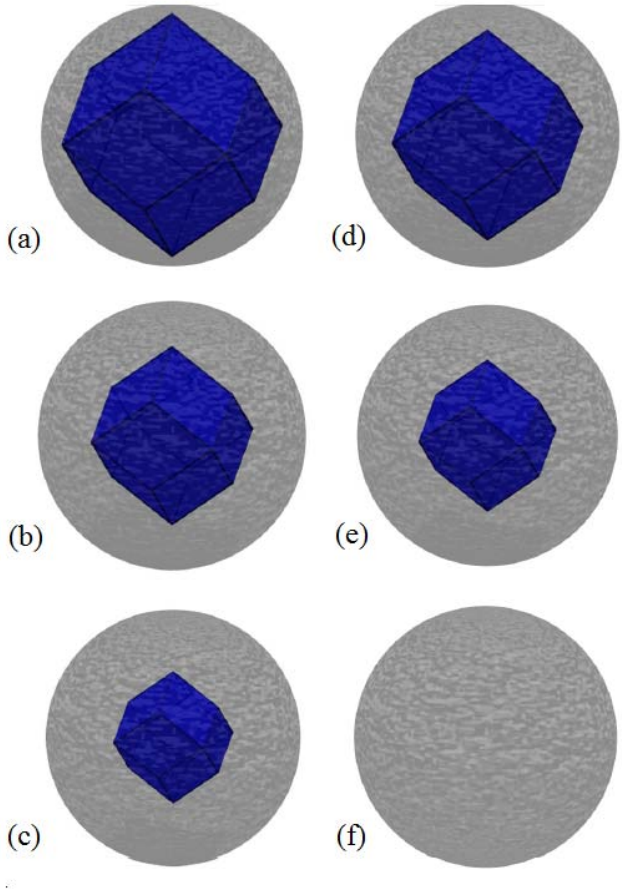

Figure 9.1 – The ZB crystalline/amorphous core-shell structures modelled in this chapter, with core/shell ratios by volume of (a) 82.0/18.0; (b) 57.6/42.4; (c) 38.6/61.4; (d) 24.3/75.7; (e) 14.1/85.9; and (f) the 100% amorphous ZnS as shown in Chapter 5.

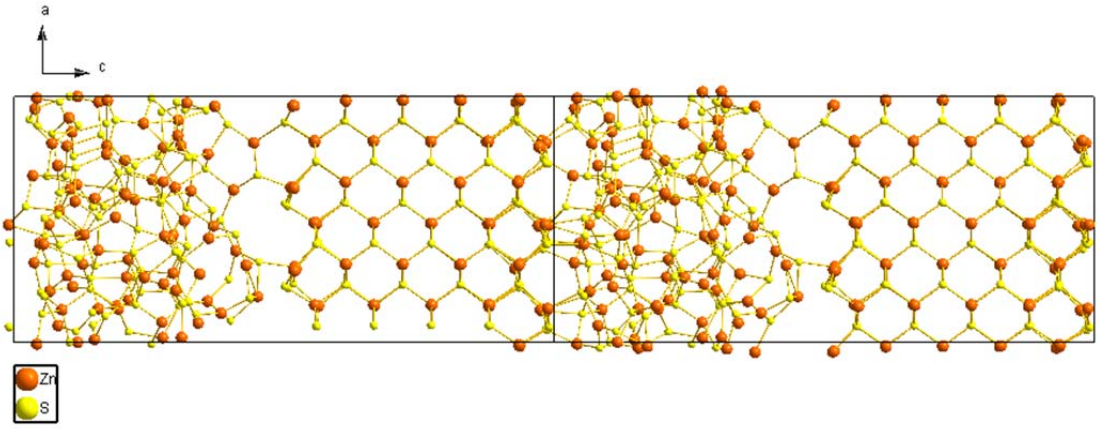

Figure 9.2 – Schematic representation of the combinded ZB/AM structure used to calculate the interfactial energy and stress for modelling ZB/AM core/shell structures.

The appropriate choices of the bulk free energy of formation, ΔG_f, for both the ZB and AM materials, was an important aspect of this analysis. In general, the free energy is the energy difference from reaction that may include a variety of reactants and products. The final value depends upon the temperature and the species participating in the chemical reaction, since some reactions are more favourable than others. For example, experimental values for the bulk ZB enthalpy of formation are -206.53 kJ/mol as measured by Deore and Navrotsky[131], between -21.87 and -105.45 kJ/mol by Daskalakis and Helz[173], and between -18.84 and -30.26 kJ/mol by Hayashi, Sugaki and Kitakaze[174]. For AM ZnS an experimental value for the bulk free energy of formation can vary between -33.52 and -62.87 kJ/mol, as shown by Gubeli and Marie[175]. In order to accurately compare the free energy difference between ZB and AM ZnS it is necessary to ensure that the same reaction is considered, but this is problematic since a single reaction rarely produces two different ZnS products. None of these values originate from identical reactions. Therefore, we have calculated these value by subtracting the energy per ion of Zn in the hexagonal phase and S in the S_8 dimer from the average Zn-S bond energy determined from our ZB and AM supercells in Chapter 5, so that they are both calculated using the same computational method and reaction, $(ZnS)_8 = (Zn)_8 + S_8$. This gave a value of -166.28 kJ/mol for bulk ZB ZnS and -116.47 kJ/mol for bulk AM ZnS, with a free energy difference of 49.78 kJ/mol.

9.2.3 Results and discussion

The surface free energy for the interface was calculated to be 0.06 J/m^2. Using this value and the bulk properties outlined above, the total free energy for the crystalline/amorphous core-shell structures were calculated according to Eq 3.12. These were compared to four low energy ZB shapes reported in Chapter 5 (which now include the bulk free energy of formation) and a spherical AM nanoparticle. These results (shown as a function of molar

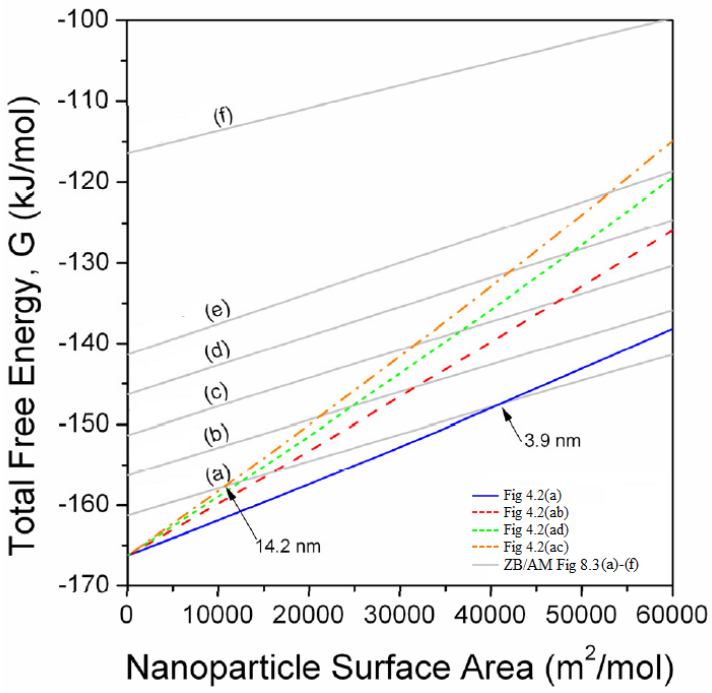

Figure 9.3 – Relative free energy of formation of low energy shapes of zinc blende structured zinc sulphide nanoparticles (as defined in Figure 5.2), as a function of surface area, compared to the free energy of formation of a core-shell crystalline/amorphous ZnS nanoaprticle (as defined in Figure 9.1(a)-(e)) and an amorphous ZnS sphere (Figure 9.1(f)). The cross-overs indicate a size dependent phase transformation given a suitable kinetic perturbation.

surface area in Figure 9.3) indicated that a size-dependent phase transformation may be expected in the range 3.9 nm to 14.2 nm, depending upon the degree of morphological dispersion and core-shell ratio.

For example, the second lowest energy shape (Figure 5.2(ab)) exhibited a crossing with the thinnest shell structure (Figure 9.1(a)) at 8.4 nm, and at smaller sizes it was observed that thicker shells are more favourable than a purely ZB structure with this morphology. This suggests that, at small sizes, the surfaces of higher energy shapes will more readily amorphize, even though they are still dominted by low energy {110} facets. These results are in agreement with experimental observations of ZnS nanoparticles reported in the literature[44] and clearly show how nanoparticle shape and core-structure are intrinsically linked. Over 14.2 nm the core-shell structure was not found to be stable, irrespective of the core-shell ratio or crystal habit, in agreement with macroscopic observations[190].

The higher energy shapes (not shown in Figure 9.3) are not expected to be stable at any size, since although a transformation from amorphous to crystalline is expected between ~15 nm to 60 nm in size, any driving force sufficient to overcome the kinetic barrier will undoubtedly be equally sufficient to invoke a simultaneous morphological transformation to a lower energy ZB shape. Therefore, in general, size-dependent transformations between zinc blende and crystalline/amorphous core-shell nanoparticles may only be controlled (or avoided) if sensitive control over the shapes can be achieved. These results also demonstrate that these phase transformations are highly efficient, indicating a low kinetic transformation barrier and dominant thermodynamic influences. This was the first time this technique has been used to model amorphous nanoparticles, and to identify the size-dependent changes in crystallinity.

9.3 ZB and mixed ZB/WZ tetrapods

9.3.1 Competing tetrapod morphologies

As discussed in previous chapters, an understanding of the relative free energies of nanomorphologies, with respect to relevant thermodynamic variables, can provide insight into the post-synthesis stability of engineered nanostructures and also assist in guiding experimental conditions to meet specific aims. In regard to the latter, as well as assessing the equilibrium morphologies, benefit can be gained from examining the thermodynamic stability of non-equilibrium structures, with specific attention to those which have been the focus of pre-existing experimental studies, as such structures are often intentionally formed with specific applications in mind.

For example, following the successful novel formation of tetrapod-structured CdSe[191], considerable attention has been given to synthesizing similar structures in other II-VI type

materials, such as ZnS[192-194], and on understanding the growth mechanisms so as to build and improve on the techniques used for fabricating this unusual morphology. Owing to the superior field emission and mechanical properties of this structure in ZnS, applications are targeted to novel electric and optoelectronic devices such as field emitters and atomic force microscope probes.

Presently in literature, there are two competing ZB tetrapod morphologies, each giving rise to two distinctly different tetrapod crystalline forms: one mono-crystalline in ZB, the other polycrystalline with a ZB core and WZ 'legs' (as shown for example in Figures 9.3 and 9.2). The mono-crystalline form possesses a tetrahedral core, while the core of the poly-crystalline tetrapod is octahedral[192-194]. One method for the fabrication of ZnS tetrapods involves Zn and S powders at 750^{o}C and 400^{o}C, respectively, deposited in the presence of an inert gas onto a silicon substrate with varying levels of Mn impurity concentrations (Mn was reported to have no effect on final tetrapod morphology). From TEM and HRTEM sample at different times in the fabrication process, the authors conclude a two-step growth process commencing with the formation of a cubic phase octahedron shaped nucleus and growth of four wurtzite legs, with uniform diameters ranging from 80-150 nm in the cubic <111> / hexagonal <0001> direction.

A separate study reacted Zn vapour with S vapour at 1000^{o}C with deposition on a stainless steel network. The tetrahedral core was measured at ~65 nm. HRTEM and SAED patterns of the core revealed a single-crystalline cubic phase. The authors conclude a two-step growth process, commencing with formation of a ZB, octahedral nucleus, followed by the growth of WZ legs in the <0001> direction on the Zn-terminated, {111} surfaces (although the species termination of core surfaces is implied from crystal symmetry and not confirmed experimentally).

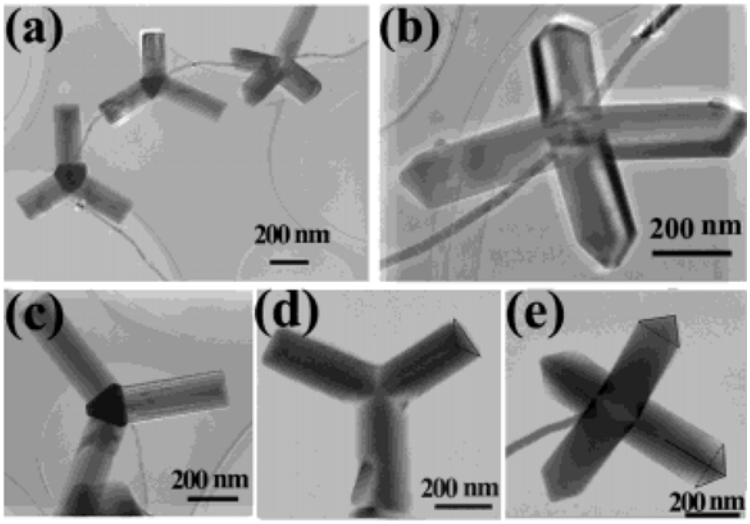

Figure 9.4 – Images of nanocable-aligned ZnS tetrapods. (a) Aligned ZnS tetrapods. (b) Nanocable passing through the centre of the tetrapod. (c) Tetrapod image viewed along the [111] direction; (d) viewed along the [$\bar{1}\,\bar{1}\,\bar{1}$] direction; (e) viewed along the [100] direction. Reprinted with permission from reference 194. Copyright (2003) American Chemical Society.

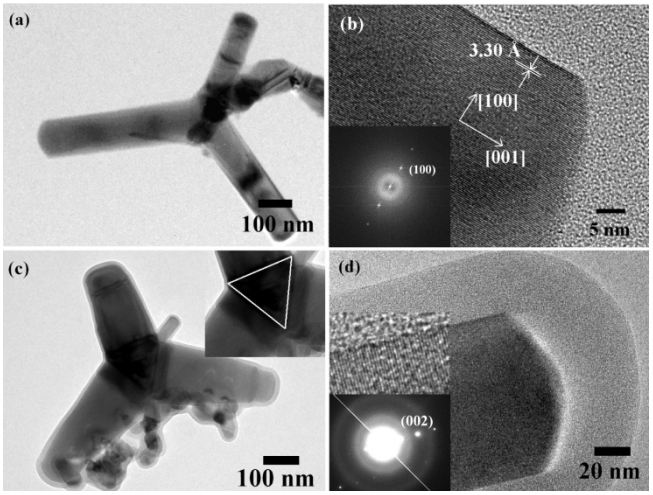

Figure 9.5 – (a) TEM image of a single undoped ZnS tetrapod. (b) HRTEM image of one leg of the ZnS tetrapod along with the FFT pattern in the inset. (c) TEM image of a single Mn-doped core/shell nanotetrapod. Magnified image in the inset shows the triangular cross-section of the leg. (d) HRTEM image of the leg of the ZnS:Mn/Si tetrapod showing crystalline ZnS:Mn core surrounded by an amorphous Si shell. Inset shows the SAED pattern and a selected magnified portion of the crystalline core. Reprinted with permission from reference 193. Copyright (2009) American Chemical Society.

A third study shows a competing trend for core morphology and leg phase. Following the formation of ZnS/C core/shell nanocables, ZnS powder was heated to 1100^{o}C and single-crystalline ZB tetrapod structures formed along the nanocable lengths. Through the use of HRTEM and ED patterns a growth process was described with reference to the crystallographic characteristics of ZnS, which has a tetrahedral bonding arrangement in the ZnS_4 base units. According to the authors, bonding at the corners of ZnS_4 tetrahedra give rise to tetrahedral shaped cores which nucleate growth of the cubic phase legs in four <111> directions.

9.3.2 Theoretical and computational method

Ab initio thermodynamic modelling of the octahedron, tetrahedron and truncated tetrahedron (an intermediate shape between octahedron and tetrahedron), repreenting three core morphologies with {111} facets, were modelled at 1000°C and ln$P$(S)=-19.6, -10.0 and 0.0 according to Eq 3.12. The equations for the surface-to-volume ratio and the facet weighting factor required to model the tetrahedron and truncated tetrahedron are given in Table 9.1.

9.3.3 Results and discussion

The results of modelling of the octahedron, tetrahedron and truncated tetrahedron can be seen in Figures 9.6 and 9.7. Figure 9.6 reveals the thermodynamic preference at all sizes for the octahedron shape in both S- and Zn-terminated surfaces. However, the relative degree of favourability is dependent on both size and sulphur levels. This dependence is revealed more clearly in Figure 9.7, where the relative free energies of the octahedron and the tetrahedron are plotted against surface area per mole. This relationship indicates that the thermodynamic preference for the octahedron morphology is greatest under zinc-rich conditions and at smaller sizes. This suggests that sulphur-rich conditions will favour the engineering of pure ZB, tetrahedron nucleated structures and that this condition is most critical in the early nucleation stage.

Table 9.1 – Equations for calculating the surface-to-volume ratio q and weighting factor f_i of the tetrahedron and truncated tetrahedron shapes.

Shape	q	f_i
Tetrahedron	$\frac{12\sqrt{3}}{\sqrt{2}}\left(\frac{12V}{\sqrt{2}}\right)^{-\frac{1}{3}}$	$f_{111}=1$
Truncated Tetrahedron	$\frac{84\sqrt{3}}{23\sqrt{2}}\left(\frac{12V}{23\sqrt{2}}\right)^{-\frac{1}{3}}$	$f_{111}=1$

9.4 Conclusions

Nanomorphology prediction remains one of the most coveted but complex aims of nanotechnology today, one that will facilitate the design of nanomaterials in a way that is not currently available. However, these results highlight how creating designer morphologies involves more than just controlling the shape, we must also pay attention to consequential structural instabilities, such as changes in crystallinity. Although some desirable sizes and shapes may deliver superior properties, they may not be sufficiently stable to ensure this benefit is maintained long term. In this chapter it was shown, using first principles computer simulations and analytical modelling, that the shape of zinc blende ZnS nanoparticles and the core-shell structure and mixing ratio of crystalline/amorphous particles has an important impact on the thermodynamic stability of this nanomaterial.

Contrasting experimental studies on ZnS tetrapods were examined, where competing octahedron and tetrahedron core morphologies have been reported. It was found that the octahedron morphology will be thermodynamically preferred in the size range 3–33 nm at T=1000^{o}C, irrespective of sulphur concentrations. However, a tetrahedron core can gain stability when S-rich conditions are applied. This dependence on the sulphur concentration is most critical when particle sizes are small, as the thermodynamic preference for the octahedron shape is highest for small nanoparticles in Zn-rich environments. If a tetrahedral

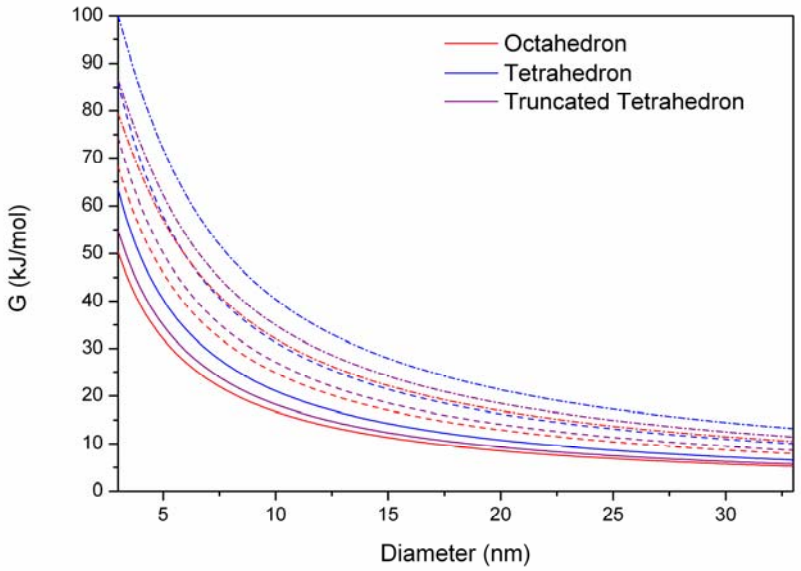

(a)

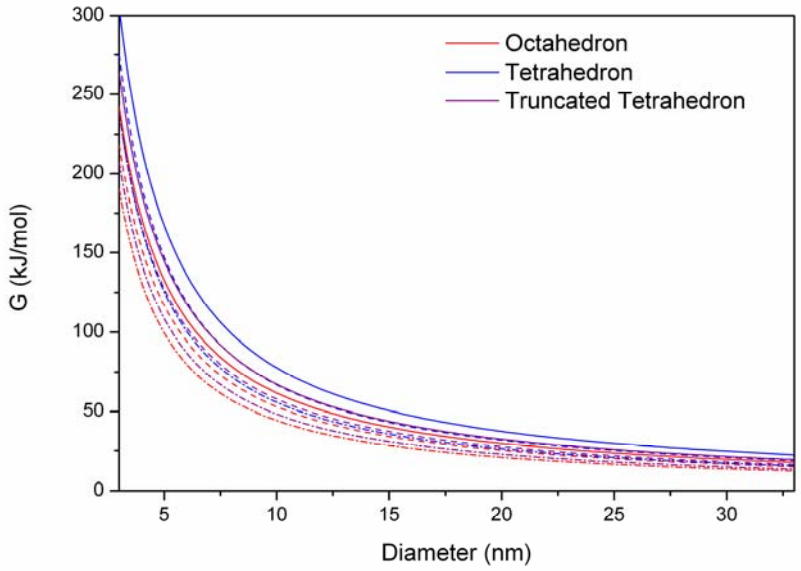

(b)

Figure 9.6 – Octahedron, tetrahedron and truncated tetrahedron free energies in red, blue and purple, respectively, as a functions of size with (a) S-terminated and (b) Zn-terminated {111} surfaces at 1000°C and ln*P*(S)=0.0(——), -10(- - -) and -19.6(-·-·-).

core can be maintained to large sizes (under S-rich conditions) then pure ZB tetrapods may be more easily obtained.

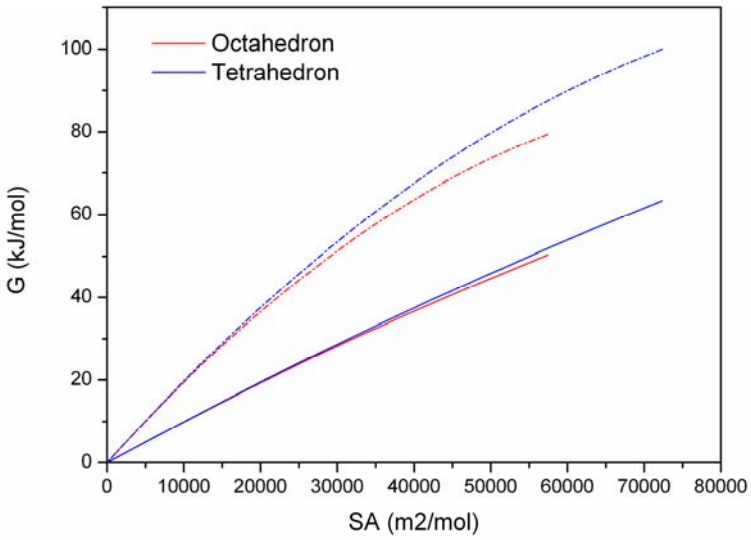

Figure 9.7 – Free energy as a function of surface area (SA) per mole for the (O) and (T) shapes at 1000°C and ln*P*(S)= 0.0(▬) and -19.6(▬ · ▬).

Chapter 10. Summary and Conclusions

Through analysis of existing experimental, computational and theoretical studies, it was shown how the exact relationship between structure and thermodynamic states of ZnS nanoparticles remained poorly understood. This was highlighted as being of significant concern, since the utility of this material is derived from its structure-property relationships (as is generally the case for nanomaterials). As a consequence, serious risks (including elevated toxicities and reduced efficiencies) associated with phase transformations (which are known to occur under a wide range of thermodynamic conditions) threatened a broad range of applications of this material. As stated in Chapter 1, harnessing the utility of this nanomaterial and minimising the associated risks requires a robust assessment of relative morphological stabilities. This body of work constitutes a means by which to predict the phase and shape of ZnS nanoparticles. This was achieved by mapping the equilibrium morphologies and identifying thermodynamic phase transformations points as a function of size, temperature and pressure (being the dominant thermodynamic variables affecting nanoparticle stability).

To accomplish these aims, *ab initio* density functional theory (DFT) calculations of ZnS surfaces were used to determine the surface energies and stresses of surface planes found in experimental XRD experiments of ZnS nanoparticles. These were used to determine the relative stabilities of various nanoparticle shapes through the use of a shape-dependent model based on the Gibbs free energy of a nanoparticle.

Since a number of approaches to DFT exist, the most appropriate method for ZnS was determined through systematic calculations and comparison with known experimental values of the mechanical and energetic properties of bulk ZnS[160]. This method was further employed for calculations of surface energies and stresses and also serves as a useful reference for other *ab initio* studies of ZnS.

The equilibrium shapes of ZnS nanoparticles in the zinc blende (ZB), wurtzite (WZ) and amorphous (AM) phases were determined as a function of size[167,180]. In the ZB phase, the equilibrium morphology was found to be dominated by a non-polar surface. Since polar surfaces are required for many applications (most noteably bio-technology and catalysis related), these results have significant implications for the agglomeration behaviour and stability of functionalised ZB ZnS nanoparticles[167]. For example, while low energy ZB morphologies with polar and non-polar surfaces were found to be stable with respect to the AM phase at all sizes, it was found that the introduction of polar facets encourages a phase transformation to the WZ phase at small sizes[180]. The exact size at which the transformation occurs depends on the shape of the ZB nanoparticle (specifically, the polar surface type and fraction of total surface area). Similarly, the aspect ratio was found to have a significant influence over the stability of the WZ phase. The optimum aspect ratios and equilibrium shapes for WZ nanoparticles were determined as a functions of size, showing a preference for elongated (nanorod-like) structures and a significantly increased thermodynamic preference for the equilibrium aspect ratio at smaller basal plane diameters. Size, shape and phase were shown to be intrinsically linked, and the shape-dependent ZB/WZ phase transformation size in the space defined by the important geometric features was mapped[180]. These results show how shape is one of the critical aspects of ZnS nanoparticles which determine phase. Encouraging or suppressing the formation of specific surfaces or growth in specific directions can therefore become the driving force behind phase changes, as opposed to conventional wisdom which regards this as purely a size-related matter.

Ab initio thermodynamic techniques were employed to investigate the effect of temperature and pressure on phase where nanoparticles composed of entirely polar surfaces are concerned[187,189]. This revealed the relative significance of these thermodynamic variables, as well as surface terminations, in determining the equilibrium morphology and

phase transformation sizes. The equilibrium morphologies for ZB and WZ shapes were established and were found to vary significantly with temperature, pressure or surface termination, while thermodynamic regions in which kinetic processes could better favour the formation of non-equilibrium shapes within each phase were identified. The influence of temperature and pressure over ZB/WZ phase transformation sizes was described, with respect to equilibrium shapes within the respective phases, while thermodynamic conditions most conducive to the formation and broader environmental stability of specific phases were identified, specifying where the use of kinetic processes would be most appropriate for achieving these aims. These results provide significant insight into the kinds of experimental and post-synthesis environmental conditions that will encourage the formation and long-term stability of specific phases.

Consideration was given to mixed ZB/AM and ZB/WZ structures which have been observed experimentally. Thermodynamic analysis of ZB/AM core/shell structures revealed a thermodynamic preference for a thin, amorphous shell surrounding a crystalline ZB core nanoparticle at small sizes, in agreement with experimental observations. Furthermore, the size at which the onset of surface amorphisation occurs was shown to be heavily dependent on nanoparticle shape and the presence of polar or non-polar surfaces. This again revealed shape as a critical aspect of nanoparticle phase selectivity and how thermodynamic or kinetic control over the formation and growth of specific surfaces is critical in determining phase, not simply growth alone. In addition to this, size, temperature and pressure conditions which favour the formation of competing tetrapod core morphologies were identified. These results provide a means of encouraging the experimental growth and stability of pure ZB or alternatively mixed ZB/WZ tetrapods (a novel ZnS nanoparticle morphology with a number of important applications).

This study facilitates phase prediction in a way that was previously unavailable. Applied experimentally, these results and conclusions will assist in developing enhanced synthesis methods and, by controlling post-synthesis phase transformations, increase the life-span and stability of this material. This will in turn assist in the intelligent design of stable and efficient nano-devices and the formation of appropriate material safety guidelines. ZnS nanoparticles serve as a model system in this case, but pending appropriate revision of the literature, one can conceive of other situations where combining knowledge drawn from experimental, computational and theoretical sources could help map the relationship between nanomorphology and physical surroundings, and guide the development of safe, stable and effective nanotechnology[195].

References

1. Feynman, R. *There's plenty of room at the bottom*. 1959. American Physical Society, Caltech.
2. McGuinness, K., *Fabrics and nanotechnology - Molecule-sized machinery will make our clothes smarter.* Futurist, 1997. **31**(4): p. 12-12.
3. Coyle, S., et al., *Smart nanotextiles: A review of materials and applications.* Mrs Bulletin, 2007. **32**(5): p. 434-442.
4. Jones, R., *Nanotechnology, energy and markets.* Nature Nanotechnology, 2009. **4**(2): p. 75-75.
5. Saunders, J.R., et al., *Nanotechnology's implications for select systems of renewable energy.* International Journal of Green Energy, 2007. **4**: p. 483-503.
6. Daniel, M.C. and D. Astruc, *Gold nanoparticles: Assembly, supramolecular chemistry, quantum-size-related properties, and applications toward biology, catalysis, and nanotechnology.* Chemical Reviews, 2004. **104**: p. 293-346.
7. Glenn, J.C., *Nanotechnology: Future military environmental health considerations.* Technological Forecasting and Social Change, 2006. **73**(2): p. 128-137.
8. Altmann, J. and M.A. Gubrud, *Military, Arms Control, and Security Aspects of Nanotechnology.* Discovering the Nanoscale, 2004.
9. Bruchez, M., et al., *Semiconductor nanocrystals as fluorescent biological labels.* Science, 1998. **281**(5385): p. 2013-2016.
10. Chan, W.C.W. and S.M. Nie, *Quantum dot bioconjugates for ultrasensitive nonisotopic detection.* Science, 1998. **281**(5385): p. 2016-2018.
11. Medintz, I.L., et al., *Quantum dot bioconjugates for imaging, labelling and sensing.* Nature Materials, 2005. **4**(6): p. 435-446.
12. Hashimoto, K., et al., *Advanced materials for global carbon dioxide recycling.* Materials Science and Engineering a-Structural Materials Properties Microstructure and Processing, 2001. **304**: p. 88-96.
13. Goettmann, F., A. Thomas, and M. Antonietti, *Metal-free activation of CO_2 by mesoporous graphitic carbon nitride.* Angewandte Chemie-International Edition, 2007. **46**(15): p. 2717-2720.
14. Roco, M.C., *Broader societal issues of nanotechnology.* Journal of Nanoparticle Research, 2003. **5**(3-4): p. 181-189.
15. *Nanoscience and Nanotechnology: Opportunities and Uncertainties.* Document 19/04 (The Royal Society, London, 2004)
16. Cormick, C., *The complexity of public engagement*. Nature Nanotechnology, 2012. **7**: p. 77-78
17. Nel, A., et al., *Toxic potential of materials at the nanolevel.* Science, 2006. **311**(5761): p. 622-627.
18. Wiseman, H. and B. Halliwell, *Damage to DNA by reactive oxygen and nitrogen species: Role in inflammatory disease and progression to cancer*. Biochemical Journal, 1996. **313**: p. 17-29
19. Albrecht, M.A., C.W. Evans, and C.L. Raston, *Green chemistry and the health implications of nanoparticles.* Green Chemistry, 2006. **8**(5): p. 417-432.
20. Donaldson, K., et al., *Nanotoxicology.* Occupational and Environmental Medicine, 2004. **61**(9): p. 727-728.
21. Hardman, R., *A toxicologic review of quantum dots: Toxicity depends on physicochemical and environmental factors.* Environmental Health Perspectives, 2006. **114**(2): p. 165-172.

22. Nohynek, G., E. Dufour, and M. Roberts, *Nanotechnology, Cosmetics and the Skin: Is There a Health Risk?* Skin Pharmacology and Physiology, 2008. **21**(3): p. 136.
23. Oberdorster, E., *Manufactured nanomaterials (Fullerenes, C-60) induce oxidative stress in the brain of juvenile largemouth bass.* Environmental Health Perspectives, 2004. **112**(10): p. 1058-1062.
24. Oberdorster, G., E. Oberdorster, and J. Oberdorster, *Nanotoxicology: An emerging discipline evolving from studies of ultrafine particles.* Environmental Health Perspectives, 2005. **113**(7): p. 823-839.
25. Barnard, A. S. (2011), ChemInform Abstract: *Size-Dependent Phase Transitions and Phase Reversal at the Nanoscale*. ChemInform, 42(7) DOI: 10.1002/chin.201107218
26. Kelly, K.L., et al., *The optical properties of metal nanoparticles: The influence of size, shape, and dielectric environment.* Journal of Physical Chemistry B, 2003. **107**(3): p. 668-677.
27. Barnard, A.S., *Nanohazards: Knowledge is our first defence.* Nature Materials, 2006. **5**(4): p. 245.
28. Barnard, A.S., *How can ab initio simulations address risks in nanotech?* Nature Nanotechnology, 2009. **4**(6): p. 332-335.
29. Fang, X., et al., *ZnS nanostructures: From synthesis to applications.* Progress in Materials Science, 2011. **56**(2): p. 175-287.
30. Manzoor, K., et al., *Bio-conjugated luminescent quantum dots of doped ZnS: a cyto-friendly system for targeted cancer imaging.* Nanotechnology, 2009. **20**(6): p. 13.
31. He, J.H., et al., *ZnS/Silica nanocable field effect transistors as biological and chemical nanosensors.* Journal of Physical Chemistry C, 2007. **111**(33): p. 12152-12156.
32. Manzoor, K., et al., *Multicolor electroluminescent devices using doped ZnS nanocrystals.* Applied Physics Letters, 2004. **84**(2): p. 284-286.
33. Hwang, J.M., et al., *Preparation and characterization of ZnS based nano-crystalline particles for polymer light-emitting diodes.* Current Applied Physics, 2005. **5**(1): p. 31-34.
34. Kim, J.U., M.H. Lee, and H. Yang, *Synthesis of Zn1-xCdxS:Mn/ZnS quantum dots and their application to light-emitting diodes.* Nanotechnology, 2008. **19**(46): p. 5.
35. Kanemoto, M., et al., *Semiconductor photocatalysis - effective photoreduction of carbon-dioxide catalyzed by zns quantum crystallites with low-density of surface-defects.* Journal of Physical Chemistry, 1992. **96**(8): p. 3521-3526.
36. Torres-Martinez, C.L., et al., *Efficient photocatalytic degradation of environmental pollutants with mass-produced ZnS nanocrystals.* Journal of Colloid and Interface Science, 2001. **240**(2): p. 525-532.
37. Yang, S.M., et al., *High photostability and quantum yield of nanoporous TiO2 thin film electrodes co-sensitized with capped sulfides*, Journal of Materials Chemistry, 2002. **12**(5): p. 1459–1464
38. Chen, Z.G., at al*., Silicon-induced oriented ZnS nanobelts for hydrogen sensitivity*. Nanotech, 2008. **19**(5): p. 055710
39. Luo, L., et al., *A cataluminescence gas sensor for carbon tetrachloride based on nanosized ZnS.* Analytica Chimica Acta, 2009. **635**(2): p. 183-187.
40. Chen, Z.G., et al., *ZnS Branched Architectures as Optoelectronic Devices and Field Emitters.* Advanced Materials, 2010. **22**(21): p. 2376-2380
41. Chen, Z.G., et al., *Growth, Cathodoluminescence and Field Emission of ZnS Tetrapod Tree-like Heterostructures*. Advanced Functional Materials, 2008. 18(19): p 3063-3069

42. Murakoshi, K., et al., *Phase transition of ZnS nanocrystallites induced by surface modification at ambient temperature and pressure confirmed by electron diffraction.* Chemical Communications, 1998(3): p. 321-322.
43. Murakoshi, K., H. Hosokawa, and S. Yanagida, *Controlling microscopic surface structure, crystalline size and crystallinity of CdS and ZnS nanocrystallites.* 1999: p. 522-527.
44. Zhang, H.Z., et al., *Water-driven structure transformation in nanoparticles at room temperature.* Nature, 2003. **424**(6952): p. 1025-1029.
45. Hosokawa, H., et al., *Extended x-ray absorption fine structure analysis of ZnS nanocrystallites in N,N-dimethylformamide. An effect of counterions on the microscopic structure of a solvated surface.* Langmuir, 1996. **12**(15): p. 3598-3603.
46. Fujiwara, H., et al., *Observation of adsorbed N,N-dimethylformamide molecules on colloidal ZnS nanocrystallites. Effect of coexistent counteranion on surface structure.* Langmuir, 1998. **14**(15): p. 4070-4073.
47. Qadri, S.B., et al., *Size-induced transition-temperature reduction in nanoparticles of ZnS.* Physical Review B, 1999. **60**(13): p. 9191-9193.
48. Qadri, S.B., et al., *The effect of particle size on the structural transitions in zinc sulfide.* Journal of Applied Physics, 2001. **89**(1): p. 115-119.
49. Pan, Y.W., et al., *Pressure-induced structural transitions of the zinc sulfide nano-particles with different sizes.* Journal of Materials Science & Technology, 2007. **23**(2): p. 193-195.
50. Desgreniers, S., L. Beaulieu, and I. Lepage, *Pressure-induced structural changes in ZnS.* Physical Review B, 2000. **61**(13): p. 8726.
51. Li, S., J.S. Lian, and Q. Jiang, *Modeling size and surface effects on ZnS phase selection.* Chemical Physics Letters, 2008. **455**(4-6): p. 202-206.
52. Yang, C.Z., et al., *Pressure-induced transition-temperature reduction in ZnS nanoparticles.* Nanotechnology, 2008. **19**(9).
53. Gilbert, B., et al., *Synchrotron analysis of ZnS nanoparticle structure and surface-driven structural transitions.* 2003: p. 432.
54. Zhang, H.Z., et al., *Molecular dynamics simulations, thermodynamic analysis, and experimental study of phase stability of zinc sulfide nanoparticles.* Journal of Physical Chemistry B, 2003. **107**(47): p. 13051-13060.
55. Zhang, H.Z., et al. *Phase stability of nanocrystalline ZnS by thermodynamic analysis and experimental study*. 2003. Amer Chemical Soc.
56. Huang, F., et al., *Reversible, surface-controlled structure transformation in nanoparticles induced by an aggregation state.* Physical Review Letters, 2004. **92**(15): p. 4.
57. Gilbert, B., et al., *Analysis and simulation of the structure of nanoparticles that undergo a surface-driven structural transformation.* Journal of Chemical Physics, 2004. **120**(24): p. 11785-11795.
58. Zhang, H.Z. and J.F. Banfield, *Aggregation, coarsening, and phase transformation in ZnS nanoparticles studied by molecular dynamics simulations.* Nano Letters, 2004. **4**(4): p. 713-718.
59. Huang, F. and J.F. Banfield, *Size-dependent phase transformation kinetics in nanocrystalline ZnS.* Journal of the American Chemical Society, 2005. **127**(12): p. 4523-4529.
60. Gilbert, B., et al., *Surface chemistry controls crystallinity of ZnS nanoparticles.* Nano Letters, 2006. **6**(4): p. 605-610.

61. Zhang, H.Z., J.R. Rustad, and J.F. Banfield, *Interaction between water molecules and zinc sulfide nanoparticles studied by temperature-programmed desorption and molecular dynamics simulations.* Journal of Physical Chemistry A, 2007. **111**(23): p. 5008-5014.
62. Huang, T.T., K. Tan, and M.H. Lin, *A theoretical exploration of the interaction of adsorptive molecules with the ZnS clusters.* Journal of Molecular Structure-Theochem, 2007. **821**(1-3): p. 101-105.
63. Goodell, C.M., et al., *Kinetics of water adsorption-driven structural transformation of ZnS nanoparticles.* Journal of Physical Chemistry C, 2008. **112**(13): p. 4791-4796.
64. Hamad, S., S. Cristol, and C.R.A. Catlow, *Surface structures and crystal morphology of ZnS: Computational study.* Journal of Physical Chemistry B, 2002. **106**(42): p. 11002-11008.
65. Hamad, S., et al., *Structure and properties of ZnS nanoclusters.* Journal of Physical Chemistry B, 2005. **109**(7): p. 2703-2709.
66. Hamad, S., S. Cristol, and C.R.A. Catlow, *Simulation of the embryonic stage of ZnS formation from aqueous solution.* Journal of the American Chemical Society, 2005. **127**(8): p. 2580-2590.
67. Hamad, S. and C.R.A. Catlow, *Computational study of the relative stabilities of ZnS clusters, for sizes between 1 and 4 nm*. Journal of Crystal Growth 2006: p. 2-8.
68. Spano, E., S. Hamad, and C.R.A. Catlow, *Computational evidence of bubble ZnS clusters.* Journal of Physical Chemistry B, 2003. **107**(38): p. 10337-10340.
69. Spano, E., S. Hamad, and C.R.A. Catlow, *ZnS bubble clusters with onion-like structures.* Chemical Communications, 2004(7): p. 864-865.
70. Barnard A., *Using theory and modelling to investigate shape at the nanoscale.* Journal of Materials Chemistry, 2006. **16**(9): p. 813–815
71. Alivisatos, A.P., *Semiconductor clusters, nanocrystals, and quantum dots.* Science, 1996. **271**(5251): p. 933-937.
72. Xu, Y.N. and W.Y. Ching, *Electronic, optical, and structural-properties of some wurtzite crystals.* Physical Review B, 1993. **48**(7): p. 4335-4351.
73. Bhargava, R.N., et al., *Optical-properties of manganese-doped nanocrystals of ZnS.* Physical Review Letters, 1994. **72**(3): p. 416-419.
74. Bhargava, R.N., *Doped nanocrystalline materials -- Physics and applications.* Journal of Luminescence, 1996. **70**(1-6): p. 85-94.
75. Sooklal, K., et al., *Photophysical properties of ZnS nanoclusters with spatially localized Mn2+.* Journal of Physical Chemistry, 1996. **100**(11): p. 4551-4555.
76. Yu, I., T. Isobe, and M. Senna, *Optical properties and characteristics of ZnS nanoparticles with homogeneous Mn distribution.* Journal of Physics and Chemistry of Solids, 1996. **57**(4): p. 373-379.
77. Bol, A.A. and A. Meijerink, *Long-lived Mn2+ emission in nanocrystalline ZnS : Mn2+.* Physical Review B, 1998. **58**(24): p. 15997-16000.
78. Murase, N., et al., *Fluorescence and EPR characteristics of Mn2+-doped ZnS nanocrystals prepared by aqueous colloidal method.* Journal of Physical Chemistry B, 1999. **103**(5): p. 754-760.
79. Lu, S.W., et al., *Synthesis and photoluminescence enhancement of Mn2+-doped ZnS nanocrystals.* Journal of Luminescence, 2000. **92**(1-2): p. 73-78.
80. Yang, H.S., P.H. Holloway, and B.B. Ratna, *Photoluminescent and electroluminescent properties of Mn-doped ZnS nanocrystals.* Journal of Applied Physics, 2003. **93**(1): p. 586-592.

81. Han, S.-D., et al., *Synthesis and photoluminescence properties of Mn2+ doped ZnS nano-crystals with surface passivation.* Materials Chemistry and Physics, 2008. **112**(3): p. 1083-1087.
82. Sarkar, R., et al., *Yellow-orange light emission from Mn2+-doped ZnS nanoparticles.* Physica E: Low-dimensional Systems and Nanostructures, 2008. **40**(10): p. 3115-3120.
83. Yanagida, S., K. Mizumoto, and C. Pac, *Semiconductor Photocatalysis .6. Cis-Trans Photoisomerization Of Simple Alkenes Induced By Trapped Holes At Surface-States.* Journal of the American Chemical Society, 1986. **108**(4): p. 647-654.
84. Yanagida, S., et al., *Semiconductor Photocatalysis .7. Zns-Catalyzed Photoreduction Of Aldehydes And Related Derivatives - 2-Electron-Transfer Reduction And Relationship With Spectroscopic Properties.* Journal of Physical Chemistry, 1989. **93**(6): p. 2576-2582.
85. Yanagida, S., et al., *Semiconductor Photocatalysis .9. Quantitative Photoreduction Of Aliphatic-Ketones To Alcohols Using Defect-Free Zns Quantum Crystallites.* Journal of Physical Chemistry, 1990. **94**(7): p. 3104-3111.
86. Yanagida, S., et al., *Semiconductor Photocatalysis .17. Zns-Nanocrystallite-Catalyzed Photooxidation Of Organic-Compounds.* Bulletin of the Chemical Society of Japan, 1995. **68**(7): p. 1811-1823.
87. Kanemoto, M., et al., *Semiconductor photocatalysis .20. Role of surface in the photoreduction of carbon dioxide catalysed by colloidal ZnS nanocrystallites in organic solvent.* Journal of the Chemical Society-Faraday Transactions, 1996. **92**(13): p. 2401-2411.
88. Stroyuk, A.L., et al., *Zinc sulfide nanoparticles: Spectral properties and photocatalytic activity in metals reduction reactions.* Journal of Nanoparticle Research, 2007. **9**(6): p. 1027-1039.
89. Li, Y., X. He, and M. Cao, *Micro-emulsion-assisted synthesis of ZnS nanospheres and their photocatalytic activity.* Materials Research Bulletin, 2008. **43**(11): p. 3100-3110.
90. Park, W., et al., *ZnS-based photonic crystals.* 2002: p. 949-960.
91. Toyama, T., et al., *An electroluminescence device for printable electronics using coprecipitated ZnS:Mn nanocrystal ink.* Nanotechnology, 2009. **20**(5): p. 5.
92. Wang, L.Y., et al., *Fluorescence for the determination of protein with functionalized nano-ZnS.* Analyst, 2002. **127**(11): p. 1531-1534.
93. Li, Y.X., et al., *Preparation and application of cysteine-capped ZnS nanoparticles as fluorescence probe in the determination of nucleic acids.* Spectrochimica Acta Part a-Molecular and Biomolecular Spectroscopy, 2004. **60**(8-9): p. 1719-1724.
94. Li, Y.X., et al., *Application of L-cysteine-capped ZnS nanoparticles in the determination of nucleic acids using the resonance light scattering method.* Microchimica Acta, 2004. **146**(1): p. 13-19.
95. Luo, X.L., et al., *Application of nanoparticles in electrochemical sensors and biosensors.* Electroanalysis, 2006. **18**(4): p. 319-326.
96. Zhang, F.F., et al., *ZnS quantum dots derived a reagentless uric acid biosensor.* Talanta, 2006. **68**(4): p. 1353-1358.
97. Kailasa, S.K., K. Kiran, and H.F. Wu, *Comparison of ZnS Semiconductor Nanaoparticles Capped with Various Functional Groups as the Matrix and Affinity Probes for Rapid Analysis of Cyclodextrins and Proteins in Surface-Assisted Laser Desorption/Ionization Time-of-Flight Mass Spectrometry.* Analytical Chemistry, 2008. **80**(24): p. 9681-9688.
98. Rabiee, M., et al., *A new method of biomolecular recognition of avidin by light scattering of ZnS : Mn nano-particles.* Pigment & Resin Technology, 2008. **37**(4): p. 224-228.

99. Tu, R.Y., et al., *Amine-capped ZnS-Mn2+ nanocrystals for fluorescence detection of trace TNT explosive.* Analytical Chemistry, 2008. **80**(9): p. 3458-3465.
100. He, Y., H.F. Wang, and X.P. Yan, *Exploring Mn-doped ZnS quantum dots for the room-temperature phosphorescence detection of enoxacin in biological fluids.* Analytical Chemistry, 2008. **80**(10): p. 3832-3837.
101. Li, L., et al., *Application of functionalized ZnS nanoparticles to determinate uracil and thymine as a fluorescence probe.* Materials Chemistry and Physics, 2009. **113**(2-3): p. 905-908.
102. Wang, H.F., et al., *Surface Molecular Imprinting on Mn-Doped ZnS Quantum Dots for Room-Temperature Phosphorescence Optosensing of Pentachlorophenol in Water.* Analytical Chemistry, 2009. **81**(4): p. 1615-1621.
103. Dabbousi, B.O., et al., *(CdSe)ZnS core-shell quantum dots: Synthesis and characterization of a size series of highly luminescent nanocrystallites.* Journal of Physical Chemistry B, 1997. **101**(46): p. 9463-9475.
104. Peng, X.G., et al., *Epitaxial growth of highly luminescent CdSe/CdS core/shell nanocrystals with photostability and electronic accessibility.* Journal of the American Chemical Society, 1997. **119**(30): p. 7019-7029.
105. Krasnov, A.N., *Electroluminescent displays: history and lessons learned.* Displays, 2003. **24**(2): p. 73-79.
106. Xu, J.F., et al., *Preparation of ZnS nanoparticles by ultrasonic radiation method.* Applied Physics a-Materials Science & Processing, 1998. **66**(6): p. 639-641.
107. Nanda, J., et al., *Size-selected zinc sulfide nanocrystallites: Synthesis, structure, and optical studies.* Chemistry of Materials, 2000. **12**(4): p. 1018-1024.
108. Wang, L.P. and G.Y. Hong, *A new preparation of zinc sulfide nanoparticles by solid-state method at low temperature.* Materials Research Bulletin, 2000. **35**(5): p. 695-701.
109. Berlier, G., et al., *Synthesis and characterisation of small ZnS particles.* Research on Chemical Intermediates, 2006. **32**(7): p. 683-693.
110. Han, J., et al., *Novel synthesis of semiconductor nanocrystalline ZnS.* Materials Science and Technology, 2007. **23**(2): p. 250-251.
111. Zeng, H.Z., et al., *A new way to synthesize ZnS nanoparticles.* Chinese Chemical Letters, 2007. **18**(4): p. 483-486.
112. Saravanan, N., et al., *Simple synthesis of ZnS nanoparticles in alkaline medium.* Journal of Materials Science-Materials in Electronics, 2008. **19**(12): p. 1206-1208.
113. Ye, X., et al., *A facile two-phase approach to nearly monodisperse ZnS nanocrystals.* Materials Chemistry and Physics, 2008. **112**(3): p. 730-733.
114. Tong, H., et al., *Self-assembled ZnS nanostructured spheres: Controllable crystal phase and morphology.* Journal of Physical Chemistry C, 2007. **111**(10): p. 3893-3900.
115. Dawood, F. and R.E. Schaak, *ZnO-Templated Synthesis of Wurtzite-Type ZnS and ZnSe Nanoparticles.* Journal of the American Chemical Society, 2009. **131**(2): p. 424-+.
116. Liu, W., *Low temperature synthesis of hexagonal phase ZnS nanocrystals by thermolysis of an air-stable single-source molecular precursor in air.* Materials Letters, 2006. **60**(4): p. 551-554.
117. Lu, H.Y., S.Y. Chu, and S.S. Tan, *The characteristics of low-temperature-synthesized ZnS and ZnO nanoparticles.* Journal of Crystal Growth, 2004. **269**(2-4): p. 385-391.

118. Sun, J.-Q., et al., *Low-temperature synthesis of hexagonal ZnS nanoparticles by a facile microwave-assisted single-source method.* Solid State Communications, 2008. **147**(11-12): p. 501-504.
119. Zhao, Y.W., et al., *Low-temperature synthesis of hexagonal (wurtzite) ZnS nanocrystals.* Journal of the American Chemical Society, 2004. **126**(22): p. 6874-6875.
120. Fujiwara, H., et al., *Surface characteristics of ZnS nanocrystallites relating to their photocatalysis for CO2 reduction.* Langmuir, 1998. **14**(18): p. 5154-5159.
121. Gibbs, J.W., *The collected works of J. Willard Gibbs*. 1928, New York: Longman.
122. Barnard, A.S. and H.F. Xu, *An Environmentally Sensitive Phase Map of Titania Nanocrystals.* ACS Nano, 2008. **2**(11): p. 2237-2242.
123. Barnard, A.S., *A thermodynamic model for the shape and stability of twinned nanostructures.* Journal of Physical Chemistry B, 2006. **110**(48): p. 24498-24504.
124. Barnard, A.S. and P. Zapol, *A model for the phase stability of arbitrary nanoparticles as a function of size and shape.* Journal of Chemical Physics, 2004. **121**(9): p. 4276-4283.
125. Barnard, A.S. and L.A. Curtiss, *Prediction of TiO2 nanoparticle phase and shape transitions controlled by surface chemistry.* Nano Letters, 2005. **5**(7): p. 1261-1266.
126. Barnard, A.S. and P. Zapol, *Effects of particle morphology and surface hydrogenation on the phase stability of TiO2.* Physical Review B, 2004. **70**(23).
127. Barnard, A.S., P. Zapol, and L.A. Curtiss, *Modeling the morphology and phase stability of TiO2 nanocrystals in water.* Journal of Chemical Theory and Computation, 2005. **1**(1): p. 107-116.
128. Barnard, A.S. and S.P. Russo, *Shape and thermodynamic stability of pyrite FeS2 nanocrystals and nanorods.* Journal of Physical Chemistry C, 2007. **111**(31): p. 11742-11746.
129. Barnard, A.S. and S.P. Russo, *Modelling nanoscale FeS(2) formation in sulfur rich conditions.* Journal of Materials Chemistry, 2009. **19**(21): p. 3389-3394.
130. Barnard, A.S. and S.P. Russo, *Morphological Stability of Pyrite FeS(2) Nanocrystals in Water.* Journal of Physical Chemistry C, 2009. **113**(14): p. 5376-5380.
131. Deore, S. and A. Navrotsky, *Oxide melt solution calorimetry of sulfides: Enthalpy of formation of sphalerite, galena, greenockite, and hawleyite.* American Mineralogist, 2006. **91**(2-3): p. 400-403.
132. Deore, S., F. Xu, and A. Navrotsky, *Oxide-melt solution calorimetry of selenides: Enthalpy of formation of zinc, cadmium, and lead selenide.* American Mineralogist, 2008. **93**(5-6): p. 779-783.
133. Wulff, G., *On the question of speed of growth and dissolution of crystal surfaces.* Zeitschrift Fur Krystallographie Und Mineralogie, 1901. **34**(5/6): p. 449-530.
134. Reuter, K. and M. Scheffler, *First-principles atomistic thermodynamics for oxidation catalysis: Surface phase diagrams and catalytically interesting regions.* Physical Review Letters, 2003. **90**(4).
135. Rogal, J., K. Reuter, and M. Scheffler, *Thermodynamic stability of PdO surfaces.* Physical Review B, 2004. **69**(7).
136. Hohenberg, P. and W. Kohn, *Inhomogeneous electron gas.* Physical Review B, 1964. **136**(3B): p. B864-B871.
137. Kohn, W. and L.J. Sham, *Self-consistent equations including exchange and correlation effects.* Physical Review, 1965. **140**(4A): p. 1133-1138.
138. Casali, R.A. and N.E. Christensen, *Elastic constants and deformation potentials of ZnS and ZnSe under pressure.* Solid State Communications, 1998. **108**(10): p. 793-798.

139. Wang, S.Q., *A comparative first-principles study of ZnS and ZnO in zinc blende structure.* Journal of Crystal Growth, 2006. **287**(1): p. 185-188.
140. Khenata, R., et al., *Elastic, electronic and optical properties of ZnS, ZnSe and ZnTe under pressure.* Computational Materials Science, 2006. **38**(1): p. 29-38.
141. Rabah, M., et al., *Calculation of structural, optical and electronic properties of ZnS, ZnSe, MgS, MgSe and their quaternary alloy Mg1-xZnxSySe1-y.* Materials Science and Engineering B-Solid State Materials for Advanced Technology, 2003. **100**(2): p. 163-171.
142. Qteish, A. and A. Munoz, *Stability and structural properties of ZnS and ZnSe under high pressure.* Physica Status Solidi B-Basic Research, 2001. **223**(2): p. 417-422.
143. Ves, S., et al., *Cubic zns under pressure - optical-absorption edge, phase-transition, and calculated equation of state.* Physical Review B, 1990. **42**(14): p. 9113-9118.
144. Lopez-Solano, J., et al., *Theoretical study of ZnS under high pressure.* Physica Status Solidi B-Basic Research, 2003. **235**(2): p. 452-455.
145. Bilge, M., et al., *B3-B1 phase transition and pressure dependence of elastic properties of ZnS.* Materials Chemistry and Physics, 2008. **111**(2-3): p. 559-564.
146. Sahraoui, F.A., et al., *Effect of pressure on the structural and elastic properties of ZnS and MgS alloys in the B3 and B1 phases.* Materials Letters, 2007. **61**(10): p. 1978-1981.
147. Chen, X.R., et al., *Pressure induced phase transition in ZnS.* Solid State Communications, 2006. **139**(5): p. 246-249.
148. Rinke, P., et al., *Combining GW calculations with exact-exchange density-functional theory: an analysis of valence-band photoemission for compound semiconductors.* New Journal of Physics, 2005. **7**: p. 126
149. Yandong M., Y. Dai and B.B. Huang *Magnetism in non-transition-metal doped CdS studied by density functional theory*. Computational Materials Science 2011. **50**(5): p. 1661–1666
150. Ekuma E.C., et al., *Ab-initio local density approximation description of the electronic properties of zinc blende cadmium sulfide (zb-CdS).* Physica B - Condensed Matter, 2011. **406**(8): p. 1477–1480
151. Kresse, G. and J. Furthmuller, *Efficient iterative schemes for ab initio total-energy calculations using a plane-wave basis set.* Physical Review B, 1996. **54**(16): p. 11169-11186.
152. Kresse, G. and J. Hafner, Ab Initio *Molecular-Dynamics For Liquid-Metals.* Physical Review B, 1993. **47**(1): p. 558-561.
153. Benkabou, F., H. Aourag, and M. Certier, *Atomistic study of zinc-blende CdS, CdSe, ZnS, and ZnSe from molecular dynamics.* Materials Chemistry and Physics, 2000. **66**(1): p. 10-16.
154. Nye, J.F., *Physical Properties of Crystals*. 1985, New York: Oxford University Press.
155. Boettger, J.C., *All-electron full-potential calculation of the electronic band structure, elastic constants, and equation of state for graphite.* Physical Review B, 1997. **55**(17): p. 11202-11211.
156. Scott, S.D. and H.L. Barnes, *Sphalerite-Wurtzite Equilibria And Stoichiometry.* Geochimica Et Cosmochimica Acta, 1972. **36**(11): p. 1275-&.
157. Becke, A.D., *Density-functional thermochemistry .3. The role of exact exchange.* Journal of Chemical Physics, 1993. **98**(7): p. 5648-5652.
158. Perdew, J.P., K. Burke, and M. Ernzerhof, *Generalized gradient approximation made simple.* Physical Review Letters, 1996. **77**(18): p. 3865-3868.

159. Perdew, J.P. and Y. Wang, *Accurate and simple analytic representation of the electron-gas correlation-energy.* Physical Review B, 1992. **45**(23): p. 13244-13249.
160. Feigl, C.A., S.P. Russo, and A.S. Barnard, *A comparative density functional theory investigation of the mechanical and energetic properties of ZnS.* Molecular Simulation, 2011. **37**(4): p. 321-333.
161. Ceperley, D.M. and B.J. Alder, *Ground State of the Electron Gas by a Stochastic Method.* Physical Review Letters, 1980. **45**(7): p. 566.
162. Jamieson, J.C. and H.H. Demarest, *A note on the compression of cubic ZnS.* Journal of Physics and Chemistry of Solids, 1980. **41**(9): p. 963-964.
163. Berlincourt, D., H. Jaffe, and L.R. Shiozawa, *Electroelastic Properties of the Sulfides, Selenides, and Tellurides of Zinc and Cadmium.* Physical Review, 1963. **129**(3): p. 1009.
164. Catti, M., Y. Noel, and R. Dovesi, *Full piezoelectric tensors of wurtzite and zinc blende ZnO and ZnS by first-principles calculations.* Journal of Physics and Chemistry of Solids, 2003. **64**(11): p. 2183-2190.
165. Hafner, J., *Ab-initio simulations of materials using VASP: Density-functional theory and beyond.* Journal of Computational Chemistry, 2008. **29**(13): p. 2044-2078.
166. Pandey, D.K., R.K. Yadawa, and R.R. Yadav, *Ultrasonic properties of hexagonal ZnS at nanoscale.* Materials Letters, 2007. **61**: p. 5194-5198.
167. Barnard, A.S., C.A. Feigl, and S.P. Russo, *Morphological and phase stability of zinc blende, amorphous and mixed core-shell ZnS nanoparticles.* Nanoscale, 2010. **2**(10): p. 2294-2301.
168. Wright, K., et al., *Simulation of the structure and stability of sphalerite (ZnS) surfaces.* American Mineralogist, 1998. **83**(1-2): p. 141-146.
169. Gale, J.D. and A.L. Rohl, *The General Utility Lattice Program (GULP).* Molecular Simulation, 2003. **29**(5): p. 291-341.
170. Barnard, A.S., *Self-assembly in nanodiamond agglutinates.* Journal of Materials Chemistry, 2008. **18**(34): p. 4038-4041.
171. Banhart, F., *Irradiation effects in carbon nanostructures.* Reports on Progress in Physics, 1999. **62**(8): p. 1181-1221.
172. Barnard, A.S. and M. Sternberg, *Crystallinity and surface electrostatics of diamond nanocrystals.* Journal of Materials Chemistry, 2007. **17**(45): p. 4811-4819.
173. Daskalakis, K.D. and G.R. Helz, *The Solubility Of Sphalerite (Zns) In Sulfidic Solutions At 25-Degrees-C And 1 Atm Pressure.* Geochimica Et Cosmochimica Acta, 1993. **57**(20): p. 4923-4931.
174. Hayashi, K., A. Sugaki, and A. Kitakaze, *Solubility Of Sphalerite In Aqueous Sulfide Solutions At Temperatures Between 25-Degrees And 240-Degrees-C.* Geochimica Et Cosmochimica Acta, 1990. **54**(3): p. 715-725.
175. Gubeli, A.O. and J. Ste-Marie, *Constantes de stabilité de thiocomplexes et produits de solubilité de sulfures de métaux. II Sulfure de zinc.* Canadian Journal of Chemistry, 1967. **45**(18): p. 2101-2108.
176. Yogamalar, N.R. and A.C. Bose, *Tuning the aspect ratio of hydrothermally grown ZnO by choice of precursor.* Journal of Solid State Chemistry, 2011. **184**(1): p. 12-20.
177. Sun, L., et al., *Tuning the properties of magnetic nanowires.* Ibm Journal of Research and Development, 2005. **49**(1): p. 79-102.
178. Simmons, B.A., et al., *Morphology of CdS nanocrystals synthesized in a mixed surfactant system.* Nano Letters, 2002. **2**(4): p. 263-268.

179. Li, Y.C., et al., *Controlled synthesis of CdS nanorods and hexagonal nanocrystals.* Journal of Materials Chemistry, 2003. **13**(10): p. 2641-2648.

180. Feigl, C.A., A.S. Barnard, and S.P. Russo, *Size- and shape-dependent phase transformations in wurtzite ZnS nanostructures.* Physical Chemistry Chemical Physics, 2012. **14**(28): p. 9871-9879.

181. Li, S. and G.W. Yang, *Phase Transition of II-VI Semiconductor Nanocrystals.* Journal of Physical Chemistry C, 2010. **114**(35): p. 15054-15060.

182. Aymes, D., et al., *Experimental set up for determining the temperature-oxygen partial pressure conditions during synthesis of spinel oxide nanoparticles.* Solid State Ionics, 1997. **101**: p. 261-264.

183. Wang, H. and C. Me, *The effects of oxygen partial pressure on the microstructures and photocatalytic property of ZnO nanoparticles.* Physica E-Low-Dimensional Systems & Nanostructures, 2008. **40**(8): p. 2724-2729.

184. Zeng, D.W., et al., *Oxygen partial pressure effect on synthesis and characteristics of Sb2O3 nanoparticles.* Materials Science and Engineering a-Structural Materials Properties Microstructure and Processing, 2004. **366**(2): p. 332-337.

185. Mieszawska, A.J., et al., *The synthesis and fabrication of one-dimensional nanoscale heterojunctions.* Small, 2007. **3**(5): p. 722-756.

186. Uehara, M., et al., *Structural characterization of ZnS nanocrystals with a conic head using HR-TEM and HAADF tomography.* CrystEngComm, 2011. **13**(20): p. 5998-6001.

187. Feigl, C.A., A.S. Barnard, and S.P. Russo, *Modelling nanoscale cubic ZnS morphology and thermodynamic stability under sulphur-rich conditions.* CrystEngComm, 2012. DOI:10.1039/C2CE25814E

188. Manna, L., et al., *First-principles modeling of unpassivated and surfactant-passivated bulk facets of wurtzite CdSe: A model system for studying the anisotropic growth of CdSe nanocrystals.* Journal of Physical Chemistry B, 2005. **109**(13): p. 6183-6192.

189. Feigl, C.A., A.S. Barnard, and S.P. Russo *Modelling polar wurtzite ZnS nanoparticles: the effect of sulphur supersaturation on size- and shape-dependent phase transformations*. Journal of Materials Chemistry, 2012. DOI: 10.1039/C2JM33758D.

190. Fang, X., et al., *ZnO and ZnS Nanostructures: Ultraviolet-Light Emitters, Lasers, and Sensors.* Critical Reviews in Solid State and Materials Sciences, 2009. **34**(3-4): p. 190-223.

191. Manna, L., E.C. Scher, and A.P. Alivisatos, *Synthesis of soluble and processable rod-, arrow-, teardrop-, and tetrapod-shaped CdSe nanocrystals.* Journal of the American Chemical Society, 2000. **122**(51): p. 12700-12706.

192. Gong, J.F., et al., *Experimental evidence of an octahedron nucleus in ZnS tetrapods.* Small, 2006. **2**(6): p. 732-735.

193. Kar, S. and S. Biswas, *Rapid Synthesis of Core/Shell ZnS:Mn/Si Nanotetrapods by a Catalyst-Free Thermal Evaporation Route.* ACS Applied Materials & Interfaces, 2009. **1**(7): p. 1420-1426.

194. Zhu, Y.C., et al., *Nanocable-aligned ZnS tetrapod nanocrystals.* Journal of the American Chemical Society, 2003. **125**(52): p. 16196-16197.

195. Feigl, C.A., S.P. Russo, and A.S. Barnard, *Safe, stable and effective nanotechnology: phase mapping of ZnS nanoparticles*. Journal of Materials Chemistry, 2010. **20**(24): p. 4971-4980.

Appendix A. Definitions of q and fi for zinc blende shapes

The surface-to-volume ratio q and facet weighting factors f_i are defined for shapes in the zinc blende phase in terms of the average nanoparticle diameter $\langle D \rangle$ and a shape truncation factor x which describes the degree of truncation of a specific surface in seperate direction.

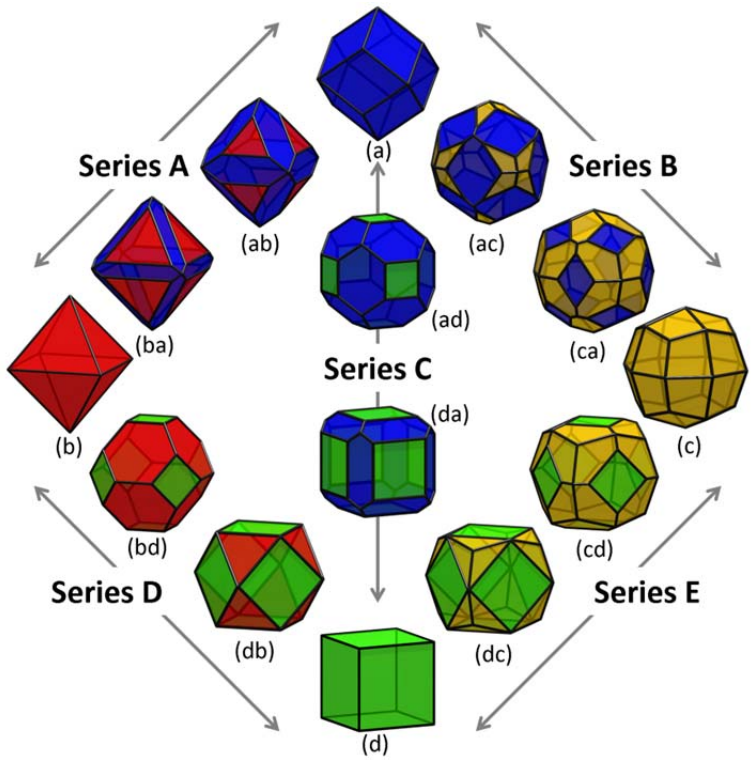

Figure A.1 – Shapes of zinc blende ZnS nanoparticles explored in Chapter 4, with truncation series terminated by (a) the Catalan rhombic dodecahedron, (b) the Platonic regular octahedron, (c) the Catalan deltoidal icositetrahedron, and (d) the Platonic regular hexahedron (or cube). The stationary points in each series are chosen such that the fraction of surface area attributed to the minority and/or majority facets conform to the ratio defined by the Platonic truncated octahedron (bd) and Archimedian cuboctahedron (db). The {220} facets are shown in blue, {111} facets are shown in red, {311} facets are shown in yellow, and {200} facets are shown in green.

The q and f_i expressions are defined below for the four series terminating shapes – the rhombic dodecahedron (a), octahedron (b), deltiodal icositetrahedron (c) and cube, or regular hexahedron (d) – in addition to the Archimedian cubeoctahedron (db). These definitions are given with respect to the surface area and volume for each shape, which are each defined in terms of the edge length 'a' for each shape.

Rhombic dodecahedron

$$V = \frac{16}{9}\sqrt{3}a^3$$
$$S = 8\sqrt{2}a^2$$
$$a = \left[\frac{9V}{16\sqrt{3}}\right]^{\frac{1}{3}}$$
$$q = \frac{1}{a}\left(\frac{8\sqrt{2}}{\frac{16}{9}\sqrt{3}}\right) = \frac{1}{a}\left(\frac{3\sqrt{3}}{2}\right)$$
$$f_{110} = 1$$

Octahedron

$$V = \frac{1}{3}\sqrt{2}a^3$$
$$S = 2\sqrt{3}a^2$$
$$a = \left[\frac{3V}{\sqrt{2}}\right]^{\frac{1}{3}}$$
$$q = \frac{1}{a}\left(\frac{2\sqrt{3}}{\frac{1}{3}\sqrt{2}}\right) = \frac{3\sqrt{6}}{a}$$
$$f_{111} = 1$$

Deltoidal icositetrahedron

$$V = \left(122 + 71\sqrt{2}\right)^{\frac{1}{2}} a^3$$
$$S = 6\left(29 - 2\sqrt{2}\right)^{\frac{1}{2}} a^2$$
$$a = \left[\frac{V}{\left(122 + 71\sqrt{2}\right)^{\frac{1}{2}}}\right]^{\frac{1}{3}}$$
$$q = \frac{1}{a}\left[\frac{6\left(29 - 2\sqrt{2}\right)^{\frac{1}{2}}}{\left(122 + 71\sqrt{2}\right)^{\frac{1}{2}}}\right]$$
$$f_{311} = 1$$

$$Cube$$

$$V = a^3$$

$$S = 6a^2$$

$$a = V^{\frac{1}{3}}$$

$$q = \frac{6}{a}$$

$$f_{100} = 1$$

$$Cubeoctahedron\,(db)$$

$$V = \frac{5}{3}\sqrt{2}a^3$$

$$S = \left(6 + 2\sqrt{3}\right)a^2$$

$$a = \left[\frac{3V}{5\sqrt{2}}\right]^{\frac{1}{3}}$$

$$q = \frac{1}{a}\left[\frac{6 + 2\sqrt{3}}{\frac{5}{3}\sqrt{2}}\right] = \frac{1}{a}\left[\frac{18 + 6\sqrt{3}}{5\sqrt{2}}\right]$$

$$f_{100} = \frac{6}{6 + 2\sqrt{3}}$$

$$f_{111} = \frac{2\sqrt{3}}{6 + 2\sqrt{3}}$$

The q and f_i expressions for the five Series in Figure A.1 – Series A to Series E – are given below. These definitions include a truncation factor x which defines the degree of truncation of a specific surface along a particular direction, and hence the exact point at which a shape exisits in the relevent Series.

Series A

$$V(x) = V_{RD}\left(1-x^3\right) + V_{Octahedron}x^3$$
$$= \frac{16}{9}\sqrt{3}a^3\left(1-x^3\right) + \frac{1}{3}\sqrt{2}a^3x^3$$

$$S(x) = S_{RD}\left(1-x^2\right) + S_{Octahedron}x^2$$
$$S(x) = 8\sqrt{2}a^2\left(1-x^2\right) + 2\sqrt{3}a^2x^2$$

$$a(x) = \left[\frac{V}{\frac{16}{9}\sqrt{3}\left(1-x^3\right) + \frac{1}{3}\sqrt{2}x^3}\right]^{\frac{1}{3}}$$

$$q(x) = \frac{1}{a}\left[\frac{8\sqrt{2}\left(1-x^2\right) + 2\sqrt{3}x^2}{\frac{16}{9}\sqrt{3}\left(1-x^3\right) + \frac{1}{3}\sqrt{2}x^3}\right]$$

$$f_{110}(x) = \frac{8\sqrt{2}\left(1-x^2\right)}{8\sqrt{2}\left(1-x^2\right) + 2\sqrt{3}x^2}$$

$$f_{111}(x) = \frac{2\sqrt{3}x^2}{8\sqrt{2}\left(1-x^2\right) + 2\sqrt{3}x^2}$$

Series B

$$V(x) = V_{RD}\left(1-x^3\right) + V_{DI}x^3$$
$$= \frac{16}{9}\sqrt{3}a^3\left(1-x^3\right) + \left(122+71\sqrt{2}\right)^{\frac{1}{2}}a^3x^3$$

$$S(x) = S_{RD}\left(1-x^2\right) + S_{DI}x^2$$
$$S(x) = 8\sqrt{2}a^2\left(1-x^2\right) + 6\left(29-2\sqrt{2}\right)^{\frac{1}{2}}a^2x^2$$

$$a(x) = \left[\frac{V}{\frac{16}{9}\sqrt{3}\left(1-x^3\right) + \left(122+71\sqrt{2}\right)^{\frac{1}{2}}x^3}\right]^{\frac{1}{3}}$$

$$q(x) = \frac{1}{a}\left[\frac{8\sqrt{2}\left(1-x^2\right) + 6\left(29-2\sqrt{2}\right)^{\frac{1}{2}}x^2}{\frac{16}{9}\sqrt{3}\left(1-x^3\right) + \left(122+71\sqrt{2}\right)^{\frac{1}{2}}x^3}\right]$$

$$f_{110}(x) = \frac{8\sqrt{2}\left(1-x^2\right)}{8\sqrt{2}\left(1-x^2\right) + 2\sqrt{3}x^2}$$

$$f_{311}(x) = \frac{6\left(29-2\sqrt{2}\right)^{\frac{1}{2}}x^2}{8\sqrt{2}\left(1-x^2\right) + 6\left(29-2\sqrt{2}\right)^{\frac{1}{2}}x^2}$$

Series C

$$V(x) = V_{RD}\left(1-x^3\right) + V_{Cube}x^3$$
$$= \frac{16}{9}\sqrt{3}a^3\left(1-x^3\right) + a^3x^3$$

$$S(x) = S_{RD}\left(1-x^2\right) + S_{Cube}x^2$$
$$S(x) = 8\sqrt{2}a^2\left(1-x^2\right) + 6a^2x^2$$

$$a(x) = \left[\frac{V}{\frac{16}{9}\sqrt{3}\left(1-x^3\right)+x^3}\right]^{\frac{1}{3}}$$

$$q(x) = \frac{1}{a}\left[\frac{8\sqrt{2}\left(1-x^2\right)+6x^2}{\frac{16}{9}\sqrt{3}\left(1-x^3\right)+x^3}\right]$$

$$f_{110}(x) = \frac{8\sqrt{2}\left(1-x^2\right)}{8\sqrt{2}\left(1-x^2\right)+6x^2}$$

$$f_{100}(x) = \frac{6x^2}{8\sqrt{2}\left(1-x^2\right)+6x^2}$$

$Series\, D, (b)\ to\ Cubeoctahedron(db)$

$$0 < x < x_{max}$$

$$x_{max} = \frac{1}{2}$$

$$\begin{aligned} V(x) &= V_{Octahedron} - 3V_{Octahedron}x^3 \\ &= V_{Octahedron}\left(1 - 3x^3\right) \\ &= \frac{1}{3}\sqrt{2}a^3\left(1 - 3x^3\right) \end{aligned}$$

$$\begin{aligned} S(x) &= S_{Octahedron} - 3S_{Octahedron}x^2 + S_{Cube}x^2 \\ &= S_{Octahedron}\left(1 - 3x^2\right) + S_{Cube}x^2 \\ &= 2\sqrt{3}a^2\left(1 - 3x^2\right) + 6a^2x^2 \end{aligned}$$

$$a(x) = \left[\frac{V}{\frac{1}{3}\sqrt{2}\left(1 - 3x^3\right)}\right]^{\frac{1}{3}}$$

$$q(x) = \frac{1}{a}\left[\frac{2\sqrt{3}\left(1 - 3x^2\right) + 6x^2}{\frac{1}{3}\sqrt{2}\left(1 - 3x^3\right)}\right]$$

$$f_{111}(x) = \frac{2\sqrt{3}\left(1 - 3x^2\right)}{2\sqrt{3}\left(1 - 3x^2\right) + 6x^2}$$

$$f_{100}(x) = \frac{6x^2}{2\sqrt{3}\left(1 - 3x^2\right) + 6x^2}$$

Series D, (d) to Cubeoctahedron

$$\begin{aligned} V(x) &= V_{Cube}\left(1-x^3\right) + V_{Cubeoctahedron}x^3 \\ &= a^3\left(1-x^3\right) + \frac{5}{3}\sqrt{2}a^3x^3 \end{aligned}$$

$$\begin{aligned} S(x) &= S_{Cube}\left(1-x^2\right) + S_{Cubeoctahedron}x^2 \\ &= 6a^2\left(1-x^2\right) + \left(6+2\sqrt{3}\right)a^2x^2 \\ &= 6a^2 + 2\sqrt{3}a^2x^2 \end{aligned}$$

$$a(x) = \left[\frac{V}{(1-x^3)+\frac{5}{3}\sqrt{2}x^3}\right]^{\frac{1}{3}} = \left[\frac{V}{1+x^3\left(\frac{5}{3}\sqrt{2}-1\right)}\right]^{\frac{1}{3}}$$

$$q(x) = \frac{1}{a}\left[\frac{6+2\sqrt{3}x^2}{1+x^3\left(\frac{5}{3}\sqrt{2}-1\right)}\right]$$

$$f_{100}(x) = \frac{6}{6+2\sqrt{3}x^2}$$

$$f_{111}(x) = \frac{2\sqrt{3}x^2}{6+2\sqrt{3}x^2}$$

$Series\ E,\ (c)\ to\ (dc)$

$$0 < x < x_{max}$$

$$x_{max} = 1.70$$

$$\begin{aligned} V(x) &= V_{DI} - 6V_{SquarePyramid} \\ &= \left(122 + 71\sqrt{2}\right)^{\frac{1}{2}} a^3 - \frac{1}{3}\sqrt{2}a^3x^3 \end{aligned}$$

$$\begin{aligned} S(x) &= S_{DI} - 6S_{SquarePyramid} + S_{Cube} \\ &= 6\left(29 - 2\sqrt{2}\right)^{\frac{1}{2}} a^2 - 2\sqrt{11}a^2x^2 + 6a^2x^2 \end{aligned}$$

$$a(x) = \left[\frac{V}{\left(122 + 71\sqrt{2}\right)^{\frac{1}{2}} - \frac{1}{3}\sqrt{2}x^3}\right]^{\frac{1}{3}}$$

$$q(x) = \frac{1}{a}\left[\frac{6\left(29 - 2\sqrt{2}\right)^{\frac{1}{2}} - 2\sqrt{11}x^2 + 6x^2}{\left(122 + 71\sqrt{2}\right)^{\frac{1}{2}} - \frac{1}{3}\sqrt{2}x^3}\right]$$

$$f_{311}(x) = \frac{6\left(29 - 2\sqrt{2}\right)^{\frac{1}{2}} - 2\sqrt{11}x^2}{6\left(29 - 2\sqrt{2}\right)^{\frac{1}{2}} - 2\sqrt{11}x^2 + 6x^2}$$

$$f_{100}(x) = \frac{6x^2}{6\left(29 - 2\sqrt{2}\right)^{\frac{1}{2}} - 2\sqrt{11}x^2 + 6x^2}$$

Series E, (d) to (dc)

$0 < x < x_{max}$

$$x_{max} = \frac{1}{\sqrt{2}}$$

$$\begin{aligned}
V(x) &= V_{Cube} - 8V_{TriPyr} + 8V'_{TriPyr} \\
&= a^3 - \frac{8}{3}A_{TriPyr}h_{TriPyr} + \frac{8}{3}A_{TriPyr}h'_{TriPyr} \\
&= a^3 + \frac{8}{3}A_{TriPyr}\left[h'_{TriPyr} - h_{TriPyr}\right] \\
&= a^3 + \frac{8}{3}\left(\frac{1}{2}b_{A_{TriPyr}}h_{A_{TriPyr}}\right)\left[\sqrt{e'^2 - \frac{(ax)^2}{3}} - \sqrt{e^2 - \frac{(ax)^2}{3}}\right] \\
&= a^3 + \frac{8}{3}\left(\frac{1}{2}ax\sqrt{(ax)^2 - \left(\frac{ax}{2}\right)^2}\right)\left[\sqrt{\left(\frac{ax}{1.70}\right)^2 - \frac{(ax)^2}{3}} - \sqrt{\left(\frac{ax}{\sqrt{2}}\right)^2 - \frac{(ax)^2}{3}}\right] \\
&= a^3 + \frac{2}{\sqrt{3}}(ax)^3\left[\left(\sqrt{\frac{1}{1.70^2} - \frac{1}{3}} - \frac{1}{\sqrt{6}}\right)\right] \\
&= a^3 - \frac{2}{\sqrt{3}}(0.296)(ax)^3 \\
&= a^3\left(1 - 0.340x^3\right)
\end{aligned}$$

$$\begin{aligned}
S(x) &= S_{Cube} - 8S_{TriPyr} + 8S'_{TriPyr} \\
&= 6a^2 - 8\left(\frac{3}{2}b_{TriPyr}s_{TriPyr}\right) + 8\left(\frac{3}{2}b_{TriPyr}s'_{TriPyr}\right) \\
&= 6a^2 + 12b_{TriPyr}\left[s'_{TriPyr} - s_{TriPyr}\right] \\
&= 6a^2 + 12ax\left[\sqrt{e'^2 - \left(\frac{ax}{2}\right)^2} - \sqrt{e^2 - \left(\frac{ax}{2}\right)^2}\right] \\
&= 6a^2 + 12ax\left[\sqrt{\left(\frac{ax}{1.70}\right)^2 - \left(\frac{ax}{2}\right)^2} - \sqrt{\left(\frac{ax}{\sqrt{2}}\right)^2 - \left(\frac{ax}{2}\right)^2}\right] \\
&= 6a^2 + 12(ax)^2\left[\sqrt{\frac{1}{1.70^2} - \frac{1}{4}} - \frac{1}{2}\right] \\
&= 6a^2 - 12(0.190)(ax)^2 \\
&= 6a^2\left(1 - 0.380x^2\right)
\end{aligned}$$

Series E, (d) to (dc) (cont.)

$$a(x) = \left[\frac{V}{1 - 0.340x^3}\right]^{\frac{1}{3}}$$

$$q(x) = \frac{1}{a}\left[\frac{6\left(1 - 0.380x^2\right)}{1 - 0.340x^3}\right]$$

$$f_{100}(x) = \frac{1 - x^2}{1 - 0.380x^2}$$

$$f_{311}(x) = \frac{3.72x^2}{6\left(1 - 0.380x^2\right)}$$

In addition to the five Series studied in Chapter 4, Chapter 6 includes the series of morphologies described by truncation of the deltoidal icositetrahedron in the <111> direction and truncation of the octahrdron in the <311> direction, as shown in Figure A.2.

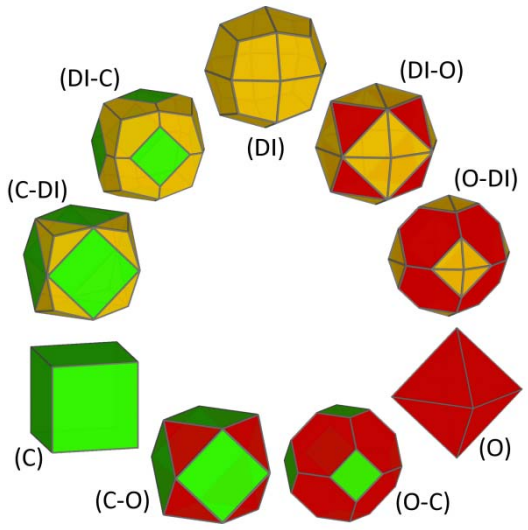

Figure A.2 – From Chapter 6, a sub-set of shapes enclosed by the polar ZnS surfaces of cubic ZnS.

With respect to figure A.2, the q and f_i expressions for the shapes located in the region occupying the space between (DI) and (DI-O), and between (O) and (DI-O) are given below.

$(DI)\,to\,(DI-O)$

$0 < x < x_{max}$

$x_{max} = 1.70$

$$\begin{aligned}
V(x) &= V_{DI} - 8V_{TriPyr} \\
&= \sqrt{122+71\sqrt{2}}a^3 - \frac{8}{3}A_{TriPyr}h_{TriPyr} \\
&= \sqrt{122+71\sqrt{2}}a^3 - \frac{8}{3}\left(\frac{1}{2}b_{A_{TriPyr}}h_{A_{TriPyr}}\right)h_{TriPyr} \\
&= \sqrt{122+71\sqrt{2}}a^3 - \frac{8}{3}\left(\frac{1}{2}ax\sqrt{(ax)^2-\left(\frac{ax}{2}\right)^2}\right)\left[\sqrt{e^2-\frac{(ax)^2}{3}}\right] \\
&= \sqrt{122+71\sqrt{2}}a^3 - \frac{2}{\sqrt{3}}(ax)^2\left[\sqrt{\left(\frac{ax}{1.70}\right)^2-\frac{(ax)^2}{3}}\right] \\
&= \sqrt{122+71\sqrt{2}}a^3 - 0.130\,(ax)^3
\end{aligned}$$

$$\begin{aligned}
S(x) &= S_{DI} - 8S_{TriPyr} + S_{Oct} \\
&= 6\sqrt{29-2\sqrt{2}}a^2 - 8\left(\frac{3}{2}b_{TriPyr}s_{TriPyr}\right) + 2\sqrt{3}\,(ax)^2 \\
&= 6\sqrt{29-2\sqrt{2}}a^2 - 12ax\sqrt{e^2-\left(\frac{ax}{2}\right)^2} + 2\sqrt{3}\,(ax)^2 \\
&= 6\sqrt{29-2\sqrt{2}}a^2 - 12ax\sqrt{\left(\frac{ax}{1.70}\right)^2-\left(\frac{ax}{2}\right)^2} + 2\sqrt{3}\,(ax)^2 \\
&= 6\sqrt{29-2\sqrt{2}}a^2 - 3.72\,(ax)^2 + 2\sqrt{3}\,(ax)^2
\end{aligned}$$

$$a(x) = \left[\frac{V}{\sqrt{122+71\sqrt{2}-0.130x^3}}\right]^{\frac{1}{3}}$$

$$q(x) = \frac{1}{a}\left[\frac{6\sqrt{29-2\sqrt{2}}-3.72x^2+2\sqrt{3}x^2}{\sqrt{122+71\sqrt{2}-0.130x^3}}\right]$$

$$f_{311}(x) = \frac{6\sqrt{29-2\sqrt{2}}-3.72x^2}{6\sqrt{29-2\sqrt{2}}-3.72x^2+2\sqrt{3}x^2}$$

$$f_{111}(x) = \frac{2\sqrt{3}x^2}{6\sqrt{29-2\sqrt{2}}-3.72x^2+2\sqrt{3}x^2}$$

$$(O)\,to\,(DI-O)$$

$$0 < x < x_{max}$$

$$x_{max} = \frac{1}{2}$$

$$\begin{aligned} V(x) &= V_{Oct} - 3V'_{Oct} + 6V_{SquarePyramid} \\ &= \frac{1}{3}\sqrt{2}a^3 - \sqrt{2}(ax)^3 + \frac{1}{3}\sqrt{2}(ax)^3 \\ &= \sqrt{2}a^3\left[\frac{1}{3} + x^3\left(\frac{1}{3} - 1\right)\right] \\ &= \frac{\sqrt{2}}{3}a^3\left(1 - 2x^3\right) \end{aligned}$$

$$\begin{aligned} S(x) &= S_{Oct} - 3S'_{Oct} + 6S_{SquarePyramid} \\ &= 2\sqrt{3}a^2 - 6\sqrt{3}(ax)^2 + 2\sqrt{11}(ax)^2 \\ &= 2\sqrt{3}a^2\left(1 - 3x^2\right) + 2\sqrt{11}(ax)^2 \end{aligned}$$

$$a(x) = \left[\frac{3V}{\sqrt{2}(1-2x^3)}\right]^{\frac{1}{3}}$$

$$q(x) = \frac{1}{a}\left[\frac{2\sqrt{3}\left(1-3x^2\right) + 2\sqrt{11}x^2}{\frac{\sqrt{2}}{3}(1-2x^3)}\right]$$

$$f_{111}(x) = \frac{2\sqrt{3}\left(1-3x^2\right)}{2\sqrt{3}(1-x^2) + 2\sqrt{11}x^2}$$

$$f_{311}(x) = \frac{2\sqrt{11}x^2}{2\sqrt{3}(1-x^2) + 2\sqrt{11}x^2}$$

Appendix B. Definitions of q and f_i for wurtzite phase morphologies

The surface-to-volume ratio q and facet weighting factors f_i are defined for nanoparticles and nanorods (possessing uniformly oriented capping facets and zero or non-zero aspect ratios) in the wurtzite phase in terms of the average nanoparticle diameter <*D*> and three shape paramters *x*, *x'*, and *x''*. These shape parameters represent the aspect ratio, truncation of the $\{10\bar{1}0\}$ planes in the $<11\bar{2}0>$ direction and truncation of the pyramidal capping facets in the <0002> direction, respectively, and are shown schematically in Figure B.1.

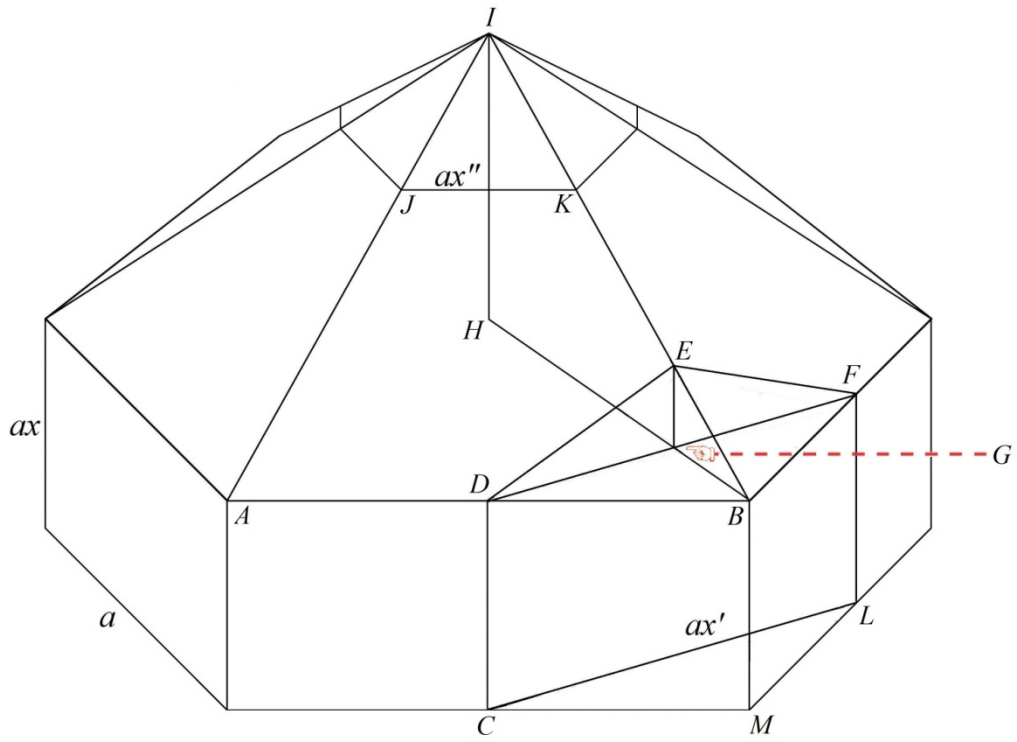

Figure B.1 – A schematic representation of the wurtzite shape with all critical points necessary to define all surface-to-volume ratios and facet weighting factors contained in the morphology space defined by <*D*>, *x*, *x'* and *x''*.

The surface to volume ratio q_{WZ} (for shapes in the wurtzite phase) is defined as follows:

$$q_{WZ}\left(\langle D\rangle, x, x', x''\right) = \frac{S_{WZ}\left(\langle D\rangle, x, x, x\right)}{V_{WZ}\left(\langle D\rangle, x, x, x\right)} \qquad \text{Eq B.1}$$

where $S_{WZ}(\langle D\rangle, x, x', x'')$ and $V_{WZ}(\langle D\rangle, x, x', x'')$ are the surface area and volume of any given WZ shape in the morphology space spanned by $\langle D\rangle$, x, x' and x''.

From Eq B.1 and with respect to Figure B.1, the surface area term is defined as follows:

$$\begin{aligned} S_{WZ}\left(\langle D\rangle, x, x', x''\right) &= 6\overline{AB}\,\overline{CD} + 12\triangle_{ABI} - 12\overline{CD}\,\overline{DB} - 24\triangle_{BDE} \\ &\quad + 6\overline{CD}\,\overline{DF} + 12\triangle_{DEF} - 12\triangle_{JKL} + 2S_{BasalPlane} \\ &= 6a^2x + 2S_{HexPyr} - 12ax\overline{BD} - 24\triangle_{BDE} \\ &\quad + 6a^2xx' + 12\triangle_{DEF} - 2S''_{HexPyr} + 2S_{BasalPlane} \end{aligned} \qquad \text{Eq B.2}$$

where S_{HexPyr} and S''_{HexPyr} refer to the surface areas of hexagonal pyramids of base edge lengths a and ax'', respectively and $S_{BasalPlane}$ refers to the surface area of basal planes of edge lengths ax''.

From Eq B.2:

$$\begin{aligned} S_{HexPyr} &= \frac{3}{2}a\sqrt{3a^2 + 4\overline{HI}^2} \\ &= \frac{3}{2}a\sqrt{3a^2 + 4\left(\frac{az}{l}\right)^2} \\ &= \frac{3}{2}a^2\sqrt{3 + 4\left(\frac{z}{l}\right)^2} \\ &= \frac{3}{2}a^2\sqrt{3 + 4\alpha^2} \end{aligned} \qquad \text{Eq B.3}$$

where $\alpha = \frac{z}{l}$; l is the value of the index in standard $\{hjkl\}$ notation for the appropriate pyramidal capping facet; and z is the ratio of the wurtzite lattice constants $\frac{c_0}{a_0} = \frac{6.30}{3.85} = 1.64$.

Further terms in Eq B.2 are defined as follows:

$$\overline{BD} = \frac{\sin\theta_{BDG}}{\sin\theta_{DBF}} ax' = \frac{\sin 30^o}{\sin 120^o} ax' = \frac{1}{\sqrt{3}} ax' \qquad \text{Eq B.4}$$

and

$$\triangle_{BDE} = \sqrt{s\left(s-\overline{BD}\right)\left(s-\overline{DE}\right)\left(s-\overline{EB}\right)} \qquad \text{Eq B.5}$$

where:

$$s = \frac{\overline{BD}+\overline{DE}+\overline{EB}}{2} \qquad \text{Eq B.6}$$

.

From Eq B.6:

$$\overline{EB} = \left(\overline{EG}^2 + \overline{BG}^2\right)^{\frac{1}{2}} = \frac{1}{2\sqrt{3}}\left(1+\alpha^2\right) ax' \; ; \qquad \text{Eq B.7}$$

$$\overline{BD} = \frac{1}{\sqrt{3}} ax' \qquad \text{Eq B.8}$$

and

$$\overline{DE} = \left(\overline{DG}^2 + \overline{EG}^2\right)^{\frac{1}{2}} \qquad \text{Eq B.9}$$

.

From Eq B.9:

$$\overline{DG} = \frac{ax'}{2} \qquad \text{Eq B.10}$$

and

$$\overline{EG} = \overline{BG}\,\tan\theta_{EBG} \qquad \text{Eq B.11}$$

where:

$$\overline{BG} = \left(\overline{BD}^2 - \overline{DG}^2\right)^{\frac{1}{2}} = \left[\left(\frac{1}{\sqrt{3}} ax'\right)^2 - \left(\frac{ax'}{2}\right)^2\right]^{\frac{1}{2}} = \frac{1}{2\sqrt{3}} ax' \qquad \text{Eq B.12}$$

and

$$\theta_{EBG} = \arctan\frac{\overline{HI}}{\overline{BH}} = \arctan\alpha \qquad \text{Eq B.13}$$

.

The remaining terms in Eq B.2 are defined as follows:

$$\triangle_{DEF} = \frac{1}{2} a x' \overline{EG} = \frac{\alpha}{4\sqrt{3}} \left(a x'\right)^2 \quad ; \qquad \text{Eq B.14}$$

$$S''_{HexPyr} = \frac{3}{2} \left(a x''\right)^2 \sqrt{3 + 4\alpha^2} \qquad \text{Eq B.15}$$

and

$$S_{BasalPlane} = \frac{3}{2} \sqrt{3} a^2 x''^2 \quad . \qquad \text{Eq B.16}$$

Substituting Eqs B.3, B.4, B.14, B.15 and B.16 into Eq B.2 gives:

$$\begin{aligned} S_{WZ}\left(\langle D \rangle, x, x', x''\right) = {} & 6a^2 x + 3a^2 \sqrt{3 + 4\alpha^2} - 4\sqrt{3} a^2 x x' - 24 \triangle_{BDE} \\ & + 6a^2 x x' + \sqrt{3} a^2 x'^2 \alpha - 3 \left(a x''\right)^2 \sqrt{3 + 4\alpha^2} + 3\sqrt{3} \left(a x''\right)^2 \end{aligned} \qquad \text{Eq B.17}$$

where Δ_{BDE} is defined by Eqs B.5 to B.13.

The volume term in Eq B.1 is defined as follows:

$$\begin{aligned} V_{WZ}\left(\langle D \rangle, x, x', x''\right) &= V_{HexPrism} + 2V_{HexPyr} - 12V_1 - 6V_2 - 2V''_{HexPyr} \\ &= \frac{3}{2}\sqrt{3} a^3 x + \sqrt{3} a^3 \alpha - 12V_1 - 6V_2 - \sqrt{3} \left(a x''\right)^3 \alpha \end{aligned} \qquad \text{Eq B.18}$$

where $V_{HexPrism}$ refers to the volume of a hexagonal prism of edge lengths *a* and *ax*; V_{HexPyr} and V'_{HexPyr} refer to the volumes of hexagonal pyramids of base edge lengths *a* and *ax''*, respectively; V_1 refers to the volume enclosed by points *B*, *D*, *E* and *F*; and V_2 refers to the volume enclosed by points *C*, *D*, *F*, *L*, *B* and *M*. The two remaining terms in Eq. B.18 are defined as follows:

$$\begin{aligned} V_1 &= \int_0^r A_{\triangle_{BDF}}\left(x'\right) dy \\ &= \int_0^r \frac{1}{2} b_{\triangle_{BDF}}\left(x'\right) h_{\triangle_{BDF}}\left(x'\right) dy \end{aligned} \qquad \text{Eq B.19}$$

where *r* is the length of line $\overline{GE}$ and $A_{\Delta BDF}$ is the area of the triangle which is defined by points *B*, *D* and *F* at *y*=0, which are both functions of *x'*, and where *y* is in the direction of *l* in

the hexagonal {*hjkl*} axis (the <0001> direction). In Eq B.19, $b\Delta_{BDF}$ and $h\Delta_{BDF}$ are the base length and height respectively, of the triangle which is *BDF* at *y*=0, corresponding respectively to lines $\overline{DF}$ and $\overline{GB}$ at *y*=0 and 0 for both at *y*=*r*.

From Eq. B.19:

$$b_{\triangle_{BDF}}(x') = ax' - 2\delta ax' \qquad \text{Eq B.20}$$

where:

$$\delta ax' = \frac{y}{\tan\theta_{EDF}} \qquad \text{Eq B.21}$$

and

$$\theta_{EDF} = \arctan\frac{2\overline{EG}}{ax'} = \arctan\frac{\alpha}{\sqrt{3}} \qquad \text{Eq B.22}$$

The remaining term in Eq B.19 is defined as follows:

$$h_{\triangle_{BDF}}(x') = \overline{BG} - \delta\overline{BG} \qquad \text{Eq B.23}$$

where:

$$\delta\overline{BG} = \frac{y}{\tan\theta_{EBG}} \qquad \text{Eq B.24}$$

and

$$\theta_{EBG} = \arctan\frac{\overline{EG}}{\overline{BG}} = \arctan\alpha \qquad \text{Eq B.25}$$

Combining Eqs B.20 to B.22 and Eqs B.23 to B.25 and substituting back into Eq B.19 gives:

$$V_1 = \frac{1}{2}\int_0^r \left(ax' - \frac{2\sqrt{3}}{\alpha}y\right)\left(\frac{ax'}{2\sqrt{3}} - \frac{1}{\alpha}y\right)dy$$

$$= \frac{1}{2}\int_0^r \frac{(ax')^2}{2\sqrt{3}} - 2\frac{ax'}{\alpha}y + \frac{2\sqrt{3}}{\alpha^2}y^2 dy$$

$$= \frac{1}{2}\left[\frac{(ax')^2}{2\sqrt{3}}y - \frac{ax'}{\alpha}y^2 + \frac{2}{\sqrt{3}\alpha^2}y^3\right]_0^r$$

$$= \frac{1}{2}\left[\frac{(ax')^2}{2\sqrt{3}}r - \frac{ax'}{\alpha}r^2 + \frac{2}{\sqrt{3}\alpha^2}r^3\right]$$

$$= \frac{1}{2}\left[\frac{(ax')^2}{2\sqrt{3}}\frac{\alpha}{2\sqrt{3}ax'} - \frac{ax'}{\alpha}\left(\frac{\alpha}{2\sqrt{3}ax'}\right)^2 + \frac{2}{\sqrt{3}\alpha^2}\left(\frac{\alpha}{2\sqrt{3}ax'}\right)^3\right]$$

$$= \frac{(ax')^3}{2}\left[\frac{\alpha}{12} - \frac{\alpha}{12} + \frac{\alpha}{36}\right]$$

$$= \frac{\alpha}{72}(ax')^3 \qquad \text{Eq B.26}$$

The remaining term in Eq B.18 is defined as follows:

$$V_2 = \frac{1}{2}b_{\triangle BDF}(x')\,h_{\triangle BDF}(x')\,ax$$

$$= \frac{1}{2}ax'\overline{BG}ax = \frac{1}{2}a^2xx'\frac{1}{2\sqrt{3}}ax'$$

$$= \frac{1}{4\sqrt{3}}a^3xx'^2 \qquad \text{Eq B.27}$$

Substituting Eqs B.26 and B.27 into Eq B.18 gives:

$$V_{WZ}(\langle D\rangle, x, x', x'') = \frac{3}{2}\sqrt{3}a^3x + \sqrt{3}a^3\alpha - \frac{\alpha}{6}(ax')^3 - \frac{\sqrt{3}}{2}a^3xx'^2 - \sqrt{3}(ax'')^3\alpha \quad \text{Eq B.28}$$

By obtaining a as a function of <*D*> from Eq B.28 (using a spherical approximation to obtain <D> from *V*) and substituting Eqs B.17 and B.28 into Eq B.1 we get q for all wurtzite shapes as a function of size and the three shape parametres *x*, *x'* and *x''*.

The facet specific weighting factors, based on the terms in Eq B.17, are as follows:

$$f_{10\bar{1}0} = \frac{6x - 4\sqrt{3}xx'}{6x + 3\sqrt{3+4\alpha^2} - 4\sqrt{3}xx' - \frac{24\triangle_{BDE}}{a^2} + 6xx' + \sqrt{3}x'^2\alpha - 3\left(x''\right)^2\sqrt{3+4\alpha^2} + 3\sqrt{3}\left(x''\right)^2}$$

Eq B.29

$$f_{11\bar{2}0} = \frac{6xx' + \sqrt{3}x'^2\alpha}{6x + 3\sqrt{3+4\alpha^2} - 4\sqrt{3}xx' - \frac{24\triangle_{BDE}}{a^2} + 6xx' + \sqrt{3}x'^2\alpha - 3\left(x''\right)^2\sqrt{3+4\alpha^2} + 3\sqrt{3}\left(x''\right)^2}$$

Eq B.30

$$f_{10\bar{1}l} = \frac{3\sqrt{3+4\alpha^2} - \frac{24\triangle_{BDE}}{a^2} - 3\left(x''\right)^2\sqrt{3+4\alpha^2}}{6x + 3\sqrt{3+4\alpha^2} - 4\sqrt{3}xx' - \frac{24\triangle_{BDE}}{a^2} + 6xx' + \sqrt{3}x'^2\alpha - 3\left(x''\right)^2\sqrt{3+4\alpha^2} + 3\sqrt{3}\left(x''\right)^2}$$

Eq B.31

$$f_{0002} = \frac{3\sqrt{3}\left(x''\right)^2}{6x + 3\sqrt{3+4\alpha^2} - 4\sqrt{3}xx' - \frac{24\triangle_{BDE}}{a^2} + 6xx' + \sqrt{3}x'^2\alpha - 3\left(x''\right)^2\sqrt{3+4\alpha^2} + 3\sqrt{3}\left(x''\right)^2}$$

Eq B.32

Chapter 7 reports on the modelling of a WZ shape (labelled l=2|3) consisting of varying proportions of {10$\bar{1}$2}, {10$\bar{1}$3} and {0002} surfaces. This is achieved using an aditional variable to those defined above. This variable x''' represents truncation of {10$\bar{1}$2} surfaces in the <10$\bar{1}$3> directions. As stated in Chapter 7, this variable spans the range $0 \leq x''' \leq 1$, where 0 is no truncation and 1 is complete (effectively Figure 7.4(a) and (b), respectively). Truncation in the <0002> direction is limited to the {10$\bar{1}$3} surfaces, as any truncation of the {10$\bar{1}$2} surfaces in this direction forms a shape which is described by l=2. For this specific shape, the surface-to-volume ratio $q_{2|3}$ is defined as:

$$q_{2|3}\left(\langle D\rangle, x'', x'''\right) = \frac{S_{2|3}\left(\langle D\rangle, x'', x'''\right)}{V_{2|3}\left(\langle D\rangle, x'', x'''\right)} \qquad \text{Eq B.33}$$

where $S_{2|3}(\langle D\rangle, x'', x''')$ and $V_{2|3}(\langle D\rangle, x'', x''')$ are the surface area and volume of any given WZ shape in the morphology space spanned by $\langle D\rangle$, x'' and x'''.

From Eq B.33 the surface area term is defined as follows:

$$S_{2|3}\left(\langle D\rangle, x'', x'''\right) = 2S_{l=2,HexPyr} - 2S'''_{l=2,HexPyr} + 2S'''_{l=3,HexPyr} - 2S''_{l=3,HexPyr} + 2S_{BasalPlane} \quad \text{Eq B.34}$$

where the first four terms are the surface areas of hexagonal pyramids consisting of, respectively, {10$\bar{1}$2} facets with base edge length *a*, {10$\bar{1}$2} facets with base edge length *ax'''*, {10$\bar{1}$3} facets with base edge length *ax'''*, and {10$\bar{1}$3} facets with base edge length *ax''x'''*, and $S_{BasalPlane}$ refers to the surface area of basal planes of edge lengths *ax''x'''*.

In general, the surface area of a hexagonal pyramid of height $a\frac{z}{l}$ and base edge length *a* is:

$$S_{HexPyr} = \frac{3}{2}a^2\sqrt{3+4\alpha^2} \quad \text{Eq B.35}$$

Applying Eq B.35 to Eq B.34 gives the following:

$$\begin{aligned} S_{2|3}\left(\langle D\rangle, x'', x'''\right) &= 3a^2\sqrt{3+4\alpha_2^2} - 3\left(ax'''\right)^2\sqrt{3+4\alpha_2^2} + 3\left(ax'''\right)^2\sqrt{3+4\alpha_3^2} \\ &\quad - 3\left(ax''x'''\right)^2\sqrt{3+4\alpha_3^2} + 3\sqrt{3}\left(ax''x'''\right)^2 \\ &= 3a^2\sqrt{3+4\alpha_2^2}\left(1-x'''^2\right) + 3\left(ax'''\right)^2\sqrt{3+4\alpha_3^2}\left(1-x''^2\right) \\ &\quad + 3\sqrt{3}\left(ax''x'''\right)^2 \end{aligned} \quad \text{Eq B.36}$$

where the subscript *l* on the α terms indicates the appropriate value of *l* contained in α.

The volume term in Eq B.33 is as follows:

$$V_{2|3}\left(\langle D\rangle, x'', x'''\right) = 2V_{l=2,HexPyr} - 2V'''_{l=2,HexPyr} + 2V'''_{l=3,HexPyr} - 2V''_{l=3,HexPyr} \quad \text{Eq B.37}$$

where each terms refers to the volume of hexagonal pyramids consisting of, respectively, {10$\bar{1}$2} facets with base edge length *a*, {10$\bar{1}$2} facets with base edge length *ax'''*, {10$\bar{1}$3} facets with base edge length *ax'''*, and {10$\bar{1}$3} facets with base edge length *ax''x'''*.

In general, the volume of a hexagonal pyramid of height $a\frac{z}{l}$ and base edge edge length a is:

$$V_{HexPyr} = \frac{\sqrt{3}}{2}a^2\alpha \qquad \text{Eq B.38}$$

Applying Eq B.35 to Eq B.34 gives the following:

$$V_{2|3}\left(\langle D\rangle, x'', x'''\right) = \sqrt{3}a^3\alpha_2 - \sqrt{3}\left(ax'''\right)^3\alpha_2 + \sqrt{3}\left(ax'''\right)^3\alpha_3 - \sqrt{3}\left(ax''x'''\right)^3\alpha_3 \qquad \text{Eq B.39}$$

where the subscript l on the α terms indicates the appropriate value of l contained in α.

By obtaining a as a function of <*D*> from Eq B.39 (using a spherical approximation to obtain <D> from *V*) and substituting Eqs B.36 and B.39 into Eq B.33 we get q for all wurtzite shapes as a function of size and the two shape parametres *x''* and *x'''*.

The facet specific weighting factors, based on the terms in Eq B.36, are as follows:

$$f_{10\bar{1}2} = \frac{3\sqrt{3+4\alpha_2^2}\left(1-x'''^2\right)}{3\sqrt{3+4\alpha_2^2}\left(1-x'''^2\right)+3x'''^2\sqrt{3+4\alpha_3^2}\left(1-x''^2\right)+3\sqrt{3}\left(x''x'''\right)^2} \qquad \text{Eq B.40}$$

$$f_{10\bar{1}3} = \frac{3x'''^2\sqrt{3+4\alpha_3^2}\left(1-x''^2\right)}{3\sqrt{3+4\alpha_2^2}\left(1-x'''^2\right)+3x'''^2\sqrt{3+4\alpha_3^2}\left(1-x''^2\right)+3\sqrt{3}\left(x''x'''\right)^2} \qquad \text{Eq B.41}$$

$$f_{0002} = \frac{3\sqrt{3}\left(x''x'''\right)^2}{3\sqrt{3+4\alpha_2^2}\left(1-x'''^2\right)+3x'''^2\sqrt{3+4\alpha_3^2}\left(1-x''^2\right)+3\sqrt{3}\left(x''x'''\right)^2} \qquad \text{Eq B.42}$$